

AD-A053 772

TORONTO UNIV (ONTARIO) INST FOR AEROSPACE STUDIES  
EFFECTS OF IMPURITIES ON SHOCK WAVE STABILITY AND STRUCTURE IN --ETC(U)

F/G 20/4

NOV 77 F C TANG

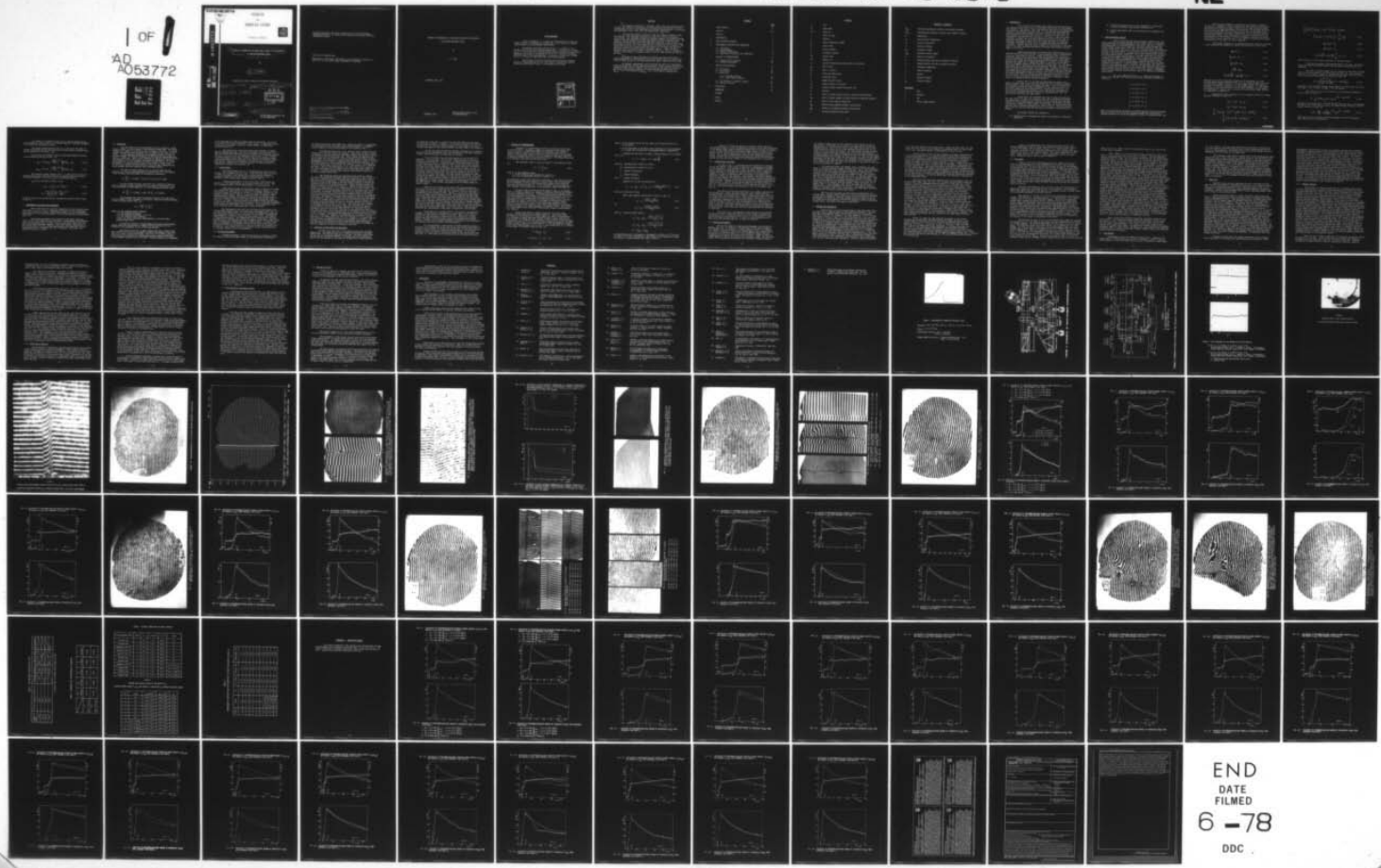
AFOSR-77-3303

UNCLASSIFIED

UTIAS-TN-212

AFOSR-TR-78-0841

NL



AFOSR-TR-78-0841



INSTITUTE  
FOR  
AEROSPACE STUDIES



UNIVERSITY OF TORONTO

AD A 053772

AD No. 1  
DDC FILE COPY

6 EFFECTS OF IMPURITIES ON SHOCK WAVE STABILITY AND STRUCTURE  
IN IONIZING MONATOMIC GASES.

by

10 F. C. Tang

Approved for public release; distribution unlimited.

15 AFOSR-77-3343

18 AFOSR

19 TR-78-0841

16 2307

17 A3

DDC  
RECEIVED  
MAY 8 1978

12 94P.

9 Technical note

HPB

14 UTIAS-TN-212

UTIAS Technical Note No. 212  
CN ISSN 0082-5263

11 November 1977

178 920

JOB

Qualified requestors may obtain additional copies from the Defense Documentation Center, all others should apply to the National Technical Information Service.

Conditions of Reproduction:

Reproduction, translation, publication, use and disposal in whole or in part by or for the United States Government is permitted.

**AIR FORCE OFFICE OF SCIENTIFIC RESEARCH (AFSC)**  
**NOTICE OF TRANSMITTAL TO DDC**  
This technical report has been reviewed and is  
approved for public release IAW AFR 190-12 (7b).  
Distribution is unlimited.  
A. D. BLOSE  
Technical Information Officer

EFFECTS OF IMPURITIES ON SHOCK WAVE STABILITY AND STRUCTURE  
IN IONIZING MONATOMIC GASES

by

F. C. Tang

Submitted July, 1977

November, 1977

UTIAS Technical Note No. 212  
CN ISSN 0082-5263

Acknowledgement

I wish to thank Dr. I. I. Glass for the opportunity to work and study at UTIAS. His guidance and supervision in the course of my Master-degree program is very gratefully acknowledged.

The helpful assistance afforded by Mr. B. T. Whitten in all aspects of this project is sincerely appreciated. I should like to thank Dr. W. S. Liu for providing the theoretical results presented in this report. Thanks are due to Mr. B. T. Whitten and Dr. M. P. F. Bristow for making available some of the interferograms. In addition I should like to thank Mr. R. L. M. Wong for digitizing some of the interferograms.

The financial assistance received from the National Research Council of Canada and the U.S. Air Force Office of Scientific Research under grant USAF-AFOSR 77-3303, is acknowledged with thanks.

ACCESSION for	
NTIS	White Section <input checked="" type="checkbox"/>
DDC	Buff Section <input type="checkbox"/>
UNANNOUNCED <input type="checkbox"/>	
JUSTIFICATION _____	
BY _____	
DISTRIBUTION/AVAILABILITY CODES	
Dist. AVAIL and/or SPECIAL	
A	

### Abstract

The effects of impurities - hydrogen, water vapour and sodium chloride - on shock wave stability and structure in ionizing-argon and krypton flows were investigated by using a dual-wavelength Mach-Zehnder interferometer in conjunction with the UTIAS 10 cm x 18 cm (4" x 7") Hypervelocity Shock Tube.

At shock Mach number of about 15, when pure argon or krypton is used as a test gas, the resulting translational shock front develops sinusoidal oscillations. The subsequent ionization relaxation region, the electron-cascade front and the quasi-equilibrium state also exhibit unstable characteristics. The addition of small amounts of hydrogen (0.5% by pressure) to the test gas stabilizes the entire flow and at the same time drastically shortens the relaxation length to about 1/3 of the original value in argon and 2/3 in krypton. The addition of about 1% of water vapour (by pressure) to the argon test gas also stabilizes the flow and shortens the relaxation region. A thin coating of dissolved sodium chloride in water on the shock tube wall, which on evacuation leaves a rough surface of crystals, however, does not seem to have any effect on the flow.

Although the small impurities of hydrogen and water vapour have a significant effect in stabilizing the shock, the overall values of density and electron number density in the quasi-equilibrium region remain nearly the same.

The present experimental results provided the data for a theoretical study which took into account atom-atom collisions, electron-atom collisions and radiation-energy losses to deduce a precise value for the atom-atom collision excitation cross-section constants for argon and krypton having values of  $S_{Ar-Ar}^* = 1.0 \times 10^{-19} \text{ cm}^2/\text{eV}$  and  $S_{Kr-Kr}^* = 1.2 \times 10^{-19} \text{ cm}^2/\text{eV}$ , respectively.

CONTENTS

	<u>Page</u>
Acknowledgement	ii
Abstract	iii
Notation	v
1. INTRODUCTION	1
2. SHOCK STRUCTURE ANALYSIS	2
3. EXPERIMENTAL FACILITIES AND TECHNIQUES	5
3.1 Shock Tube	6
3.2 Interferometer	7
3.3 Velocity Measurement	7
3.4 Admission of Test Gases and Impurities	8
4. ANALYSIS OF INTERFEROGRAMS	10
4.1 Gladstone-Dale Constants	12
4.2 Digitizing Equipment	12
5. RESULTS AND DISCUSSIONS	13
5.1 Pure Argon	15
5.2 Pure Krypton	16
5.3 Impurities	17
5.3.1 Hydrogen Impurity	18
5.3.2 Water Vapour Impurity	19
5.4 Wall Effects in Relaxation Region	21
5.5 Sources of Errors	22
6. CONCLUSIONS	23
REFERENCES	24
FIGURES	
TABLES	
APPENDIX	

### Notation

a	Atom
Ar	Argon atom
$\text{Ar}^+$	Argon ion
c	Speed of light
e	Electron
g	Atomic statistical weight
$\bar{g}$	Gaunt factor
h	Planck constant
k	Boltzmann constant
Kr	Krypton atom
$\text{Kr}^+$	Krypton ion
L	Distance travelled by light source in shock tube
$m_a$	Mass of atom
$m_e$	Mass of electron
$M_s$	Shock wave Mach number
n	Refractive index
$n_a$	Number density of atoms
$n_e$	Number density of electrons
$\dot{n}_e$	Electron number density production rate
p	Pressure
$Q_B$	Rate of radiant energy loss/unit volume by line radiation
$Q_C$	Rate of radiant energy loss/unit volume by continuum radiation
$Q_R$	Rate of total radiant energy loss
$Q_{ea}$	Electron atom momentum transfer cross-section
$Q_{ei}$	Electron ion momentum transfer cross-section
S	Nondimensionalized fringe shift

Notation - Continued

$S_{a-a}^*$	Atom-atom excitation collision cross section constant
$S_{e-a}^*$	Electron-atom inelastic collision cross section constant
T	Temperature
$T_a$	Heavy particle temperature
$T_e$	Electron temperature
u	Particle velocity
$X_E$	Relaxation length
$Z_{\text{eff}}$	Effective nuclear charge
$\alpha$	Degree of ionization
$\phi$	Energy transfer rate due to inelastic collision
$\eta$	Energy transfer rate due to elastic collision
$\theta$	Ionization temperature
$\nu_c$	Cut-off frequency
$\rho$	Density
$\omega$	Angular frequency
$\omega_p$	Plasma frequency

Subscripts

a	Atom
e	Electron
i	Ion
s	Shock, plasma species

## 1. INTRODUCTION

The ionization of monatomic gases behind strong shock waves is now understood quite well owing to considerable theoretical and experimental work devoted to the subject. After some detailed theoretical and experimental considerations, Petschek and Byron (Ref. 1) concluded that the mechanisms leading to equilibrium ionization were first controlled by impurities and then dominated by electron-atom collisions. Harwell and Jahn's (Ref. 2) experimental work supported the proposal of Bond (Ref. 3) that the initial ionization proceeded via a two-step atom-atom collision process; that is, electronic excitation to the first excited state followed by ionization. Subsequent investigators (Refs. 4-8) all adopted the model for achieving ionization relaxation as first due to atom-atom and then electron-atom collisions. However, there are quite a number of discrepancies in the value used for the argon atom-atom excitational collision cross-section constant (Refs. 2, 4, 9, 10).

Harwell and Jahn (Ref. 2) observed that unknown impurities in the test gases had profound effects on the ionization rates at concentration as low as a few parts per million. Morgan and Morrison (Ref. 4) using a relatively simple theory and based on some characteristic excitation energy tried to fit Harwell and Jahn's (Ref. 2) experimental result. They hypothesised that sodium and nitrogen impurities had a definite effect whereas hydrogen and oxygen had no significant effect on the rate of ionization. These are somewhat contrary to the findings of Bristow (Ref. 11), who showed that oxygen had no observable effect but hydrogen did have a significant effect in reducing the ionization relaxation time. Schneider and Park (Ref. 12) studied the ionization rates using NaCl-contaminated argon as a test gas. Their measurements showed that an increase in the rate of ionization was due to electron detachment of negative chlorine ions produced from the sodium chloride vapour. They also concluded that atmospheric impurities such as  $H_2O$ ,  $N_2$  and  $CO_2$  had insignificant effect on the rate of ionization. This result is contradicted by the present experiments.

Enomoto (Ref. 8) included the perturbations caused by the laminar boundary layer in his work and showed that the ionization relaxation time shortened as the shock tube diameter decreased. (He also showed that the ionization relaxation time was dependent on the initial pressure for a given Mach number and shock tube diameter.) McLaren and Hobson (Ref. 10) also included boundary layer effects in their theoretical considerations. It should be noted that the above authors all adopted Mirels' (Ref. 13) theory which considered only ideal gases.

D'yakov (Ref. 14) initiated the study of shock wave stability and later Swan et al (Ref. 15) and Fowles (Ref. 16) re-examined the subject and came up with a condition for stability for real gases at very high Mach number when the Hugoniot changes slope and curvature. Griffiths et al (Ref. 17) have also looked into this problem. Levine (Ref. 18) studied shock wave stability due to turbulent mixing at the contact surface. The above investigators were not involved with the same type of instability first observed by Bristow.

The present research was designed to:

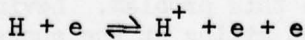
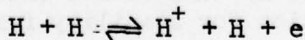
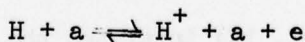
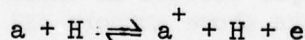
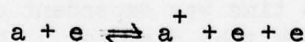
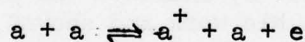
- (1) Experimentally investigate the effects of impurities on shock wave stability,

- (2) Provide experimental data for the determination of atom-atom collision excitation cross-section constants, and
- (3) Provide experimental data for the choosing of a radiation-loss model.

## 2. SHOCK STRUCTURE ANALYSIS

Before considering the shock structure equations, the collisional ionization processes employed in this analysis will be discussed. Immediately behind the Rankine-Hugoniot shock front, the gas is heated to high temperature by a few translational collisions, which increase the kinetic energy of the atoms. Then via a two step atom-atom collisional process, which takes some atoms to their first excited state, and subsequent collisions ionize the atoms. In this manner the first few electrons are produced. The next phase is dominated by the much more efficient electron-atom collisional process, leading to a very rapid production of electrons. As the electron number density reaches a certain level, the three body (electron-ion-electron) recombination process becomes important and this is followed by a quasi-equilibrium state. Subsequently, the electron number density drops due to radiant energy losses as electrons and atoms recombine and de-excite. In the radiative cooling region, the plasma is almost in an equilibrium state. It can be concluded that the entire shock-wave structure can be divided into two regions, the ionization relaxation region and the radiative cooling region. The former region is dominated by collisional processes while the latter region is dominated by radiation energy losses.

For a two-component mixture, i.e., argon with hydrogen or krypton with hydrogen, the following collisional ionization processes are considered:



Here, we assume that the ionization of hydrogen molecules starts effectively behind the strong shock since the relaxation length for dissociation of hydrogen molecules is very short compared with that of ionization (Ref. 19).

The following assumptions are made in the theoretical analysis:  
 (1) the flow is steady and quasi-one-dimensional when viewed in shock-fixed coordinates; (2) the gas is singly ionized; (3) the heavy particles (atoms and ions) have the same temperatures and velocities; (4) the heavy particles and electrons have Maxwellian velocity distributions corresponding to the local atom temperature and electron temperature; (5) the electron diffusive velocity with respect to the heavy particle velocity is very small and can be neglected; (6) the effects of electric and magnetic fields on the shock-wave structure can be neglected; and (7) the effects of viscosity and thermal conductivity are very small and can be neglected.

Under these assumptions, the governing equations which are applicable to the nonequilibrium relaxing flow behind the shock wave are (Ref. 20):

$$\frac{d}{dx} (\rho u) = 0 \quad (2.1)$$

$$\frac{d}{dx} (\rho u^2 + P) = 0 \quad (2.2)$$

$$\frac{d}{dx} (\rho u H) = -Q_R \quad (2.3)$$

$$\rho u \frac{d\alpha}{dx} = m_a \dot{n}_e \quad (2.4)$$

$$\frac{3}{2} n_e u k \frac{dT_e}{dx} + n_e k T_e \frac{du}{dx} = \eta + \phi \quad (2.5)$$

where  $Q_R$  is the rate of radiation energy loss of the plasma,  $\dot{n}_e$  is the electron number density production rate,  $\eta$  is the energy transfer rate given to electrons by elastic collision,  $\phi$  is the energy transfer rate given to electrons by inelastic collisions,  $\rho$  is the plasma density,  $u$  is the plasma velocity,  $P$  is the flow pressure,  $H$  is the total enthalpy,  $\alpha$  is the degree of ionization [ $\alpha = n_e/(n_e + n_a)$ ],  $n_e$  and  $T_e$  are the electron number density and temperature, respectively.

Expanding the above equations for a two-component mixture of plasma, they may be written as (Ref. 21)

$$(n_{a1} + n_{e1})u = n_{01} u_{01} \quad (2.6)$$

$$(n_{a2} + n_{e2})u = n_{02} u_{02} \quad (2.7)$$

$$\begin{aligned} & \sum_{j=1}^2 \left\{ m_{aj} (n_{aj} + n_{ej}) u^2 + n_{ej} k T_e + (n_{aj} + n_{ej}) k T_a \right\} \\ &= \sum_{j=1}^2 \left\{ m_{aj} n_{0j} u_{0j}^2 + n_{0j} k T_{0j} \right\} \end{aligned} \quad (2.8)$$

$$\sum_{j=1}^2 \left\{ \frac{d}{dx} \left[ \frac{1}{2} m_{aj} (n_{aj} + n_{ej}) u^3 + \frac{5}{2} (n_{aj} + n_{ej}) kT_a u + \frac{5}{2} n_{ej} kT_e u + n_{ej} k\theta_j u \right] \right\} = - \sum_{j=1}^2 (Q_{Rj}) \quad (2.9)$$

$$\frac{d}{dx} (n_{el} u) = \dot{n}_{el} \quad (2.10)$$

$$\frac{d}{dx} (n_{e2} u) = \dot{n}_{e2} \quad (2.11)$$

$$\frac{3}{2} n_e u k \frac{dT_e}{dx} + n_e kT_e \frac{du}{dx} = \sum_{j=1}^2 (n_j + \phi_j) \quad (2.12)$$

where subscripts 1 and 2 denote components of the gas mixture.

Since the percentage of the hydrogen impurity is small, the kinetic energy and momentum transfers between the two types of heavy particles are neglected.

The rate of radiant energy loss,  $Q_R$ , consists of the rates of energy loss by continuum radiation,  $Q_C$ , and by line radiation,  $Q_B$ . The continuum radiation in a plasma is caused by recombination processes (free-bound radiation) and free-free transitions and is given by (Ref. 22)

$$Q_C = \frac{64\pi^{3/2} e^6 n_e^2}{3\sqrt{6} m_e^{3/2} c^3 h \sqrt{kT_e}} (h\nu_c + kT_e) \bar{g} Z_{eff}^2 \quad (2.13)$$

where  $Z_{eff}$  is the effective nuclear charge. Meiners and Weiss (Ref. 23) found that  $Z_{eff}^2 = 1.67$  for argon, and  $Z_{eff}^2 = 1.65$  for krypton.

The energy loss by line radiation due to bound-bound transitions can be written as (Ref. 24)

$$Q_B = \sum_k n_a(k) A_{k,k-1} (E_k - E_{k-1}) e^{-(E_k - E_{k-1})/kT_e} \quad (2.14)$$

where  $E_k$  is the energy level of the  $k^{th}$  excited state and  $A_{k,k-1}$  the radiative transition rate coefficients and  $n_a(k)$  the number density of atoms at the  $k^{th}$  excited state and is given by

$$n_a(k) = \frac{g_k}{2g_I} \left( \frac{h^2}{2\pi m_e kT_e} \right)^{3/2} n_e^2 e^{(k\theta - E_k)/kT_e} \quad (2.15)$$

where  $g_k$  and  $g_I$  are the atomic statistical weights of the  $k^{th}$  excitation level and of the ion, respectively.

For krypton, we assumed that the rate of radiant energy loss by line radiation is equal to that for continuum radiation. The same assumption is also made for the hydrogen plasma.

The elastic energy transfer rate,  $\eta$ , is the sum of the rates of thermal energy given to the free electrons by electron-atom collisions,  $\eta_{ea}$ , and by electron-ion collisions,  $\eta_{ei}$ .

$\eta_{ea}$  and  $\eta_{ei}$  are related to their corresponding momentum transfer cross-sections  $Q_{ea}$  and  $Q_{ei}$  by (Ref. 21)

$$\eta_{ea} = 6 \sqrt{2} n_e n_a \left( \frac{m_e k T_e}{\pi} \right)^{1/2} \frac{Q_{ea}}{m_a} k(T_a - T_e) \quad (2.16)$$

$$\eta_{ei} = 6 \sqrt{2} n_e^2 \left( \frac{m_e k T_e}{\pi} \right)^{1/2} \frac{Q_{ei}}{m_a} k(T_a - T_e) \quad (2.17)$$

The inelastic energy transfer rate,  $\phi$ , is the sum of the rates of thermal energy given to the free electrons by electron-atom and electron-ion-electron inelastic collisions  $\phi_{ea}$  and by bremsstrahlung  $\phi_R$ .

$\phi_{ea}$  and  $\phi_R$  are given by (Refs. 21,22)

$$\phi_{ea} = - (n_e) e \left( k\theta + \frac{3}{2} k T_e \right) \quad (2.18)$$

$$\phi_R = \frac{8\pi n_e^2 e^6 k T_e}{\sqrt{6} m_e^2 c^3 h} \left( \frac{8\pi m_e}{k T_e} \right)^{1/2} \quad (2.19)$$

Further discussions on the theoretical considerations may be found in Refs. 21 and 25.

### 3. EXPERIMENTAL FACILITIES AND TECHNIQUES

Shock tubes have been used very successfully in the study of plasma flows (Refs. 1, 2, 5, 10, 11). Diagnostic techniques are quite different and can be divided into optical interferometry (Refs. 5, 11), electrostatic probes (Refs. 1, 10), microwaves (Refs. 2, 9) and photoelectric interferometry (Ref. 26).

The present experiments were conducted in the UTIAS combustion driven 10 cm x 18 cm Hypervelocity Shock Tube. A Mach-Zehnder interferometer with a 23-cm diameter field of view, using a pulsed laser light source was used as the main diagnostic equipment. Since the original construction of the facility (Refs. 27, 28), several modifications were made which substantially improved the performance and ease of handling. The details are described in Refs. 11 and 29.

### 3.1 Shock Tube

The shock tube can be divided mainly into four sections: driver section, channel or driven section, test section and dump tank. The driver section has a length of 1.42m and an inner diameter of 15.24 cm. A 0.38 mm diameter impulsively heated tungsten wire is located at the centre of the driver. An experimentally determined stoichiometric mixture of 7.5% (by pressure) oxygen, 15% hydrogen diluted by 72.5% helium and 5% hydrogen was used as a driver gas. When a 13 kV potential was applied impulsively across the tungsten wire, the gas mixture was ignited by combustion. The final driver pressure,  $P_4$ , was increased to about 6.6 times that of the initial gas mixture. A typical pressure trace of the driver is shown in Fig. 1. It can be seen clearly how the pressure is built up after combustion and drops suddenly after the stainless steel diaphragm ruptures.

The ratio of driver pressure,  $P_4$ , to initial argon test gas pressure,  $P_1$ , was found experimentally by Bristow (Ref. 11) to be related to the incident shock Mach number by the empirical expression,

$$\ln \left( \frac{P_4}{P_1} \right) = (0.422M_s + 4.02), \text{ for } 10 \leq M_s \leq 24, \text{ argon}$$

For the krypton test gas, there were not a sufficient number of runs to formulate a similar expression over a range of Mach numbers. But it is found that for Mach number  $M_s \sim 15$ , the following expression holds,

$$\ln \left( \frac{P_4}{P_1} \right) = (0.422M_s + 2.92), \text{ for } M_s \sim 15, \text{ krypton}$$

The diaphragms were made of annealed stainless steel type SS304 with an ultimate tensile strength of 85,000 psi. They were scribed according to the following equation (Ref. 11),

$$P_4 = \left( \frac{4\sigma t}{d} \right) K \left( \frac{h}{t} \right)^n$$

where  $\sigma$  is the ultimate tensile strength,  
 $t$  is the diaphragm thickness,  
 $d$  is the unsupported diameter, = 18.1 cm,  
 $h$  is the thickness after scribing,  
 $K$  and  $n$  are values determined experimentally, to ensure proper petaling after burst.

A transition section is located between the driver and the driven section where the cross-section is changed from the circular 15.24 cm diameter to the rectangular 10 cm x 18 cm cross-section.

The driven section has a length of 15.2m with ports located 1.22m apart which can be used to house gauges to monitor the passage of the shock wave or to record its pressure history. The 10 cm x 18 cm test section is 1.22m long and incorporates two interferometer-quality glass windows with a 20 cm diameter aperture and 9.5 cm thick. They are polished to a smoothness

of 1/4 wavelength at 6328 $\text{\AA}$  with wedge angles not exceeding 1 sec of arc. Cross-hairs 8.2 cm apart are mounted on the windows. A dump tank located at the end of the channel serves as a safety feature in preventing a reflected shock wave.

The vacuum-pump system of the shock tube consists of a Kinney type KS-47 mechanical pump, a Heraeus Roots-type VP-RG-350A pump and a CVC type PMCS-6B diffusion pump, which are capable of bringing the pressure down to  $3 \times 10^{-5}$  torr with an outgassing rate of about  $2 \times 10^{-5}$  torr/min. Prolonged pumpdown period does not seem to improve the ultimate vacuum. A mass spectrometric study (Ref. 29) of the present vacuum system showed that the main desorption constituents were water vapour, air and some hydrocarbons. There were no detectable amounts of sodium chloride, as suggested by Schneider and Park (Ref. 13).

### 3.2 Interferometer

The interferometer used is of the Mach-Zehnder type (Ref. 28) and has a 23-cm diameter field of view. A TRG 104A ruby laser, pulsed by a Pockels cell Q-switch and fitted with a second harmonic generator, provided the 6943 $\text{\AA}$  and 3471.5 $\text{\AA}$  component wavelength light source. A schematic of the interferometer system is shown in Fig. 2.

A detailed description of the construction, modification and operation of the interferometer can be found in Refs. 28, 11, 29. The basic working principle of the interferometer is outlined below.

Light shines through the input mirror (Fig. 2) which is so placed as to reflect the light towards the collimating parabolic mirror 1. It is then divided into two portions at splitter 1, one travels through the compensation chamber and onto mirror 2, while the other via mirror 1 passes through the test section. The two beams then rejoin at splitter 2 and form interference patterns depending on the optical path lengths each has travelled. Parabolic mirror 2 then sends the image through the output mirror to the camera. Inside the camera are located a 60-40 beam splitter, a plane mirror and two line-filters to separate out the component wavelengths. The film used was Kodak Royal X Pan (1250 ASA). DK-50 proved to be the proper developer with a developing time of about 8 minutes.

The attachment of the ruby laser directly onto the frame of the interferometer greatly reduced the difficulty of adjustment (Ref. 29). As has been noticed before (Ref. 11), air currents and temperature variations have significant effects on the orientation of the fringes. Although the interferometer is covered by canvas and foam sponge, it is still subject to temperature gradients. The temperature rise is attributed to the heat generated by the surrounding electronic equipment and the white light source used in setting and focussing the central order fringes. In order to minimize the movements of the fringes, the use of the white light source is restricted and the air-conditioner is shut off to avoid air currents prior to each run. The ultimate way to ensure stable fringe settings might be an insulated housing for the interferometer.

### 3.3 Velocity Measurement

Accurate measurement of the shock velocity is necessary in order to provide a precise shock Mach number for the theoretical calculations.

As will be shown later, Mach number has a significant effect in determining the atom-atom collision excitation cross-section constant. A schematic circuit diagram for velocity measurement is illustrated in Fig. 3.

As mentioned before (Sec. 3.1), there are ports located along the channel and in the test section of the tube. These ports are used to house piezoelectric pressure transducers (Atlantic Research type LD-25) to monitor the arrival of the incident shock wave. Their outputs are amplified and used to start and stop electronic counters thereby giving several velocity measurements of the shock as it travels along the channel. From the velocity measurements it is possible to determine the shock-wave attenuation. At a shock Mach number  $M_s \sim 16$  travelling into argon at 5 torr, the attenuation is about 0.7% per meter while at  $M_s \sim 15$  in 5 torr krypton, it is about 1% per meter. That is, the attenuation of the shock wave is more severe at the lower Mach number runs in krypton than at the higher Mach number runs in argon. A detailed boundary layer analysis would probably yield the reasons to explain these facts.

Even though the shock wave velocity history along the channel was known, the velocity measurement taken across stations I and J (Fig. 3) was used to determine the incident shock Mach number at the test section. This was done for consistency. A Kistler pressure transducer was used at station M, right at the centre of the test section windows, to record the pressure history of the shock induced flow. Typical pressure traces for argon and krypton runs are shown in Fig. 4. Figure 4a shows the pressure history of a shock wave  $M_s = 15.9$  travelling into 5.14 torr of argon. The upward shift of the trace indicates the arrival of the shock wave. It is not possible to pinpoint the exact location of the ionization shock front from the pressure trace as the ionization relaxation time is only about 4  $\mu$ sec which is well within the rise time of about 10  $\mu$ sec for the pressure transducer. The symbol S represents the positions of both the translation and ionization shock fronts. From the trace the pressure behind the shock front has an average value of about 1700 torr over the flow period. The predicted value by assuming the flow in ionization equilibrium without considering radiation losses is 1880 torr. The total test time available is estimated to be about 200  $\mu$ sec for this case including real gas and viscous effects but not the turbulent diffusion of the contact front. Experiments show that the actual test time for the conditions studied is only about 100  $\mu$ sec. It is very difficult to accurately locate the position of the contact front on the pressure trace as the pressure across the contact front is constant. Nevertheless the beginnings of the contact front at 100  $\mu$ sec are so indicated. Figure 4b shows the pressure history of a shock wave at  $M_s = 15.0$  travelling into 5.15 torr of krypton. A pressure jump of about 280 times is expected and shows up accordingly in the trace. The fluctuations of the filtered pressure trace probably come about mainly from the natural frequencies associated with the transducer diaphragm and cannot be explained in detail as relating to the flow.

### 3.4 Admission of Test Gases and Impurities

The test gases used were of the highest purity level available commercially. The argon test gas had a quoted purity level of 99.9998%, whereas that of the krypton test gas was 99.995%. The higher grade argon did not have any noticeable effects in reducing shock wave instability. Neither did the admission of the test gas through ports located upstream

or downstream of the tube or purging the whole tube with test gas before runs have any influence on stability. The initial pressure of the test gas was monitored by a Wallace & Tiernan gauge (0-50 torr range) and a more accurate measurement of the initial pressure was made using an oil manometer.

For the runs that involved the addition of hydrogen as an impurity, the technique used by Brimelow (Ref. 29) was employed. The same technique, however, proved unsuitable for admitting water vapour.

It was found that the water when exposed to low pressure will evaporate, cool and freeze. The ice thus formed will stay in the solid state for a long time under low pressure. A simple device was used later to introduce water vapour. A measured amount of distilled water was put inside a small metal capsule which was then lowered into liquid nitrogen. The water was frozen almost instantly. The capsule was then connected to an inlet with a valve near the evacuated test section (station J, Fig. 3). The valve on the inlet was opened and since the volume of the capsule was very small compared with the tube, the pressure inside was down to that of the tube in a very short time. The water inside the capsule was still frozen and presumably very little of it was lost by evaporation. The valve was then shut and the capsule heated to vaporize the water. At the same time the pumps were shut off and part of the test gas was let into the tube and monitored by a McLeod gauge. The valve was opened again to let in the water vapour. Some pressure measurements from the McLeod gauge are given in Table 1.

There are a few things worth noting from these measurements. First, not all the water inside the capsule was converted to water vapour. For example, if 0.5 ml of water were all vaporized, then we would have a measurement of  $600\mu$  instead of  $250\mu$ . Second, as can be seen from Table 1, all the readings are decreasing with time. This probably indicates that part of the water vapour introduced was being adsorbed by the shock tube walls forming molecular layers which could not be measured by the pressure gauge. The reason for introducing part of the test gas first and then water vapour was to saturate the wall surfaces with the test gas thereby hopefully allowing all the water vapour to be part of the test gas. As can be seen, this was not the case. Apparently, water vapour has a tendency of displacing all other gas molecules that cling to the wall surface. The previously mentioned mass spectrometric study seems to support the above concept.

Since there is no accurate means in the present instrumentation equipment of measuring the exact amount of water vapour in the test gas mixture, the last readings in Table 1 were used. This is by no means precise for when the balance of the test gas was introduced, a purging effect could take place and possibly some of the adsorbed water vapour evolved. However, as the present experiments were meant to be qualitative, the readings chosen will probably serve the purpose.

For one experiment, a thin coating of sodium chloride crystals was grown on the bottom side of the tube in the test section before the run. A normal saline solution was applied inside the tube and then the pressure inside was lowered slowly by controlled vacuum pumping. As the water vaporized, a thin and uniform coating was formed on the test-section lower wall (Fig. 5). The results will be discussed in the subsequent sections.

#### 4. ANALYSIS OF INTERFEROGRAMS

Basically, an interferogram consists of bright and dark fringes as shown in Fig. 6. Sequential numbers are assigned to the fringes as shown. It gives a relative measurement of refractive index between a reference and an unknown region. The  $(x, y)$ -plane consists of a pre-shock region, a translational shock front S, an ionization relaxation region  $X_E$ , an electron cascade front E and a post-shock region. The overall shock wave SE is moving to the left into the gas at rest.

The refractive index of a gas is related to its density by (Ref. 31)

$$(n - 1) = \sum_s K_s \rho_s \quad (4.1)$$

where  $n$  is the refractive index,

$K_s$  is the Gladstone-Dale constant for species 's',  
 $\rho_s$  is the corresponding density for species 's',

and subscript s denotes the components of the gas. in the case of a singly ionized monatomic gas that consists of neutral atoms, ions and electrons. The contributions of the electronically excited atoms to the refractive index are not included (Ref. 11). In the runs that involve hydrogen as a small impurity, its contributions to the refractive index were neglected.

As can be seen from the pre-shock region in Fig. 6, the density there is constant so there is no change in refractive index and the fringes show up as uniformly horizontal. The almost discontinuous downward shift of fringes signifies the location of the incident translational shock front. This is followed by a region where atom-atom collisions take place. As this process is not very efficient in producing electrons (i.e., the flow properties are change very slowly), the change of refractive index in this region is very slow and as a result the fringes gradually shift upward. As more and more electrons are formed, they become very effective collision partners and a rapid cascading of electrons occurs. This results in a rapid change in the refractive index and the fringes correspondingly rise suddenly.

Fringe shifts make it possible to measure the total plasma density  $\rho$  and the electron (ion) number density  $n_e$ . The fringe shifts are defined as the difference of fringe number (or orders of interference) at a particular location where the original fringe is being displaced by a new fringe. For example if the location of point X (Fig. 6) was originally occupied by fringe No. 15 and now that location registers fringe No. 13, then at that location, there is a fringe shift of 2. The nondimensional (normalized by the fringe spacing 5 to 6 or 6 to 7, say) fringe shift,  $S$ , is related to the change of refractive index by (Ref. 29)

$$S = \frac{1}{\lambda} (n_j - n_i) \quad (4.2)$$

or

$$S = \frac{1}{\lambda} [(n_j - 1) - (n_i - 1)] \quad (4.3)$$

where  $L$  is the distance (10.16 cm) the light source travelled across the test section,

$\lambda$  is the wavelength of the light source expressed in cm and subscripts  $i, j$  denote the reference and investigated regions, respectively.

Expanded for the case of a singly ionized plasma, Eq. 4.1 becomes (Ref. 32)

$$(n - 1) = \rho [K_A(1 - \alpha) + K_I \alpha] - \frac{\omega_p^2}{2\omega^2} \quad (4.4)$$

where  $K_A$  - Gladstone-Dale constant for atoms,

$K_I$  - Gladstone-Dale constant for ions,

$\alpha$  - degree of ionization,

$\omega_p$  - plasma frequency,

and  $\omega$  - angular frequency.

Equation 4.4 can also be expressed as

$$(n - 1) = \rho K_A - \alpha \left[ (K_A - K_I) + \frac{4.485 \times 10^{-14}}{m_a} \lambda^2 \right] \quad (4.5)$$

where  $m_a$  is the mass of atom.

After some algebraic manipulation of Eqs. 4.3 and 4.5,

$$\rho_j = \rho_i + \frac{C_1 S_2 \lambda_2 - C_2 S_1 \lambda_1}{L K} \quad (4.6)$$

and

$$n_{ej} = n_{ei} + \frac{K_{A1} S_2 \lambda_2 - K_{A2} S_1 \lambda_1}{L K m_a} \quad (4.7)$$

where  $n_e$  - electron number density,

$$C_1 = (K_A - K_I)_1 + \frac{4.485 \times 10^{-14} \lambda_1^2}{m_a}$$

$$C_2 = (K_A - K_I)_2 + \frac{4.485 \times 10^{-14} \lambda_2^2}{m_a}$$

$$K = C_1 K_{A2} - C_2 K_{A1}$$

and subscripts 1 and 2 correspond to wavelengths  $\lambda_1$  ( $6943.0 \times 10^{-8}$  cm) and  $\lambda_2$  ( $3471.5 \times 10^{-8}$  cm) respectively. The values of the constants for argon and krypton in these equations are listed in Table 2.

Ideally, if we know the density and electron number density in the reference region, and the Gladstone-Dale constants of all the constituents in the unknown region, then by measuring fringe shifts at points of interest, we can calculate the density and electron number density at those points. However, due to optical imperfections there may be some fictitious fringe shifts. The no-flow interferograms, which are taken immediately before firing, together with the flow interferograms, will provide the true fringe shifts, and thus the actual changes in flow properties can be calculated.

#### 4.1 Gladstone-Dale Constants

As noted in Sec. 4, a knowledge of the Gladstone-Dale constants for all the species in the plasma is essential in determining the changes in flow properties. Peck and Fisher (Ref. 33) used a Michelson interferometer to measure the refractivity of argon and came up with a dispersion formula for argon. Chashchina and Shreider (Ref. 34) used the method of spectral line shift to determine index of refraction for krypton and a dispersion formula was also derived. Using Cauchy's dispersion equation (Ref. 35) for krypton, the refractive index obtained was slightly different, but the overall results in density and electron number density evaluated are almost the same. Expressions for the free-electron refractive index can be found in Refs. 11 and 36. Following the expression for free electrons in Ref. 36, a constant of  $4.485 \times 10^{-14} n_e \lambda^2$  was obtained and used in Sec. 4, Eq. 4.5. This value differs from that given in Ref. 36 but agrees with Ref. 11.

The values for the argon and krypton ions, however, are not that well agreed upon. Alpher and White (Ref. 36) used a Slater screening-constant theory and calculated the refractive index of the argon ion to be 0.67 times that of the neutral atom. Later investigators (Refs. 11, 26, 37) all obtained a value of 0.72 using the same theory. Bristow (Ref. 11) did an experimental determination of the polarizability for singly ionized argon and obtained a ratio of 0.65 for the argon ion to the argon atom. However, the value obtained by Alpher and White is still being widely used (Refs. 26, 30, 38). Iggra (Ref. 38) compared the resulting density profiles by using various ratios from 0.25 to 1.0 and concluded that the difference is very small.

Since there is no experimental result available for the krypton ion and using Iggra's comparison, the ratio of the index of refraction of the krypton ion to its atom was taken to be 0.75, as calculated by using Slater screening-constant theory. It should be noted that Meiners and Weiss (Ref. 26) used the ratio of 1 in their calculation.

#### 4.2 Digitizing Equipment

The present scheme of analyzing interferograms was developed by Whitten (Ref. 29). It requires a transformation of the fringe locations into digital form with respect to a chosen reference point. For example, if we choose a particular point in an interferogram as the reference point and assign it to be the origin of an  $(x, y)$ -coordinate system, then the fringes can be thought of as lines or loci of points. Figure 7a shows an interferogram of a shock wave travelling from right to left. The pre-shock region, the translational shock front, the ionization relaxation region,

the electron cascade front and the radiative cooling region can all be seen clearly. Cross-hairs are located 8.2 cm apart and can be used as reference points. The cross-hair at the lower right hand corner of this interferogram was chosen as one of the reference points and also as the origin of an  $(x,y)$ -coordinate system. The corresponding digitized version of the pre-shock region, the translational shock front, the ionization relaxation region, the electron cascade front, the radiative cooling region and the reference point (origin) are shown in Fig. 7b. With all four interferograms (2 no-flow and 2 flow) of one experiment digitized in this fashion with respect to the same reference point (origin), we can determine the actual fringe shift when the same  $(x,y)$ -coordinate of any point in the flow and no-flow pictures is compared.

To transform fringes into digital form, a digitizer was used. First, it involves picking a common reference point in all four interferograms and in this case, the cross-hairs were used. Then a hand-held cursor is used to trace the fringes, and their locations with respect to the reference point are recorded directly on a magnetic tape. The recorded data are later transferred from tape onto cards. An IBM 1800 Plotter is then used to reproduce the digitized version of the interferograms. There are of course some errors in tracing the exact locations of fringes. By comparing the digitized and original interferograms, we can pick out the points that are not aligned with the original. Since the points are in digital form on cards already, they can be corrected and the error reduced until a good reproduction is obtained. The original interferograms are enlarged to about twice their actual size which makes the whole digitizing and correction procedure much easier.

The whole set of points are then linearly interpolated into uniform steps. Fringe numbers (orders) are also interpolated and assigned to each  $(x,y)$ -coordinate. With the flow and no-flow pictures at the two wavelengths now digitized and fringe numbers assigned, fringe shifts at any point can be calculated and in turn the changes in the flow properties at that point. The entire flow region is then known.

##### 5. RESULTS AND DISCUSSIONS

Bristow (Ref. 11) first observed that in high Mach number ( $M_S \gtrsim 15$ ) argon runs, a complex system of flow disturbances persist. Figure 8 shows two interferograms taken simultaneously using two wavelengths, 6943.0 Å and 3471.5 Å. An incident shock, Mach number  $M_S = 14.7$ , is moving from right to left into argon at an initial pressure  $P_1 = 4.08$  torr and temperature  $T_1 = 298.0$  K. Clearly seen are the sinusoidal-type oscillations of the translational shock front S, where the fringes change abruptly, followed by a relaxation region, terminating in the electron-cascade front E, followed by disturbances in the fringes at this front and beyond into the quasi-equilibrium region. Subsequent investigators (Refs. 29,30,38) using the same experimental facilities all reported similar findings. Figure 9 shows an interferogram of a shock wave at  $M_S = 15.2$  travelling from right to left into the krypton test gas initially at  $P_1 = 5.07$  torr and  $T_1 = 295.4$  K. Evidently, the same type of disturbances also exist here. Other investigators (Refs. 22,36) who used a rotating mirror camera to record time-resolved dual-wavelength interferograms of the ionized argon flow, did not come across this phenomenon. The major apparent difference

was in the cross-sections of the shock tubes. Alpher and White (Ref. 36) used a tube 8.25 cm x 8.25 cm, while Oettinger and Bershad (Ref. 22) used a tube 5 cm x 5 cm. The UTIAS tube has a cross-section of 10 cm x 18 cm.

Morse and Ingrad (Ref. 39) have treated the problem of amplification of acoustic disturbances in a collision-dominated plasma where initially the electron temperature  $T_e$  is much higher than the heavy particle temperature  $T_a$ . In our case, immediately behind the translational shock front in ionizing krypton and argon, the reverse is true (see Fig. 10) but the temperature difference between electrons and heavy particles is large. Based on this fact, Bristow postulated that such a condition may be favourable to generating ion-acoustic disturbances. Since the calculations by Belozerov and Measures (Ref. 40) for strong shocks into hydrogen have shown that the electron temperature is essentially the same as the heavy particle temperature in the post-shock relaxation region, Bristow then added a small percentage of hydrogen to the argon test gas for the purpose of reducing the temperature difference between the electrons and the heavy particles. As will be shown later, the addition of hydrogen had a very significant effect.

But the results obtained by Whitten (Ref. 29) and Brimelow (Ref. 30) at lower Mach number argon runs ( $M_s \sim 13$ ), disagreed with Bristow's postulate. Figure 11 shows two simultaneous interferograms of a shock wave ( $M_s = 13.0$ ) travelling from right to left around a sharp corner in ionizing argon with an initial pressure and temperature of 5.01 torr and 296.8 K, respectively. Disregarding the effects of the expansion wave at the corner, we can see that in the free stream, the translational shock front is planar, the subsequent ionization relaxation region and the electron cascade front are all stable. Figure 12 shows the result at a higher Mach number ( $M_s = 16.1$ ) argon run. A comparison of Figs. 11, 8 and 12 reveals that as the incident shock Mach number increases, or the degree of ionization increases, the more severe become the disturbances. This strongly suggests that the disturbances observed are associated with significant ionization. Figure 13c shows a strong shock wave ( $M_s = 16.6$ ) travelling into nitrogen at an initial pressure  $P_1 = 2.26$  torr. Nitrogen is dissociated but not ionized in this case. As can be seen, the flow is stable and free of any disturbances. As further proof that shock wave disturbances are associated with significant ionization only, series of runs were carried out using krypton as the test gas. Krypton can be readily ionized and, as can be seen from Fig. 9, the disturbances are produced as expected. The above mentioned experiments were all conducted in the same manner using the same facility.

In Ref. 21, there are some detailed discussions on the factors affecting the theoretically calculated relaxation length,  $X_E$  (that is, the distance between the shock front  $S$  to the point of maximum electron number density  $E$ , see Fig. 6). It is shown in Ref. 21 that for a fixed shock Mach number  $M_s$  and an initial pressure  $P_1$ ,  $X_E$  theory =  $X_E (S_{a-a}^*, S_{e-a}^*, Q_{ea}, Q_{ei}, Q_R)$ . That is, the relaxation length depends on the atom-atom excitation collision cross-section constant, the electron atom inelastic collision cross-section constant, the electron atom momentum transfer cross-section, the electron ion momentum transfer cross-section and the rate of radiation energy loss. A study of their relative importance shows that  $S_{a-a}^*$  is the main and most sensitive factor in calculating  $X_E$ .

Based on the experimental data from pure test-gas runs and with hydrogen impurities, best-fit values were obtained of  $S_{\text{Ar}-\text{Ar}}^*$  for argon,  $S_{\text{Ar}-\text{Ar}}^* = 1.0 \times 10^{-19} \text{ cm}^2/\text{eV}$ , and for krypton,  $S_{\text{Kr}-\text{Kr}}^* = 1.2 \times 10^{-19} \text{ cm}^2/\text{eV}$ . The available information in the relatively long-duration quasi-equilibrium region helped in the choice of the radiation model. The initial conditions for the cases studied are given in Table 3. Some representative results are given below. Additional results can be found in Appendix A.

### 5.1 Pure Argon

Figure 14 shows the interferogram for Case 1, Table 3, and Fig. 15 shows the corresponding plot of the nondimensional electron number density  $n_e/n_{e,E}$  through the shock wave transition and beyond, as well as the nondimensional density  $\rho/\rho_E$ . As can be seen in Fig. 14, the translational shock front is sinusoidal and disturbances show up as wavy fringes. The lower half of the shock front appears unusually thick owing to nonplanarity. It substantiates the hypothesis that the shock wave is not one-dimensional and may even be three-dimensional in nature. As the translational shock fronts always show up sinusoidal in shape (Figs. 8, 9, 12, 13 and 14), it is very possible that the fronts are also wavy in a direction normal to the optical viewing path. To avoid non-planar effects on the shock front, measurements were taken in the most quiescent regions which usually also avoided the major oscillations through the relaxation region and beyond.

The post shock values of  $n_e/n_{e,E}$  in Fig. 15 are also oscillatory and reflect the waviness of the fringes in Fig. 14, as expected. The interferometric data points were taken 1 mm apart for convenience and more or fewer points can be evaluated depending on the work required.

The position  $X = 0$  (Fig. 15) is where the translational shock front is located. The position  $X = X_E$ , where  $n_e/n_{e,E} = 1$  is the position of the electron cascade front or the end of the transition region. Here the flow quantities achieve their maximum equilibrium values. Radiation losses are insignificant in this region but beyond this point radiation losses become important and the electron number density falls. The fits to the experimental data of  $n_e$  and  $\rho$  are quite reasonable despite their oscillations. The experimental relaxation length is 2.0 cm compared with the theoretically determined value of 2.1 cm when the value of  $S_{\text{Ar}-\text{Ar}}^*$  is chosen to be  $1.0 \times 10^{-19} \text{ cm}^2/\text{eV}$ . Figure 16 shows a plot of the nondimensional degree of ionization  $\alpha/\alpha_E$  with distance  $X$ . The post shock values after 3 cm are in particularly good agreement with the analysis. The effects of radiation losses or radiative cooling are very much in evidence and lend support to the choice of the radiation-loss model.

The fact that an error of  $\pm 0.3$  in the measured Mach number was possible (as discussed in Sec. 5.5) leads to the result that the determined value of  $S_{\text{Ar}-\text{Ar}}^*$  will change slightly. The measured Mach number for this case is  $M_s = 15.9$  (solid line). Two additional curves are plotted for  $M_s = 16.2$  (dashed) and 15.6 (dot-dashed). In order to obtain a best fit to the interferometric data, the corresponding  $S_{\text{Ar}-\text{Ar}}^*$  values have to be changed to  $0.9 \times 10^{-19} \text{ cm}^2/\text{eV}$  and  $1.1 \times 10^{-19} \text{ cm}^2/\text{eV}$ , respectively. Since the equilibrium (real gas without radiation) values for  $M_s = 15.9$  were used for normalizing, the three curves appear separated. Only this case was used to demonstrate the effects of a possible error in Mach number on the effective value of  $S_{\text{Ar}-\text{Ar}}^*$ . The error bars shown in Figs. 15, 16 and in subsequent cases are due to fringe location reading errors only as will be discussed

later in Sec. 5.5. Table 4 gives the equilibrium values of  $\rho_E$ ,  $n_{e,E}$  and  $\alpha_E$  for the cases considered.

Case 2 (Figs. 17, 18) has similar initial conditions to Case 1 (see Table 3) and, as expected, the results are also similar. The experimentally measured relaxation length (1.9 cm) compares favourably with the theoretically determined value (2.0 cm). The oscillations of data points, especially in the post-shock region, are very much in evidence due to wavy fringes in the interferograms. The measured maximum electron number density (degree of ionization) overshoots the theoretical value, but in general, the agreement is reasonable. Case 3 (Figs. 19, 20) has a slightly higher Mach number and as a result the relaxation length is shorter (1.7 cm for theory and 1.8 cm for experiment). Despite the oscillations, the agreement between theory and experiment is quite good. It should be noted that although the agreement between the experimental results and the analysis for the above cases is fair to good, it is not so for Case 4 (Figs. 21, 22) and Case 5 (Figs. 23, 24). Figures 21 and 22 show the results for a shock Mach number  $M_S = 13.0$ . It can be seen that the theoretical and interferometrically measured relaxation length differ by 2.0 cm over a length of about 11 cm. One probable reason for this is that at lower Mach number the changes of density and electron number density are relatively small and as a result the changes in refractive index become the same order as the errors associated with the measurements. Figures 23 and 24 (Case 5) show the results of a higher Mach number run ( $M_S = 17.2$ ). The agreement in the quasi-equilibrium region is quite reasonable, but not for the relaxation length. The maximum electron number density measured and calculated are also in poor agreement. Enomoto (Ref. 8) pointed out that for higher Mach number runs, the relaxation time (length) is significantly shortened when wall-boundary-layer effects are included. The lower initial pressure may also contribute to the shortening of relaxation length. As mentioned before, the main impurities in the desorbed gases consist of water vapour, air and some hydrocarbons. The lower the initial pressure, the higher the percentage of water vapour in the test gas. As will be discussed later, water vapour has a significant effect in reducing the relaxation length. This probably helps to explain the discrepancy in the calculated and measured relaxation length. However, the reason for the large discrepancy in the maximum electron number density for this case is still unknown. It may be necessary to fit a new value of the atom-atom collision excitation cross-section constant for higher (and lower) shock Mach number. Consequently, until the values of the quantities used to determine  $X_E$  (see Sec. 5) are accurately known, we cannot claim that  $S_{Ar-Ar}^*$  is a universal constant.

Table 5 lists the predicted and measured relaxation lengths for the cases studied. The comparisons between theory and experiment are quite good for Cases 1, 2 and 3. For Case 4 where the shock Mach number is much lower than the others, the agreement is not so good. Case 5 has a lower initial pressure and a higher Mach number. The difference between predicted and measured relaxation length is quite severe. The effects of wall-boundary-layer suggested by Enomoto (Ref. 8) and the possibility of higher impurity level in the test gas probably cause the discrepancy.

## 5.2 Pure Krypton

Experimental results for krypton are quite sparse. Hopefully, the present data can provide additional valuable information. Figure 25 shows an interferogram of a shock wave moving into 5.07 torr of krypton at a Mach number

$M_s = 15.2$  (Case 6). The sinusoidal shock front is very much in evidence and so is the varying shock-front thickness which further substantiates that the wave is in fact nonplanar. The disturbances in the electron cascade front are strikingly similar to those in pure argon runs.

The closeness of the electron cascade front to the translational shock wave at the wall is also worth noting. Figures 26 and 27 show the plots of the normalized electron number density, density and degree of ionization profiles. The agreement between the interferometrically measured results and analysis is very good for the chosen value of the atom-atom collisional excitation cross-section constant  $S_{Kr-Kr}^* = 1.2 \times 10^{-19} \text{ cm}^2/\text{eV}$ . The oscillation of the data points correspond with the wavy fringes due to disturbances and not due to errors in the data reduction. Figures 28 and 29 show the results for another krypton case. The length of the quasi-equilibrium region provides information on the choice of the radiation-loss model used in the theoretical calculation. A comparison of the measured and calculated relaxation lengths can be found in Table 5. As can be seen, the agreement between theory and experiment for both cases are very good.

### 5.3 Impurities

Impurities have long been important factors in the study of shock-wave structure and stability. Petschek and Byron (Ref. 1) and Harwell and Jahn (Ref. 2) all observed that impurities have a profound effect on the rate of ionization and probably provide the initial mechanism leading to equilibrium ionization. However, little agreement exists on which impurities have or have not an effect on the ionization rate.

Morgan and Morrison (Ref. 4) using a relatively simple theory and based on some characteristic excitation energy tried to fit Harwell and Jahn's (Ref. 2) experimental results. They hypothesized that a nitrogen impurity had a definite effect whereas oxygen and hydrogen impurities had no significant effects on the rate of ionization. The results shown here (from Ref. 11) contradict part of their hypothesis. Figure 13a shows an interferogram of a shock wave travelling into argon at an initial pressure of 2.85 torr with an oxygen impurity (0.46% by pressure). The disturbances are very much in evidence and the interferogram resembles a pure-gas run (Figs. 8, 9, 12 and 14). A comparison of the measured and calculated (assuming pure argon as the test gas) relaxation lengths shows the agreement to be reasonable. This proves that an oxygen impurity has no significant effect on shock-wave structure and stability and agrees with Morgan and Morrison's hypothesis. Figure 13b shows an interferogram of a Mach 17.2 shock wave travelling into argon with a helium impurity. The results are also similar to those for pure argon runs and that a helium impurity has no significant effect on either shock wave structure or stability. Figure 13c shows a strong shock wave travelling into nitrogen. The test gas was dissociated but not ionized. It can be seen clearly that the flow behind the shock front is very stable as expected. No experiment was done using nitrogen as an impurity in argon as a test gas, owing to the negative results from Fig. 13c. It is very doubtful that nitrogen would have any significant effect on argon shock-wave structure and stability. An additional test would clarify this point.

Schneider and Park (Ref. 12) studied experimentally the ionization rates using argon as a test gas with sodium chloride as an impurity. Their

measurements showed that the increase in ionization rate was due to electron detachment of negative chlorine ions produced from the sodium chloride vapour. The present study shows that a hydrogen impurity, which can be readily ionized to produce electrons, increases the ionization rate of argon. Both studies attribute the increase in the ionization rate to the electrons. It has been shown that electrons are very efficient collision partners which can lead to a rapid production of new electrons until equilibrium is achieved. Although it is well known that sodium chloride from the atmosphere can cling to the shock-tube walls during a routine cleanup, our mass spectrometric study failed to reveal any appreciable amounts of sodium chloride in the desorbed gas. As sodium chloride can be easily ionized to produce electrons, one experiment was performed by having sodium chloride crystals on the shock-tube wall. A normal saline solution was brushed onto the shock-tube wall and then by carefully monitoring the vacuum pumps, the pressure inside the tube was lowered slowly. The water evaporated and a rough coating of crystals was formed on the wall surface. It was hoped that when the shock wave travelled over the crystals it would scrub, heat and ionize the salt which might affect the shock structure. However, upon examination of the resulting interferogram (Fig. 30), it did not exhibit features different from a normal pure argon run.

### 5.3.1 Hydrogen Impurity

Bristow (Ref. 11) first discussed the use of hydrogen addition with a view to eliminate the inexplicable flow disturbances both within and behind the shock-wave structure. Figure 31 shows five interferograms of similar shock strength and initial conditions. They only differ in the amount of hydrogen addition to the test gas. Figure 31a shows the run with an almost pure argon test gas; the rest all have different amounts of hydrogen addition. As the amount of hydrogen added to the test gas increases, the flow disturbances diminish and the relaxation length shrinks. It was found by Bristow (Ref. 11) that 0.4% (by pressure) of hydrogen addition to the argon test gas can completely eliminate the disturbances. Figures 31d and 31e, which represent two runs with 0.5% and 1% hydrogen addition, respectively, show a straight translational shock front along with a stable relaxation region, electron cascade front and radiative cooling region compared to Fig. 31a, which has almost no hydrogen addition. Besides stabilizing the flow, hydrogen also shortens the entire shock transition. Figure 31 also illustrates how the relaxation length decreases as the amount of hydrogen addition increases. It was found that by adding a small amount of hydrogen (0.4% by pressure) as an impurity to the argon test gas, the relaxation length was reduced to 1/3 of the pure-gas value. This result is quite different from the argon-xenon mixtures used by Kelly (Ref. 9). He showed that the addition of 0.1% or 0.48% of xenon to the argon test gas did not substantially change the relaxation length from that for pure argon. The reason is that the collision excitation cross-section constant for xenon is much smaller than for argon, while the constant for hydrogen is much larger. In addition, the mass of the hydrogen atom is markedly smaller (1/40) than that of argon atom and the ionization energy for atomic hydrogen is lower than that for argon. These three characteristics of a hydrogen impurity in an argon test gas probably account for the large reduction in the relaxation length.

Figure 32 shows a similar comparison of the effects of hydrogen addition to krypton as a test gas. It can be seen that with 0.4% hydrogen impurity in the krypton test gas (Fig. 32b), the flow is the most stable one. Although hydrogen has a similar effect to argon in reducing the relaxation length of

ionizing krypton, it does not completely eliminate the flow disturbances. Furthermore, with more than 0.4% hydrogen added, it seems to enhance or even produce other types of disturbances (Figs. 32c and 32d).

The reason why an addition of hydrogen can stabilize the flow in argon is still unknown at this time. Although pure krypton runs exhibit similar traits as for pure argon runs, the effects of hydrogen addition are not identical as new types of instabilities appear. The reason why hydrogen behaves more favourably with argon but not with krypton is not known. It should be pointed out that although a small addition of a hydrogen impurity in an argon or krypton test gas significantly reduces the relaxation length and eliminates the disturbances, it does not affect the overall flow properties in the quasi-equilibrium region.

Calculations were made for the cases of  $M_s = 16.2$ ,  $P_1 = 5.17$  torr and  $M_s = 17.6$ ,  $P_1 = 3.12$  torr (Cases 8 and 9) and with a small amount of hydrogen (0.4% by pressure) as an impurity in argon. The resulting analytical and experimental density, electron number density and degree of ionization variations through the ionization relaxation and radiative cooling regions are shown in Figs. 33-36. The shock transition values are particularly good for the stronger shock case (Figs. 35 and 36). On the whole, the agreement between the measured and predicted relaxation lengths (see Table 5) and the quasi-equilibrium post-shock value are quite satisfactory. Better agreement might have been obtained by including the appropriate values of the refractive indices for the hydrogen impurity in the interferometric equations (Eqs. 4.6 and 4.7). The assumption of equal velocities and temperatures for the heavy particles of argon and hydrogen in the theory may also contribute some error.

Similar calculations were also made for the cases (Cases 10 and 11) of krypton with 0.38% (by pressure) of added hydrogen impurity. The comparisons of measured and predicted density and electron number density from the pre-shock region through the ionization relaxation and radiation cooling regions are shown in Fig. 37. The ionization relaxation length for this case is 8 mm when measured experimentally and the theory predicted 9 mm (Table 5). Both the measured density and electron number density profiles are below the predicted values. Since the degree of ionization profile is a function of both density and electron number density profile, the measured values overshoot the predicted ones (Fig. 38). The agreement between experiment and theory is much better in Case 11. The measured density profile in Fig. 39 agrees very well with the predicted values. The agreement in the long quasi-equilibrium region is especially good. The interferometrically determined electron number density profile falls slightly short of the predicted values, but the overall trend is in reasonable agreement. Figure 40 shows the corresponding degree of ionization profile and as can be seen, the agreement between theory and experiment is also very good, confirming the choice of the theoretical model.

### 5.3.2 Water Vapour Impurity

The possibility of impurities, especially water vapour, being present on any shock tube surface cannot be disregarded. Even though the wall was cleaned as thoroughly as possible before each run, the presence of water vapour molecules, typically at a density of  $10^4 \text{ cm}^{-2}$  at a pressure of  $10^{-6}$  torr, are always there as shown by our mass spectroscopic study. Schneider and Park (Ref. 13) pointed out that water vapour had no significant effect on the rate of ionization of argon. There is, however, no mention about what other effects water vapour may have.

The use of water vapour as an impurity was originally intended to study wall effects in the ionization relaxation region (Sec. 5.4). The method used for admitting hydrogen impurity was first tried. It involved using a precalibrated, known Wallace-Tiernan gauge volume reservoir to determine the amount of water (by pressure) being admitted into the test gas. It was later found that most of the water vapour remained inside the reservoir. Even the vapour in the test gas probably formed molecular layers of water on the surfaces, which could not be detected by a pressure gauge. Consequently, it was not possible to know the exact amount of water vapour added to the test gas. Figure 41 shows a resulting interferogram when an unknown but "small" amount was presented in the argon test gas. The unstable shock front is moving to the left, leaving behind a non-uniform region. Such disturbances were not observed before. The same experiment was repeated using the reservoir but no water was added. The argon test gas was admitted into the tube via the reservoir. This procedure had not been used before as the test gas was usually admitted through another inlet. The resulting interferogram is shown on Fig. 42. A comparison of Figs. 41 and 42 shows an almost identical disturbance even though the latter one was intended to be a pure argon run. Part of the no-flow region is missing and the reason for its blockage is not clear. It was concluded that perhaps the adsorbed or remaining water inside the gauge reservoir from the previous run must have been driven into the tube when admitting the argon test gas for the second run. When the original method of admitting the argon through another inlet was used again, then the usual interferogram (Fig. 12) was again obtained. Additional experiments using water vapour as an impurity are still being carried out at the present time (Ref. 41). Preliminary results confirm that very small amounts of water vapour added to the argon test gas will produce disturbances similar to those shown in Figs. 41 and 42.

A more efficient method of admitting water vapour was later developed (Sec. 3.4). Although it is still not possible to make an accurate measurement of water vapour concentration in the test gas, a qualitative measurement can be obtained. The difficulty is mainly due to the fact that water vapour tends to adsorb on the surfaces and no simple measuring device is available that can measure the low concentration of water vapour ( $\sim 0.1\%$  of 5 torr by pressure) of interest in the present work.

Figure 43 shows an interferogram of a perfectly stable shock wave in argon. A small amount (0.25 ml) of distilled water was introduced into the shock tube. If all the water turned into vapour then the additional expected pressure would be  $300\mu$ . However, 30 seconds after the water vapour was admitted it indicated only an additional pressure of  $70\mu$ . A reading taken 4 minutes later showed it to be only  $40\mu$ . A possible explanation is that the water vapour was adsorbed on the shock tube walls thereby lowering the pressure. It is seen that a small amount of water vapour added to the argon test gas can stabilize the shock wave and eliminate all disturbances. At the same time, the ionization relaxation length is drastically reduced very much like the effects produced on adding  $\sim 0.5\%$  H<sub>2</sub> (by pressure). This is not surprising, as the water vapour dissociates very readily at the existing temperatures ( $\sim 20,000$ K) and in turn ionized hydrogen is produced.

From the foregoing experiments it appears that sufficient water as an impurity will stabilize an argon shock wave at high shock Mach numbers, just like hydrogen. However, not enough water vapour may give rise to new instabilities. The latter is still under study (Ref. 41). One might conjecture that

the small amounts of water vapour always present in a shock tube could give rise to the instabilities observed in pure monatomic gas runs. Since the size of the shock tube used in the present work is large, it has a much bigger inner surface area compared to the tubes used by Alpher and White (Ref. 36) and Bershader et al (Refs. 5, 22). With a much bigger inner surface area, the amount of adsorbed water vapour is correspondingly increased. Consequently, such disturbances are observed only in the larger tube. By purposely increasing the amount of water vapour addition they are eliminated. Nevertheless, the disturbances shown in Figs. 41 and 42 are of a very different type from those shown in Figs. 8 and 31. Such behaviour would have to be explained by collision theory. Since the data are few, more will be known when the work of Ref. 41 is completed.

#### 5.4 Wall Effects in Relaxation Region

An interesting result was found (Ref. 30) experimentally in the relaxation region near the shock-tube wall as shown very clearly in Fig. 8 for  $\lambda_L = 6943\text{\AA}$ , which is more sensitive to electron density. It is seen that the electron front E moves in towards the translational shock front S near the wall surface. Similar wall effects can also be found when hydrogen (Fig. 31), helium and oxygen (Fig. 13) impurities were added to the argon test gas (Ref. 11). The same effect is also noticed in the krypton runs (Figs. 9 and 32). In the cases with hydrogen as an impurity (Figs. 31 and 32), the relaxation region is shortened so that only a few fringes supply data in the wall-relaxation region, and therefore the change is not so apparent.

The reasons for this premature ionization close to the wall are not clear. One considered possibility was that a gas-surface interaction occurred between the argon plasma and the chromium-plated steel shock tube wall. Two experiments were carried out by Brimelow (Ref. 30) to try to eliminate this possibility. In one, a covering (0.008 cm) of ordinary Sellopac (cellophane) tape was stuck to the wall and in the other a thin tungsten foil (0.003 cm) was fixed to the wall. It was hoped that the tape, being a good electrical insulator, or the tungsten, having a different work function from chromium or steel, might change the electron distribution, if indeed a gas-surface interaction occurred. However, no change was observed. The rough layer of sodium chloride crystals on the tube surface seems to bring the two fronts even closer (Fig. 30). It should be pointed out, however, that only changes were made in the wall surface near the test section. It is doubtful if changes in the wall surface over longer lengths of channel would be more effective. If adsorbed water vapour on the shock-tube walls cause this phenomenon, just as it reduces the relaxation length in the free stream, then it will always be present no matter what the surface may be. One difficulty arises from the fact that near the wall the viscous boundary layer is cold and the degree of ionization is approaching zero. However, at the leading edge right at the translational shock front, although the boundary thickness is approaching zero and the translational temperature is even higher than at the electron cascade front, the electron density is approaching zero. Consequently, it is difficult to give a substantive reason for the approach of the electron cascade front towards the translational shock front near the wall.

## 5.5 Sources of Errors

In Ref. 11 there is a detailed discussion of the sources of error involved in the present type of experimental work. They can be generalized as (1) errors associated in using the interferometric method and (2) errors involved in the measurement of the initial conditions.

In plasma flows with large density gradients, such as the boundary layer, the light rays are refracted and travel over longer optical paths where the plasma refractive index is constantly changing. This introduces errors that must be accounted for. In the shock structure and in the induced quasi-uniform flow such gradients are considered as small. The test section side window boundary layer effects are also neglected in the analysis. Calculation done by Bunting and DeVoto (Ref. 42) on refractive errors involved in interferometric studies showed that the above mentioned errors were relatively smaller than the fringe shift reading error (typically  $\pm 0.08$  in the present study). It is therefore reasonable to neglect such errors in the data reduction. The fact that in the case of a plasma, electrons and heavy particles have opposite effects on light refraction, further reduces possible errors from this source.

Since the locations of fringes are determined visually, it is considered to be a major error source in the data reduction. The more the interferograms are enlarged, the more accurate are the fringe readings. However, since the entire interferogram is evaluated, it is impractical to blow it up to an excessive size. Normally it was enlarged to about 50 cm x 50 cm. A fringe error of  $\pm 0.08$ , which is considered to be generous, was then used to determine the error associated with the flow properties. The error, in the argon cases, was about  $3 \times 10^{-6}$  gm/cm<sup>3</sup> or about 3.5% of the deduced maximum density and  $5 \times 10^{15}/\text{cm}^3$  or 3% of the maximum electron number density when the initial test gas pressure was 5 torr. Since the above errors depend on the initial conditions, they are uniform over the entire flow. The error in the degree of ionization, however, depends on both local density and electron number density, so it varies at different locations and is usually about 0.4% or less. The errors due to fringe readings in the krypton cases are found to have about the same magnitude as those for argon.

The maximum reading error in the initial temperature was  $\pm 0.5^\circ\text{C}$ , and has practically no effect on the calculated post-shock properties.

The measurements of the initial pressure were found to have mainly visual reading errors. A maximum random error of about 1% in the pressure reading was possible. The higher the initial pressure, the lower the error. Igra (Ref. 38) showed that when the maximum possible error in initial pressure was considered, all calculated post-shock properties were within 5% of the nominal values.

The shock arrival was monitored with Atlantic-Research LD-25 pressure transducers which triggered a microsecond timer. Considering both the rise time of the transducers and the timer resolution, the error in the measured time interval is  $\pm 1 \mu\text{sec}$ . Depending on the shock velocity, the Mach number so determined is within  $\pm 0.3$ . Section 5.1 discussed the effect of Mach number on the deduced atom-atom excitation collision cross section. The effects of the Mach number error on the calculated post-shock properties can be seen in Figs. 15 and 16, and it is significant.

Another type of error in the data reduction arises from neglecting the refractive-index effects of the added hydrogen impurities. However, in view of the fair to good agreement between the analysis and the measured data in the cases involving the small amounts of hydrogen impurity (Figs. 33-40), this error is believed to have very little effect.

## 6. CONCLUSIONS

The use of two-wavelength interferometry has proven to be a very effective method for investigating ionizing shock wave structure in monatomic gases. The measurements of total density and electron number density in the relaxation region provided the data for evaluating the atom-atom excitation collision cross-sections for argon and krypton as  $1.0 \times 10^{-19} \text{ cm}^2/\text{eV}$  and  $1.2 \times 10^{-19} \text{ cm}^2/\text{eV}$ , respectively.

The measurements in the radiative cooling region also provided the information required to choose an appropriate theoretical radiation model. It is shown that radiative cooling losses are important for high Mach number runs at higher pressures. The particle velocity, the electron temperature and the atom temperature decrease monotonically throughout the radiative cooling region, whereas the density and pressure increase. The overall agreement between theory and experiment is good.

Oxygen, helium and sodium chloride impurities when added to argon do not seem to have any effect on shock-wave structure and stability.

Owing to the low mass of the hydrogen atom and the large excitation cross-section constants between the hydrogen atom-atom and the hydrogen atom-electron collisions, even a small addition (0.4%) of hydrogen to the test gas drastically reduces the relaxation length. The addition of hydrogen also removes the sinusoidal-type instabilities from the shock front as well as those from the ionization front and the subsequent freestream. How hydrogen removes these instabilities has as yet not been explained, despite the accurate analytical predictions of density, electron concentration, and degree of ionization profiles. It should be noted that the present experiments are not in a Mach number range where real gas effects cause the second derivative of pressure with respect to volume, at constant entropy  $(\partial^2 P / \partial V^2)_S$  to become negative, in violation of the second law of thermodynamics, which may give rise to shock-wave instabilities (Refs. 14-17). Consequently, it must be concluded that the instabilities encountered in the present and earlier research are associated with a significant degree of ionization. This phenomenon is still being investigated.

Water vapour as an added impurity has some very unpredictable effects on the structure and stability of shock waves. While it can stabilize disturbances and reduce the relaxation time like hydrogen, it can also produce new forms of disturbances.

Another unsolved problem is the progression of the cascading electron (ionization) front towards the translational shock front as the shock tube wall is approached. The present interferometric profiles can be considered as very accurate experimental data. As such, it should stimulate additional theoretical research on shock-wave stability and premature ionization near shock tube walls.

REFERENCES

1. Petschek, H.  
Byron, S.  
"Approach to Equilibrium Ionization Behind Strong Shock Waves in Argon", *Annals of Physics*, Vol. 1, No. 3, 270, 1957.
2. Harwell, K. E.  
Jahn, R. G.  
"Initial Ionization Rates in Shock-Heated Argon, Krypton and Xenon", *Physics of Fluids*, Vol. 7, No. 2, 214, 1964.
3. Bond, J. W.  
"Structure of Shock Front in Argon", *Physical Review*, Vol. 105, No. 6, 1683, 1957.
4. Morgan, E. J.  
Morrison, R. D.  
"Ionization Rates Behind Shock Waves in Argon", *Physics of Fluids*, Vol. 8, No. 9, 1608, 1965.
5. Wong, H.  
Bershader, D.  
"Thermal Equilibration Behind an Ionizing Shock", *Journal of Fluid Mechanics*, Vol. 26, Part 3, 459, 1965.
6. Hoffert, M. I.  
Lien, H.  
"Quasi-One-Dimensional Nonequilibrium Gas Dynamics of Partially Ionized Two-Temperature Argon", *Physics of Fluids*, Vol. 10, No. 8, 1769, 1967.
7. Chubb, D. L.  
"Ionizing Shock Structure in a Monatomic Gas", *Physics of Fluids*, Vol. 11, No. 11, 1968.
8. Enomoto, Y.  
"Wall Boundary Layer Effects on Ionizing Shock Structure in Argon", *Journal of the Physical Society of Japan*, Vol. 35, No. 4, 1973.
9. Kelly, A. J.  
"Atom-Atom Ionization Cross Sections of the Noble Gases - Argon, Krypton and Xenon", *Journal of Chemical Physics*, Vol. 45, No. 5, 1723, 1966.
10. McLaren, T. I.  
Hobson, R. M.  
"Initial Ionization Rates and Collision Cross Sections in Shock Heated Argon", *Physics of Fluids*, Vol. 11, No. 10, 2162, 1968.
11. Bristow, M. P. F.  
"An Experimental Determination of the Polarizability for Singly Ionized Argon", *UTIAS Report No. 158*, 1971.
12. Schneider, K. P.  
Park, C.  
"Shock Tube Study of Ionization Rates of NaCl-Contaminated Argon", *Physics of Fluids*, Vol. 18, No. 8, 969, 1975.
13. Mirels, H.  
"Flow Nonuniformity in Shock Tubes Operating at Maximum Test Times", *Physics of Fluids*, Vol. 9, No. 10, 1907, 1966.
14. D'yakov, S. P.  
"The Stability of Shock Wave", *Zhurnal Eksperimental'noi Teoreticheskoi Fiziki*, Vol. 27, No. 3(9), 288, 1954; *A.E.R.E. Lib/Trans.* 648.

15. Swan, G. W.  
Fowles, G. R. "Shock Wave Stability", Physics of Fluids, Vol. 18, No. 1, 28, 1975.

16. Fowles, G. R. "Conditional Stability of Shock Wave - A Criterion for Detonation", Physics of Fluids, Vol. 19, No. 2, 227, 1976.

17. Griffiths, R. W.  
Sandeman, R. J.  
Hornung, H. G. "Stability of Shock Waves in Ionizing and Dissociating Gases", Journal of Physics D: Applied Physics, Vol. 9, 1681, 1976.

18. Levine, M. A. "Turbulent Mixing at the Contact Surface in a Driven Shock Wave", Physics of Fluids, Vol. 13, No. 5, 1166, 1970.

19. Chang, C. T. "Remarks Concerning the Rate of Thermal Ionization of Hydrogen Behind a Strong Shock", Proceedings of the Seventh International Conference on Phenomena in Ionized Gases, Vol. 2, 742, 1965, edited by B. Perovic and D. Tosic.

20. Appleton, J. P.  
Bray, K. N. C. "The Conservation Equations for a Nonequilibrium Plasma", Journal of Fluid Mechanics, Vol. 20, Part 4, 659, 1964.

21. Glass, I. I.  
Liu, W. S. "Effects of Hydrogen Impurities on Shock Structure and Stability in Ionizing Monatomic Gases: I - Argon", to be published in Journal of Fluid Mechanics.

22. Oettinger, P. E.  
Bershader, D. "A Unified Treatment of the Relaxation Phenomena in Radiating Argon Plasma Flows", AIAA Journal, Vol. 5, No. 9, 1625, 1967.

23. Meiners, D.  
Weiss, C. O. "Continuous Emission of Argon, Krypton and Xenon Plasmas", J. Quant. Spectrosc. Radiat. Transfer, Vol. 16, 273, 1976.

24. Kamimoto, G.  
Teshima, K.  
Nishimura, N. "Ionization Relaxation in Shock Heated Argon", Dept. of Aero. Eng., Kyoto University, Japan, CP 36, 1972.

25. Glass, I. I.  
Liu, W. S.  
Tang, F. C. "Effects of Hydrogen Impurities on Shock Structure and Stability in Ionizing Monatomic Gases: II - Krypton", Canadian Journal of Physics, Vol. 55, No. 14, 1269-1279, 1977.

26. Meiners, D.  
Weiss, C. O. "Interferometrische Messung der Thermischen Zustandsgrößen von EdelgasstöBwellenplasmen", Z. Naturforsch, 28 a, 1294, 1973.

27. Boyer, A. G. "Design, Instrumentation and Performance of the UTIAS 4-in x 7-in Hypervelocity Shock Tube", UTIAS Report No. 99, 1965.

28. Hall, J. G. "The Design and Performance of a 9 inch Plate Mach-Zehnder Interferometer", UTIA Report No. 27, 1954.

29. Whitten, B. T. "An Interferometric Investigation of Quasi-Steady Shock-Induced Boundary Layers in Partially Ionized Argon, UTIAS Ph.D. Thesis, 1977.

30. Brimelow, P. I. "An Interferometric Investigation of Shock Structure and Its Induced Shock-Tube Boundary Layer in Ionized Argon", UTIAS Technical Note No. 187, 1974.

31. Alpher, R. A.  
White, D. R. "Optical Refractivity of High-Temperature Gases. I. Effects Resulting from Dissociation of Diatomic Gases", The Physics of Fluids, Vol. 2, No. 2, 153, 1959.

32. Glass, I. I.  
Kawada, H. "Prandtl-Meyer Flow of Dissociated and Ionized Gases", UTIA Report No. 85, 1962.

33. Peck, E. R.  
Fisher, D. J. "Dispersion of Argon", Journal of the Optical Society of America, Vol. 54, No. 11, 1964.

34. Chaschina, G. I.  
Shreider, E. Ya. "Determination of Xenon and Krypton Refractive Indices in the Vacuum Region of the Spectrum", Optics and Spectroscopy, Vol. 27, No. 1, 79, 1969.

35. Kaye, G. W. C.  
Laby, T. H. "Tables of Physical and Chemical Constants", 10th Edition, Longmans, Green and Co.

36. Alpher, R. A.  
White, D. R. "Optical Refractivity of High-Temperature Gases. II. Effects Resulting from Ionization of Monatomic Gases", The Physics of Fluids, Vol. 2, No. 2, 162, 1959.

37. Ascoli, U.  
DeAngelis, A.  
Martellucci, S. "Wavelength Dependence of the Refractive Index of a Plasma in the Optical Region", Il Nuovo Cimento, Vol. XVIII, N. 6, 1960.

38. Igra, O. "An Experimental Investigation of a Nonequilibrium Corner-Expansion Flow of Ionized Argon", UTIAS Report No. 161, 1970.

39. Morse, P. M.  
Ingard, K. U. "Theoretical Acoustics", McGraw-Hill, New York, 1968.

40. Belozerov, A. N.  
Measures, R. M. "Study of the Initial Ionization Process in a Strong Shock Wave", Journal of Fluid Mechanics, Vol. 36, Part 4, 695, 1969.

41. Doubilet, G. "The Effects of Hydrogen and Water-Vapour Impurities on Shock-Wave Stability in Monatomic Gases", UTIAS M.A.Sc. Thesis, 1977.

42. Bunting, J. O.  
Devoto, R. S.

"Shock Tube Study of the Thermal Conductivity  
of Argon", Stanford University, Dept. of Aero-  
nautics and Astronautics, SUDAAR No. 313, 1967.

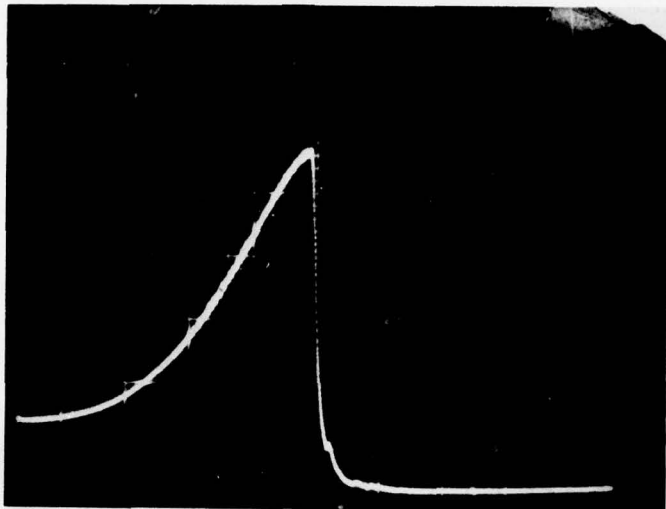


FIGURE 1 DEFLAGRATING COMBUSTION PRESSURE TRACE

$P_{\text{mixture}} = 3.9 \times 10^4 \text{ Torr}$  (15%  $\text{H}_2$  + 7.5%  $\text{O}_2$  + 72.5% He + 5%  $\text{H}_2$ )

$P_{\text{burst}} = 2.3 \times 10^5 \text{ Torr}$

Oscilloscope Setting: Vert: 1 volt/div.  
Horiz: 5 msec/div.

Charge Amplifier Setting : Transducer Sensitivity : 1.09  
Range : 1,000 psi/volt

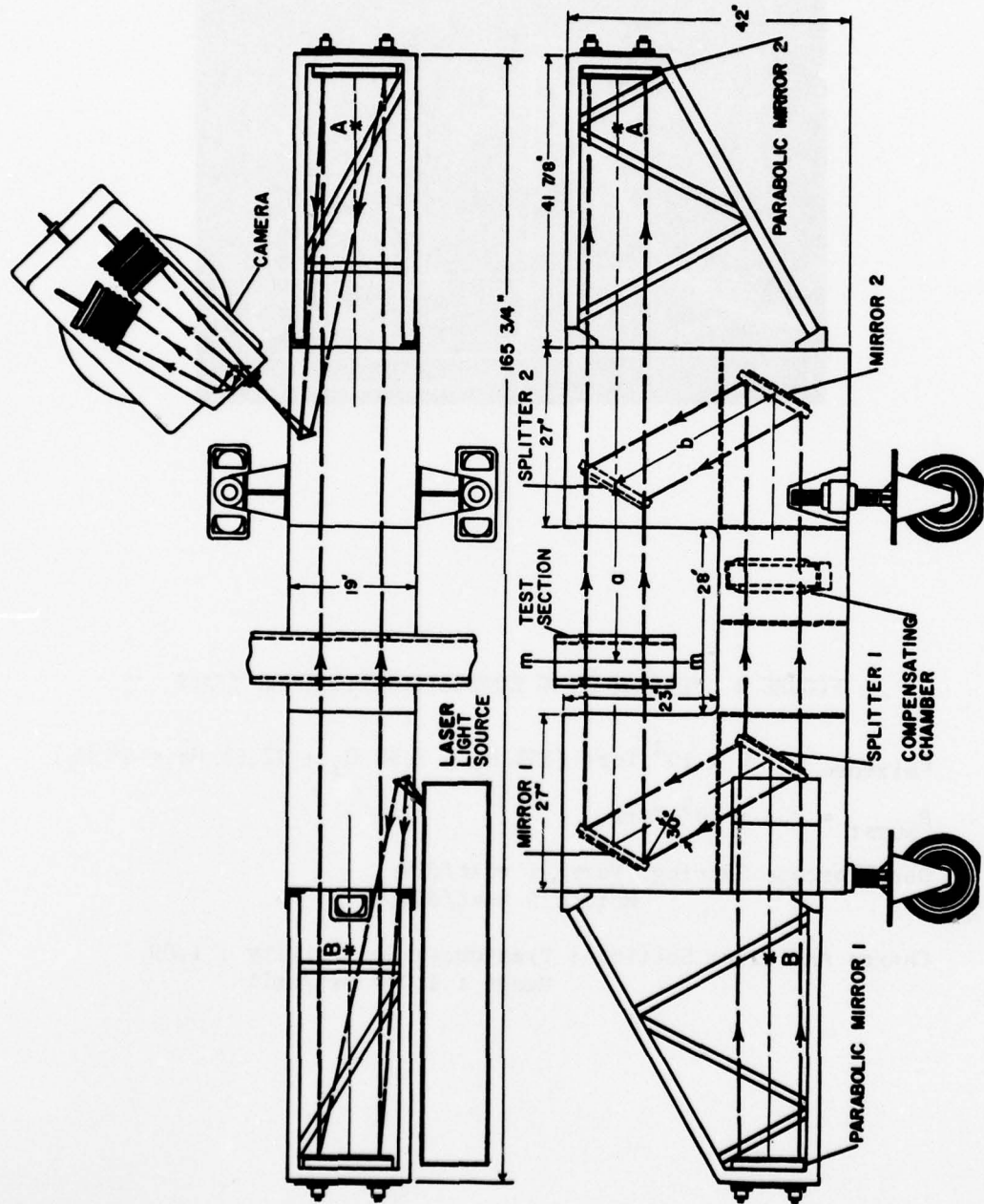
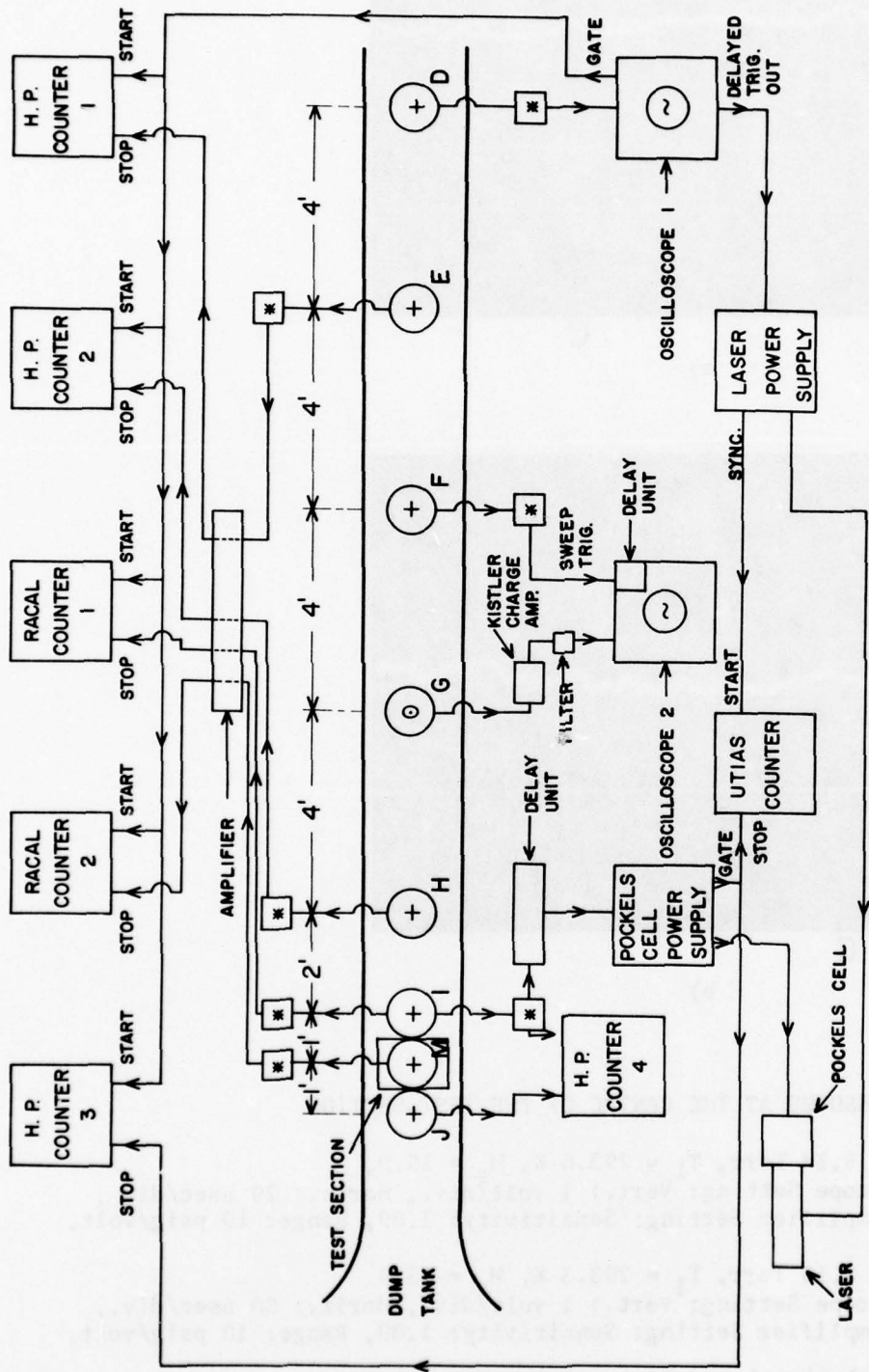


FIGURE 2 SCHEMATIC OF MACH-ZEHNDER INTERFEROMETER



### SYMBOLS

- ⊕ ATLANTIC RESEARCH LD-2S PRESSURE TRANSDUCERS
- ⊖ KISTLER TRANSDUCERS
- ×
 IMPEDANCE MATCHING UNITS

FIGURE 3 SCHEMATIC CIRCUIT DIAGRAM FOR VELOCITY MEASUREMENTS AND LASER LIGHT SOURCE

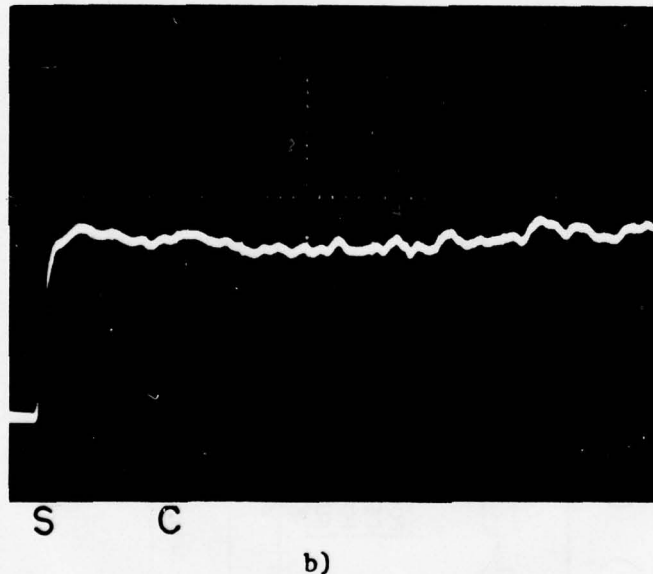
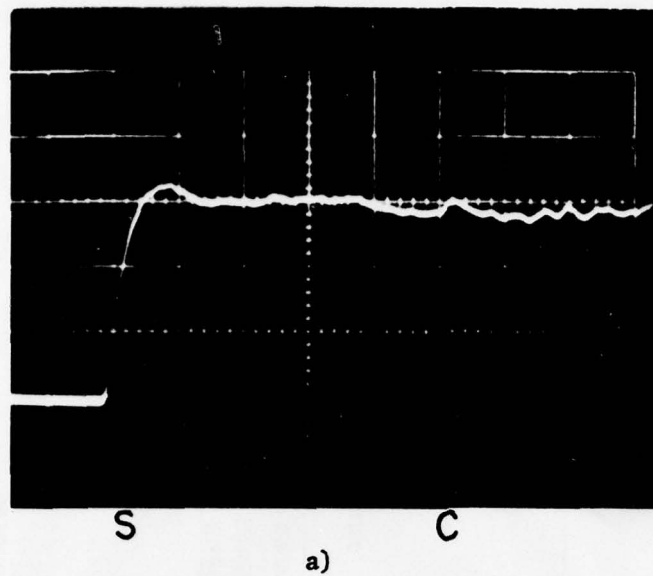


FIGURE 4 FLOW PRESSURES AT THE CENTRE OF THE TEST-SECTION

a) Ar:  $P_1 = 5.14$  Torr,  $T_1 = 293.6$  K,  $M_s = 15.9$ ,  
 Oscilloscope Setting: Vert.: 1 volt/div., Horiz.: 20  $\mu$ sec/div.,  
 Charge Amplifier Setting: Sensitivity: 1.09, Range: 10 psig/volt.

b) Kr:  $P_1 = 5.15$  Torr,  $T_1 = 298.3$  K,  $M_s = 15.0$   
 Oscilloscope Setting: Vert.: 1 volt/div., Horiz.: 50  $\mu$ sec/div.,  
 Charge Amplifier Setting: Sensitivity: 1.09, Range: 10 psig/volt.

S = Translational and Ionizational Shock Front  
 C = Contact Front

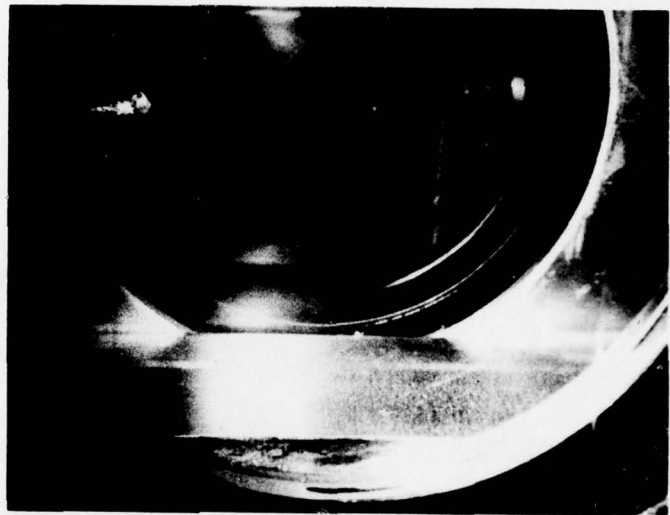
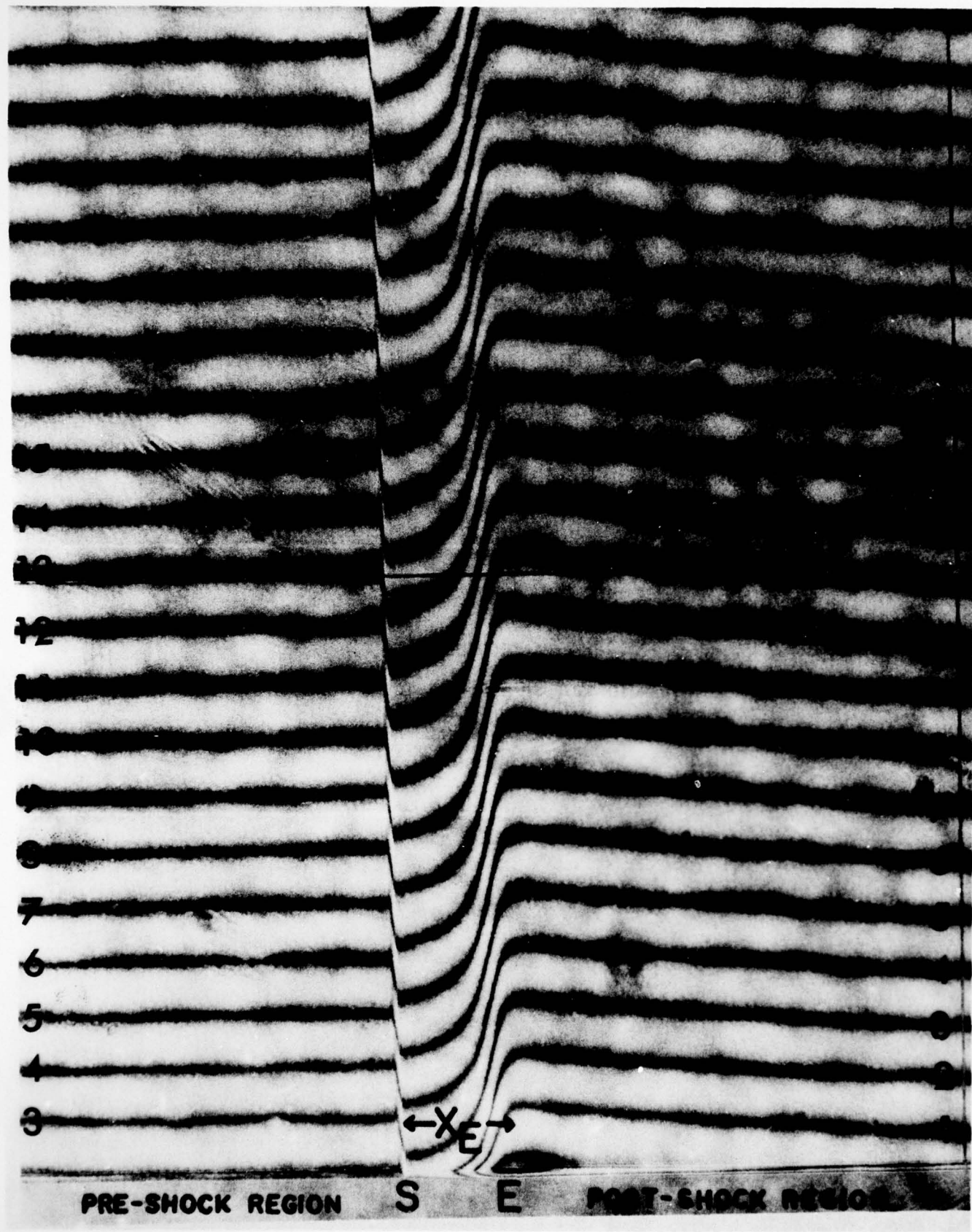


FIGURE 5  
POLAROID SHOT OF NaCl CRYSTAL COATING  
ON THE TEST-SECTION LOWER WALL PRIOR TO FIRING



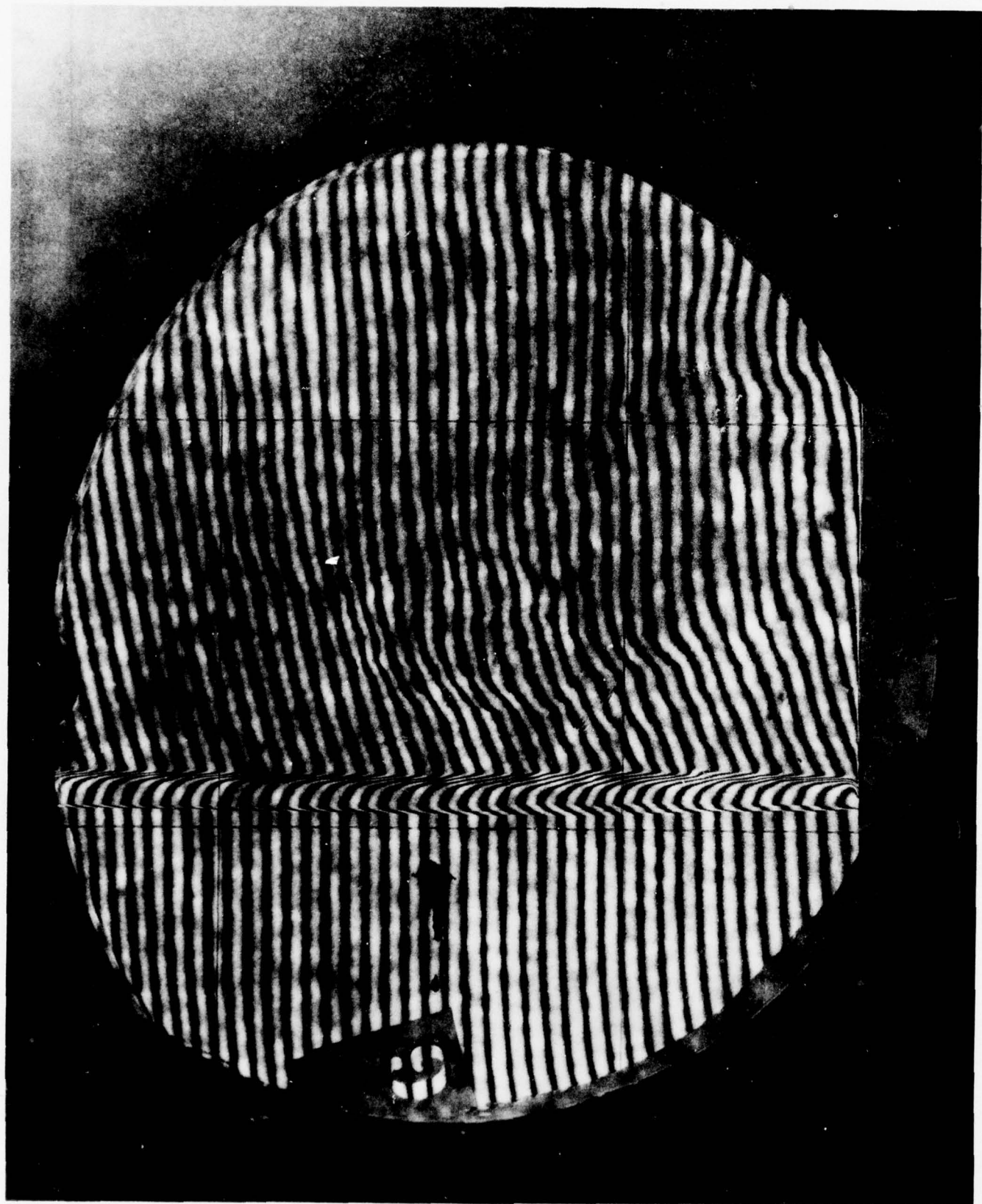


FIGURE 7 a) FLOW-INTERFEROGRAM TO BE DIGITIZED SHOWING LOCATIONS OF CROSS-HAIRS

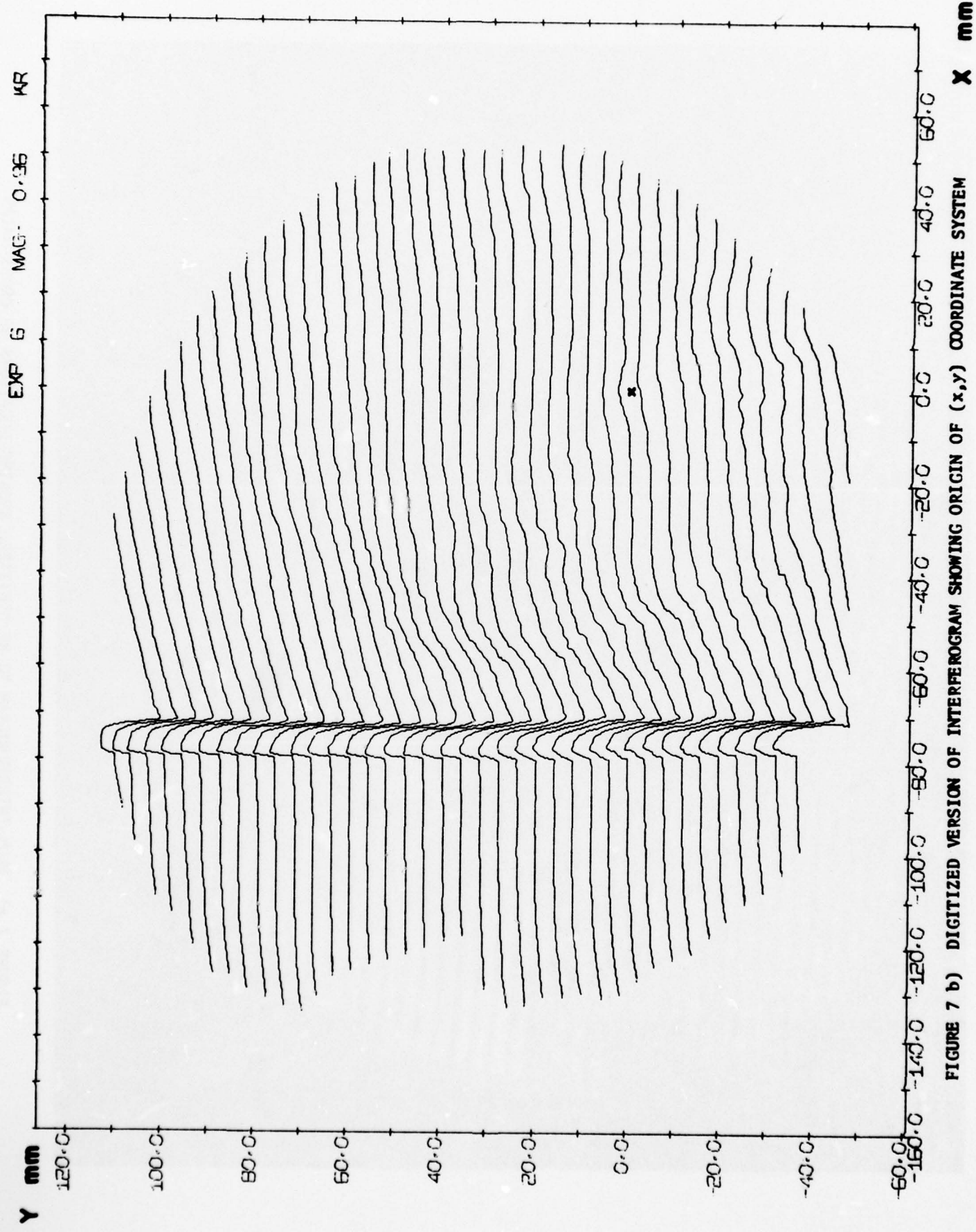


FIGURE 7 b) DIGITIZED VERSION OF INTERFEROGRAM SHOWING ORIGIN OF (x,y) COORDINATE SYSTEM

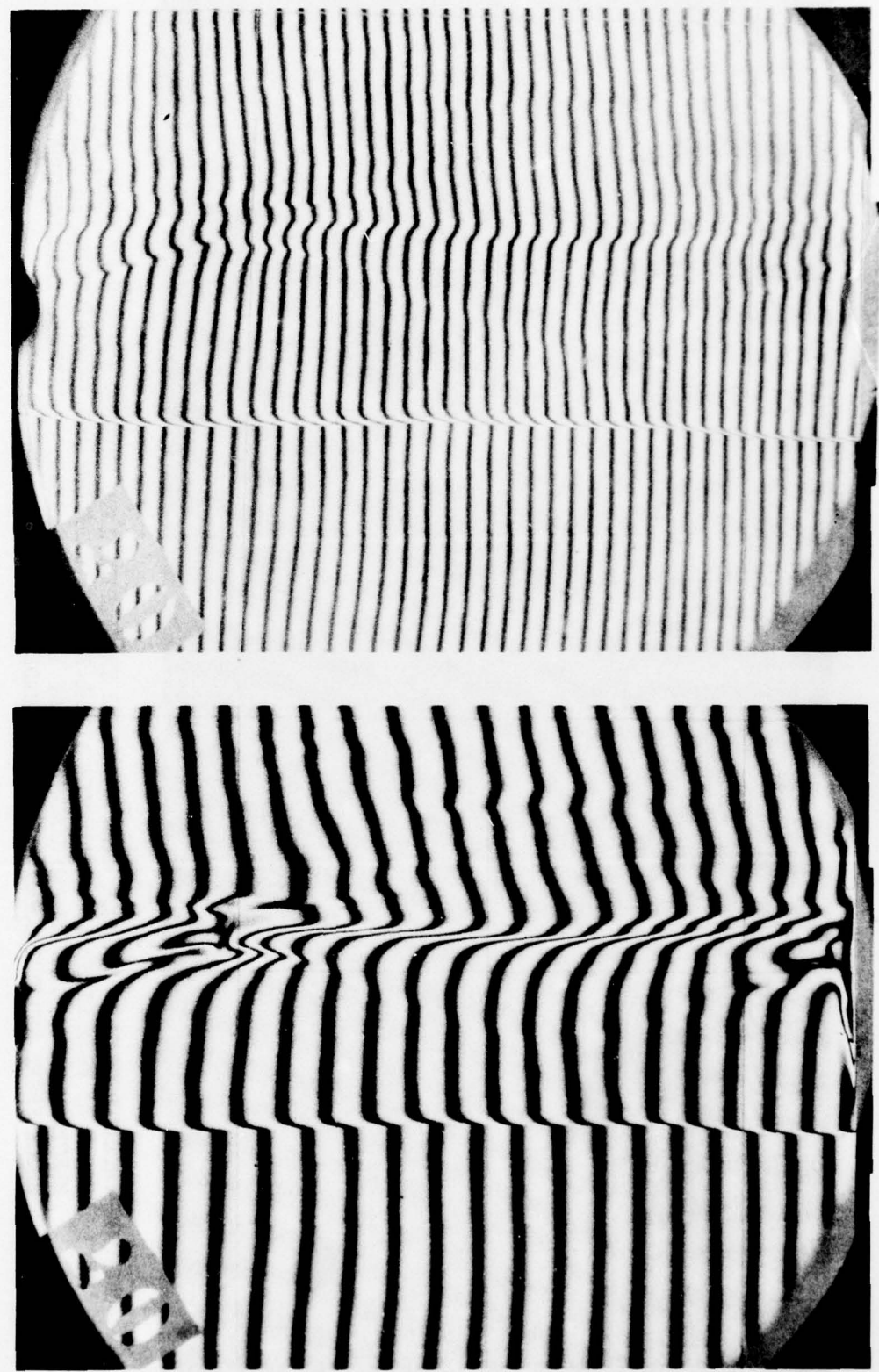


FIG. 8 SIMULTANEOUS INTERFEROGRAMS OF A SHOCK WAVE  $M_S = 14.7$  TRAVELLING INTO ARGON ( $P_1 = 4.08$  TORR,  $T_1 = 298.0$  K) FROM RIGHT TO LEFT. SINUSOIDAL TYPE SHOCK FRONT AND INSTABILITIES IN THE ELECTRON CASCADE FRONT AND DOWNSTREAM OF IT ARE ALSO SEEN. S DENOTES TRANSLATIONAL SHOCK FRONT AND E DENOTES ELECTRON CASCADE FRONT.

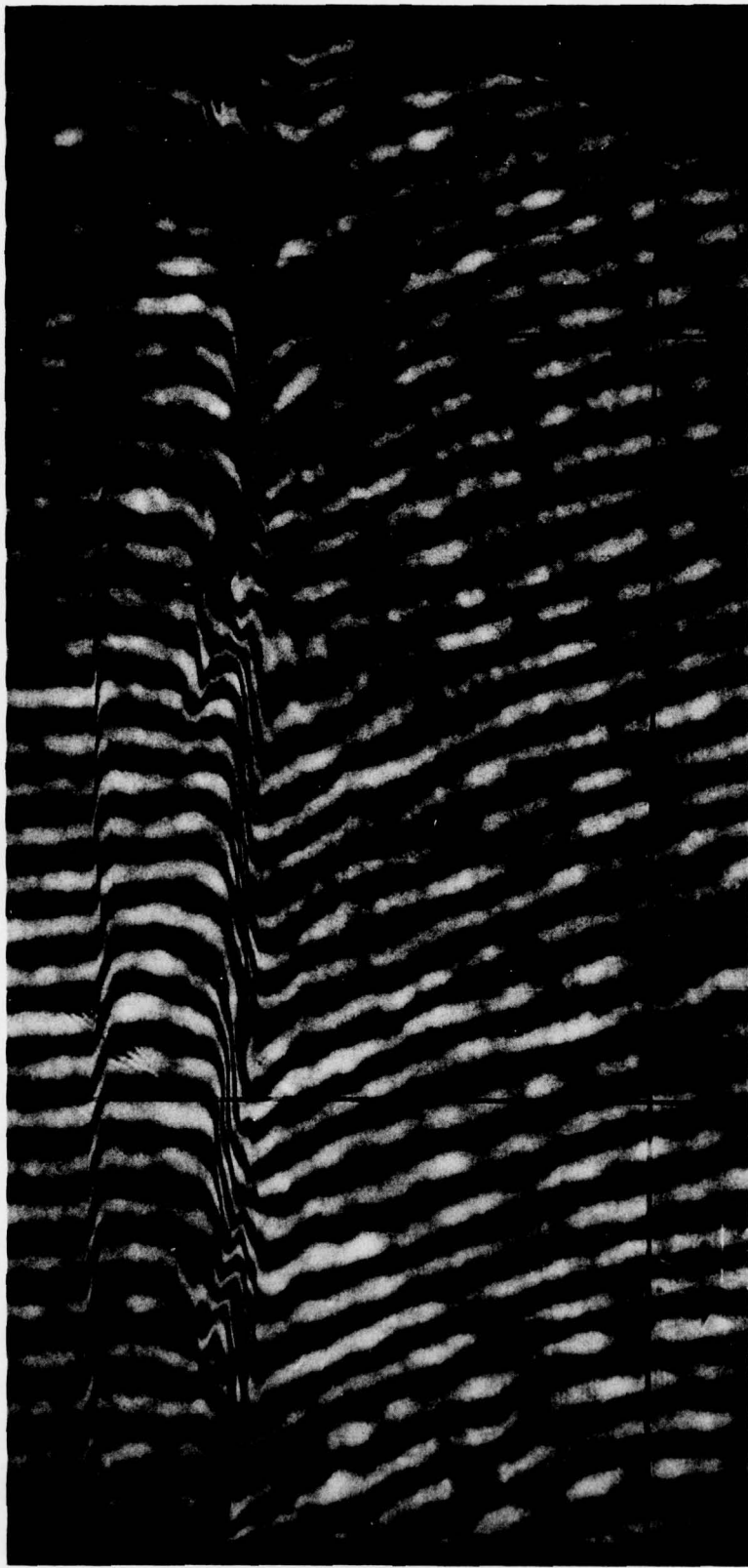


FIG. 9. INTERFERGRAM OF A SHOCK WAVE  $M_S = 15.2$  TRAVELLING INTO KRYPTON ( $P_1 = 5.07$  TORR,  $T_1 = 295.4$  K) FROM RIGHT TO LEFT. SINUSOIDAL TYPE SHOCK FRONT AND INSTABILITIES IN THE ELECTRON CASCADE FRONT AND DOWNSTREAM OF IT ARE ALSO SEEN. S DENOTES TRANSLATIONAL SHOCK FRONT AND E DENOTES ELECTRON CASCADE FRONT.

FIG. 10 (a) VARIATIONS OF HEAVY PARTICLE TEMPERATURE  $T_a$ , ELECTRON TEMPERATURE  $T_e$  AND HEAVY PARTICLE VELOCITY  $u$  WITH DISTANCE  $x$  BEHIND A SHOCK FRONT (FOR KRYPTON TEST GAS, CASE 7).  $M_s = 15.1$ ,  $P_1 = 5.15$  TORR,  $T_1 = 296.2$  K AND  $u_1 = 3.33 \times 10^5$  CM/SEC.

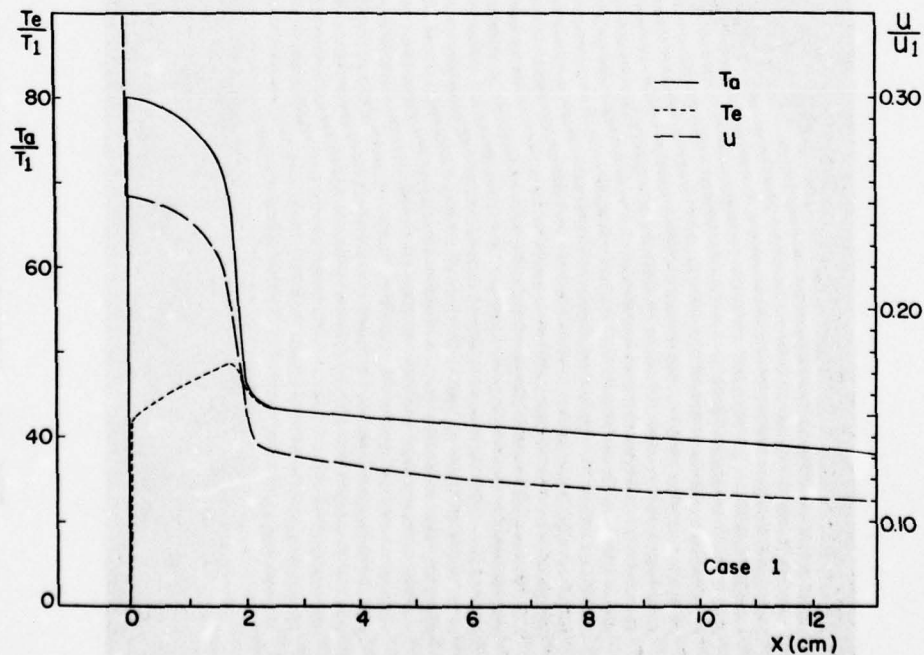
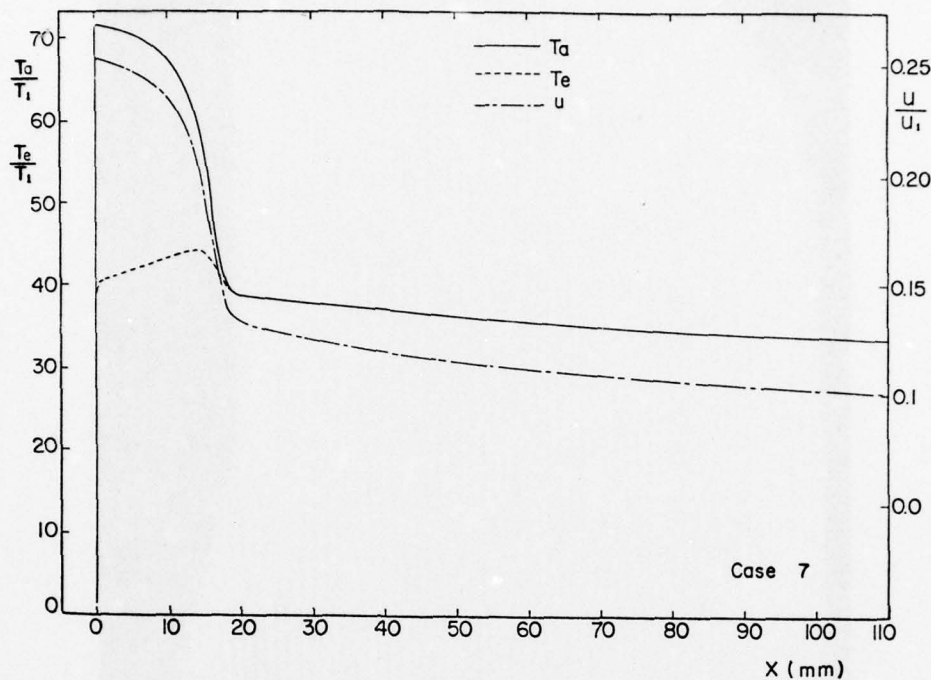


FIG. 10 (b) VARIATIONS OF HEAVY PARTICLE TEMPERATURE  $T_a$ , ELECTRON TEMPERATURE  $T_e$  AND HEAVY PARTICLE VELOCITY  $u$  WITH DISTANCE  $x$  BEHIND A SHOCK FRONT (FOR ARGON TEST GAS, CASE 1).  $M_s = 15.9$ ,  $P_1 = 5.14$  TORR,  $T_1 = 293.6$  K AND  $u_1 = 5.08 \times 10^5$  CM/SEC.

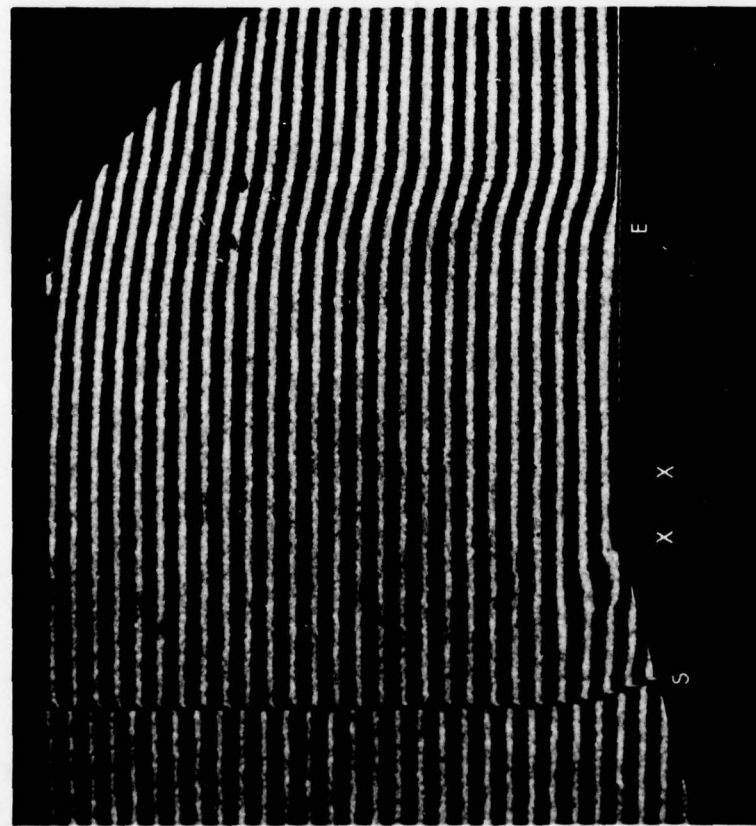
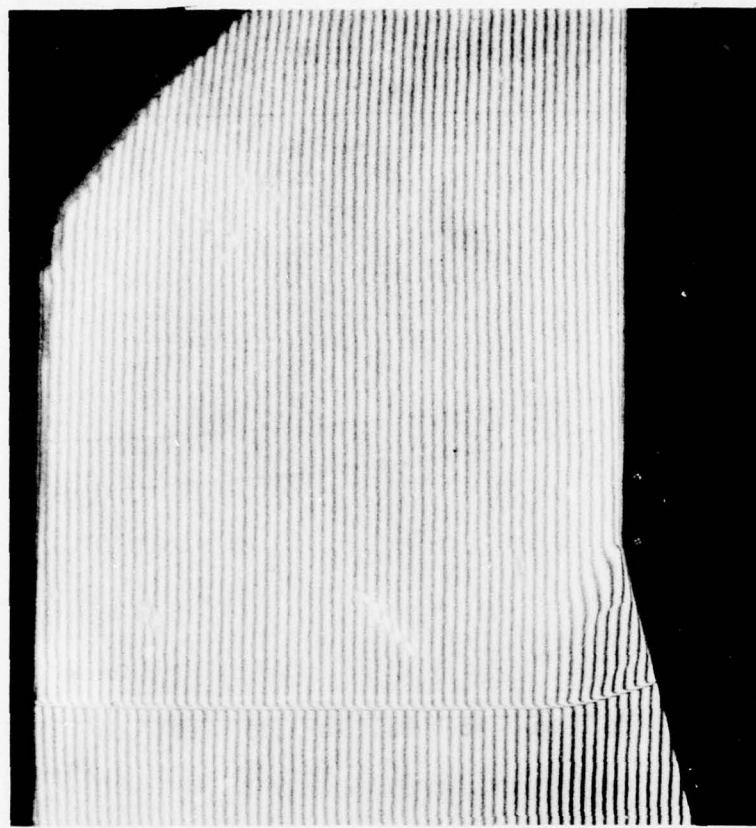


FIG. 11 SIMULTANEOUS INTERFEROGRAMS OF A SHOCK WAVE  $M_s = 13.0$  TRAVELLING FROM RIGHT TO LEFT AROUND A 15-DEGREE SHARP CORNER IN IONIZING ARGON ( $P_1 = 5.01$  TORR AND  $T_1 = 296.6$  K). S DENOTES TRANSLATIONAL SHOCK FRONT AND E DENOTES ELECTRON CASCADE FRONT.

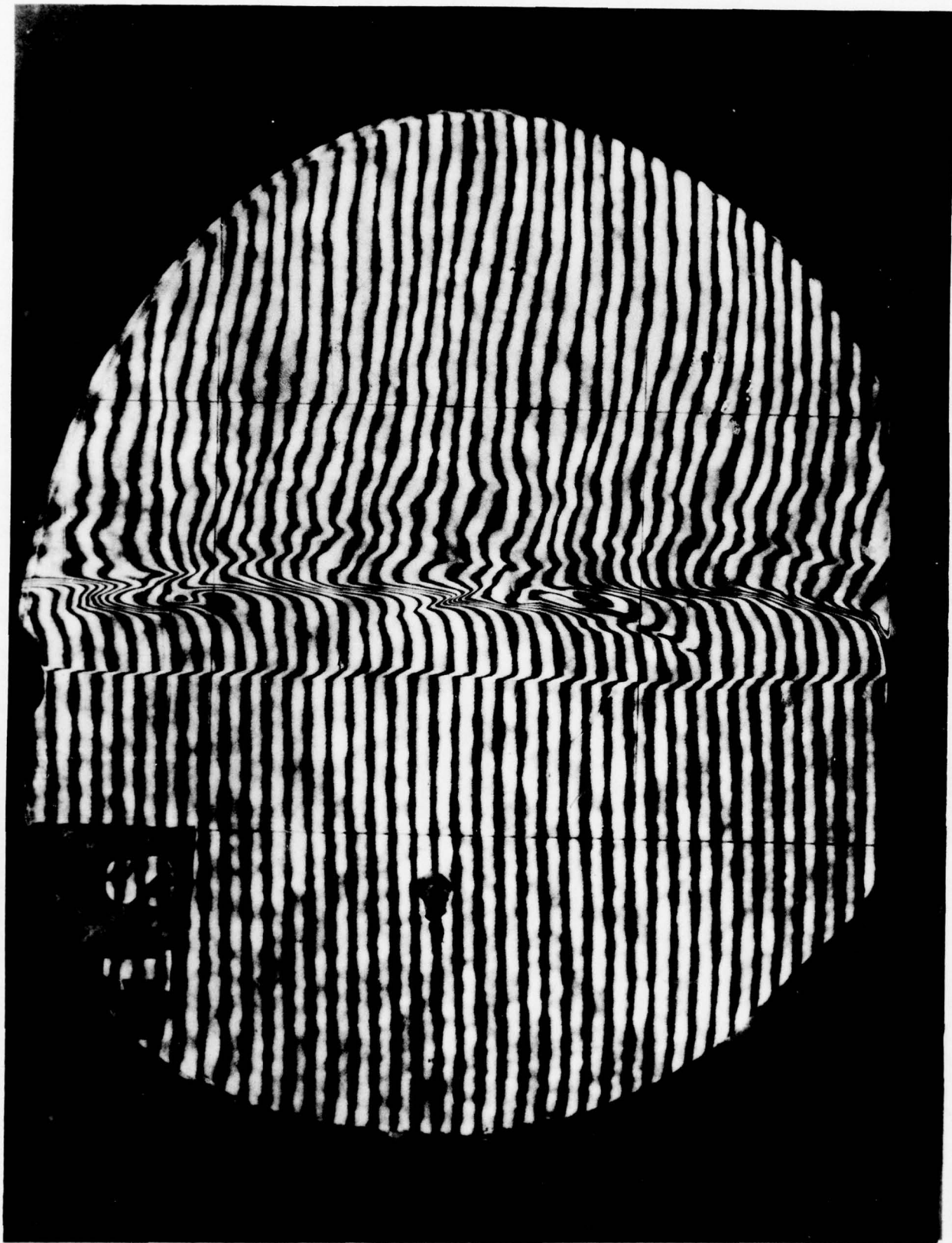


FIG. 12 INTERFEROGRAM OF A STRONG SHOCK WAVE  $M_s = 16.1$  TRAVELLING FROM RIGHT TO LEFT INTO ARGON TEST GAS ( $P_1 = 5.15$  TORR AND  $T_1 = 295.9$  K).

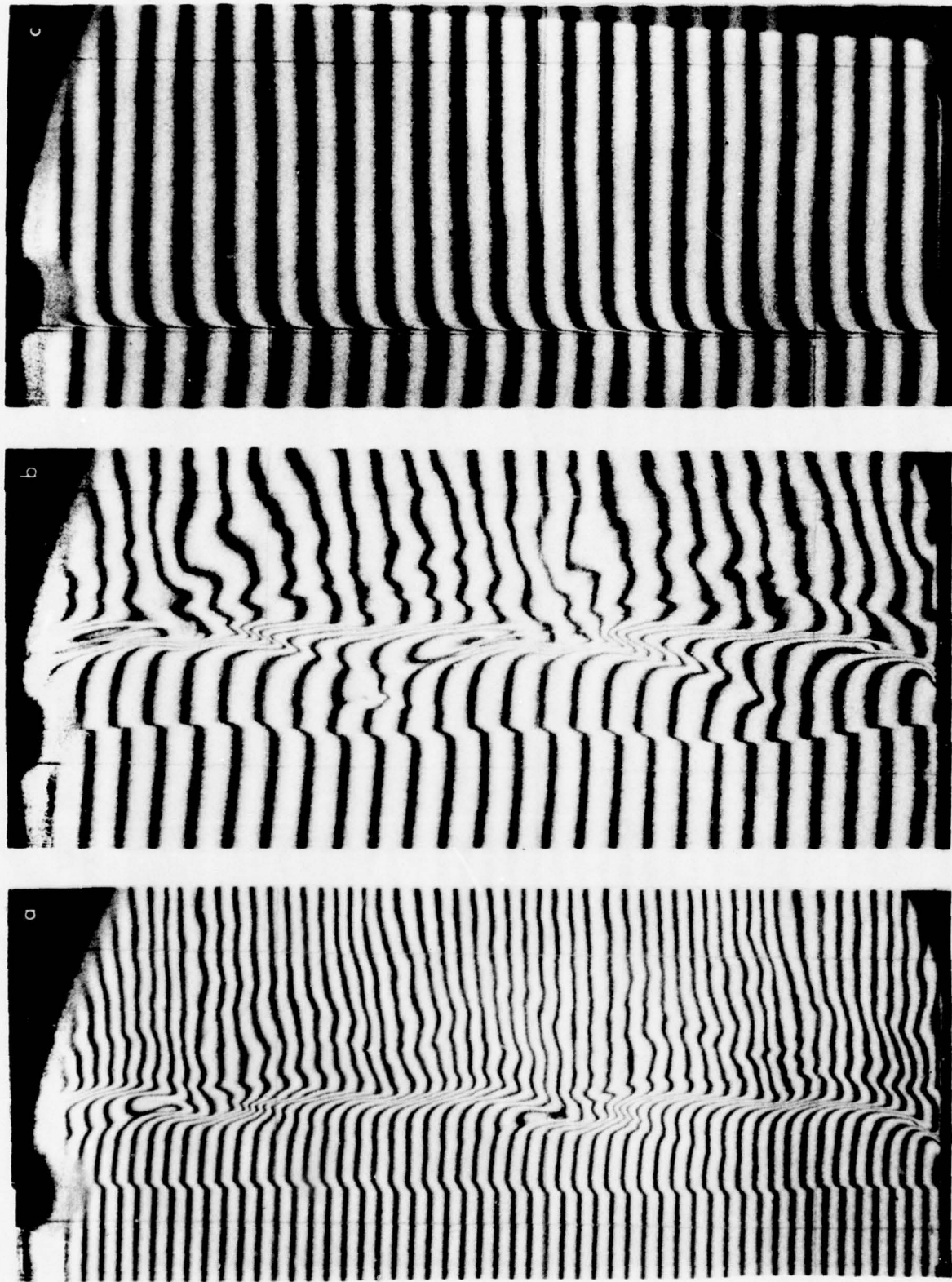


FIG. 13 INTERFEROGRAMS OF SHOCK WAVE STRUCTURE AND STABILITY.

- (a) 0.46% (BY PRESSURE) OF O<sub>2</sub> IMPURITY IN ARGON TEST GAS.  $M_s = 17.1$ ,  $P_1 = 2.85$  TORR AND  $T_1 = 295.7$  K. UNSTABLE SHOCK.
- (b) 1.08% (BY PRESSURE) OF He IMPURITY IN ARGON TEST GAS.  $M_s = 17.2$ ,  $P_1 = 2.87$  TORR AND  $T_1 = 295.6$  K. UNSTABLE SHOCK.
- (c) PURE N<sub>2</sub> TEST GAS.  $M_s = 16.6$ ,  $P_1 = 2.26$  TORR AND  $T_1 = 295.6$  K.

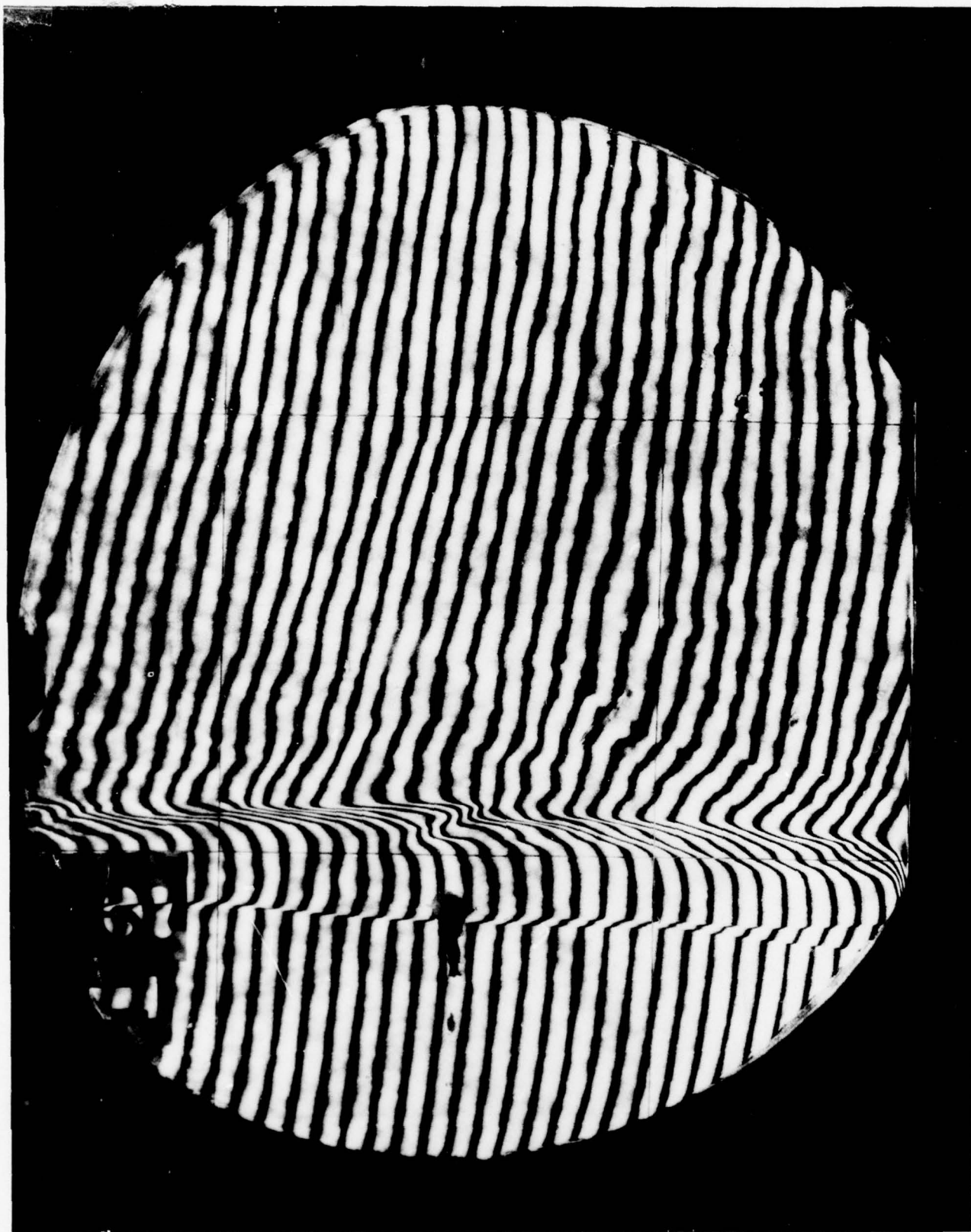


FIG. 14 INTERFEROGRAM OF A SHOCK WAVE  $M_s = 15.9$  TRAVELLING FROM RIGHT TO LEFT INTO ARGON,  $P_1 = 5.14$  TORR AND  $T_1 = 293.6$  K (CASE 1).

FIG. 15 VARIATIONS OF NONDIMENSIONALIZED ELECTRON NUMBER DENSITY ( $n_e/n_{e,E}$ ) AND DENSITY ( $\rho/\rho_E$ ) WITH DISTANCE  $x$  FOR CASE 1.

---  $M_s = 16.2$  AND  $S_{Ar-Ar}^* = 0.9 \times 10^{-19} \text{ cm}^2/\text{eV}$   
 —  $M_s = 15.9$  AND  $S_{Ar-Ar}^* = 1.0 \times 10^{-19} \text{ cm}^2/\text{eV}$   
 - - -  $M_s = 15.6$  AND  $S_{Ar-Ar}^* = 1.1 \times 10^{-19} \text{ cm}^2/\text{eV}$   
 $P_1 = 5.14 \text{ TORR AND } T_1 = 293.6 \text{ K.}$

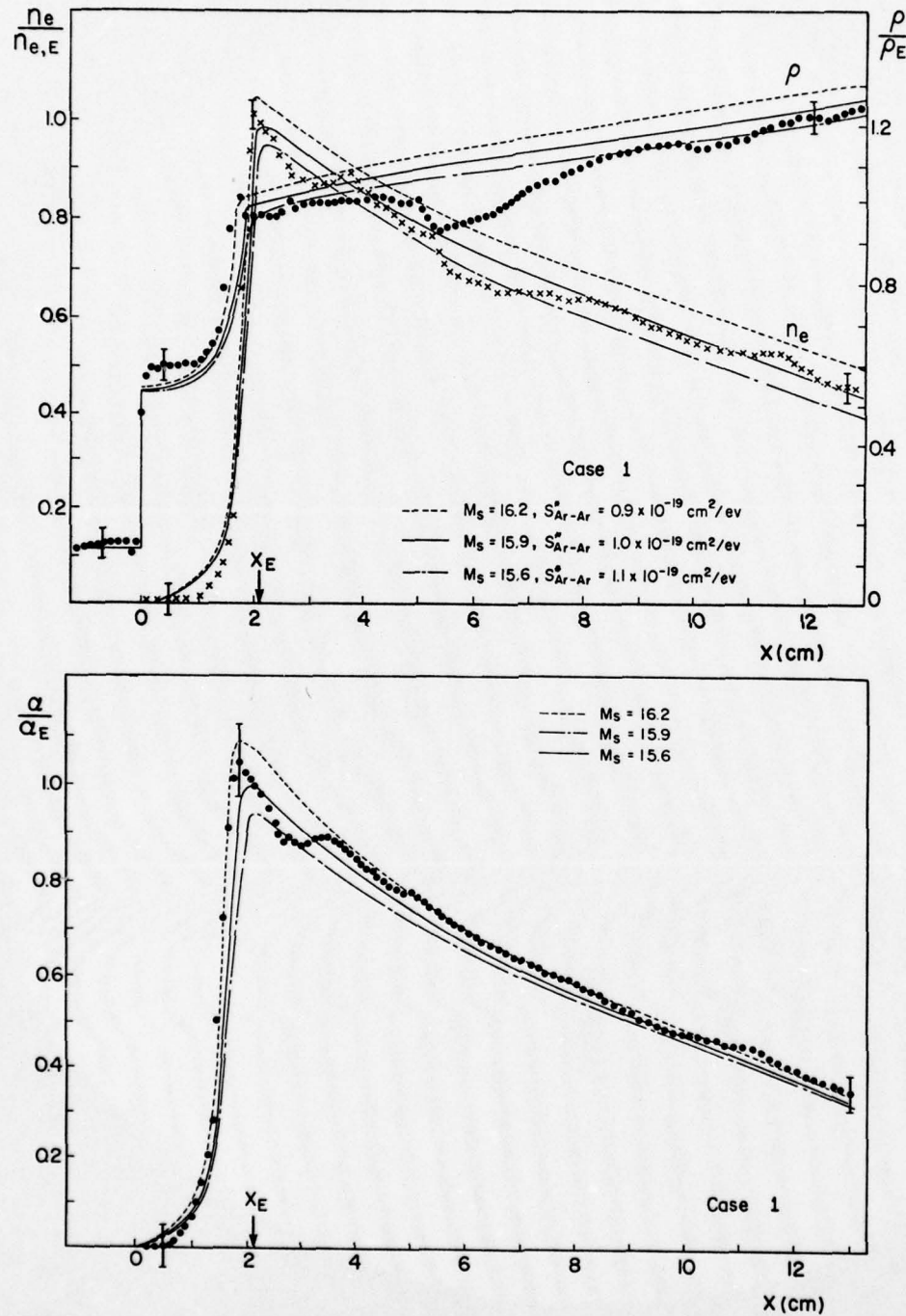


FIG. 16 VARIATION OF NONDIMENSIONALIZED DEGREE OF IONIZATION ( $\alpha/\alpha_E$ ) WITH DISTANCE  $x$  FOR CASE 1.

---  $M_s = 16.2$  AND  $S_{Ar-Ar}^* = 0.9 \times 10^{-19} \text{ cm}^2/\text{eV}$   
 —  $M_s = 15.9$  AND  $S_{Ar-Ar}^* = 1.0 \times 10^{-19} \text{ cm}^2/\text{eV}$   
 - - -  $M_s = 15.6$  AND  $S_{Ar-Ar}^* = 1.1 \times 10^{-19} \text{ cm}^2/\text{eV}$   
 $P_1 = 5.14 \text{ TORR AND } T_1 = 293.6 \text{ K.}$

FIG. 17 VARIATIONS OF NONDIMENSIONALIZED ELECTRON NUMBER DENSITY ( $n_e/n_{e,E}$ ) AND DENSITY ( $\rho/\rho_E$ ) WITH DISTANCE  $x$  FOR CASE 2.

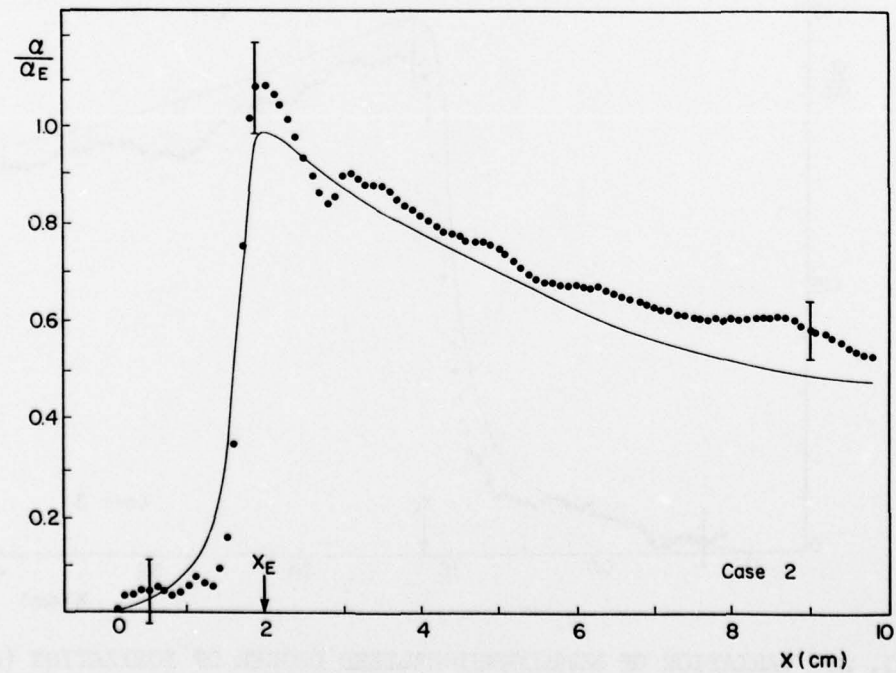
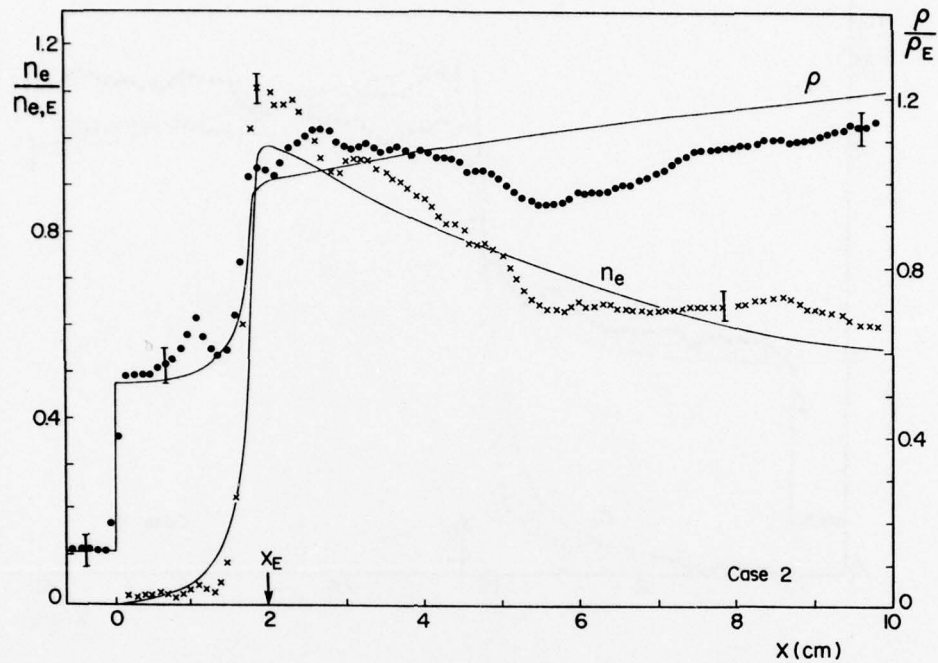


FIG. 18 VARIATION OF NONDIMENSIONALIZED DEGREE OF IONIZATION ( $\alpha/\alpha_E$ ) WITH DISTANCE  $x$  FOR CASE 2.

FIG. 19 VARIATIONS OF NONDIMENSIONALIZED ELECTRON NUMBER DENSITY ( $n_e/n_{e,E}$ ) AND DENSITY ( $\rho/\rho_E$ ) WITH DISTANCE  $x$  FOR CASE 3.

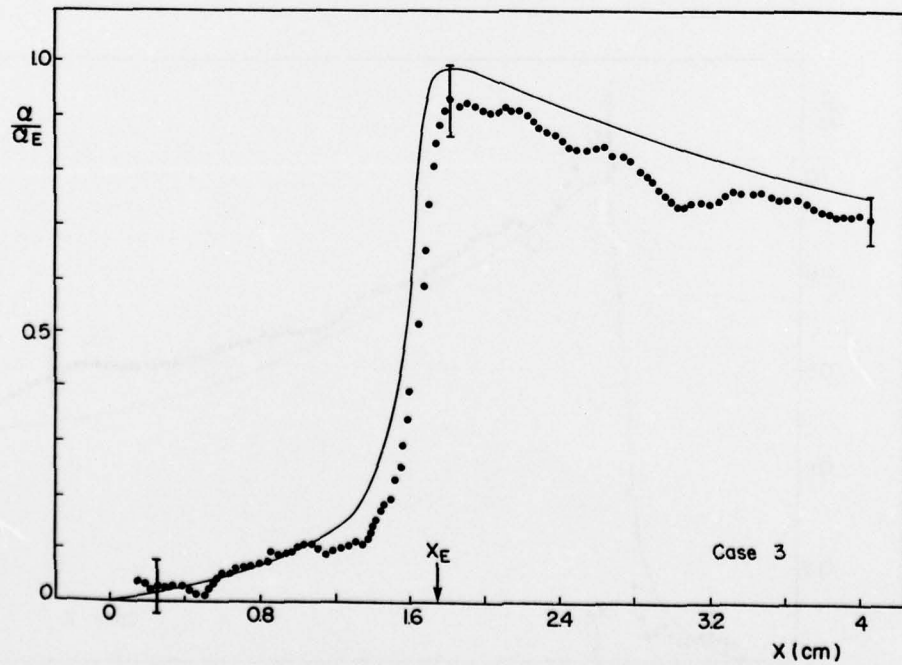
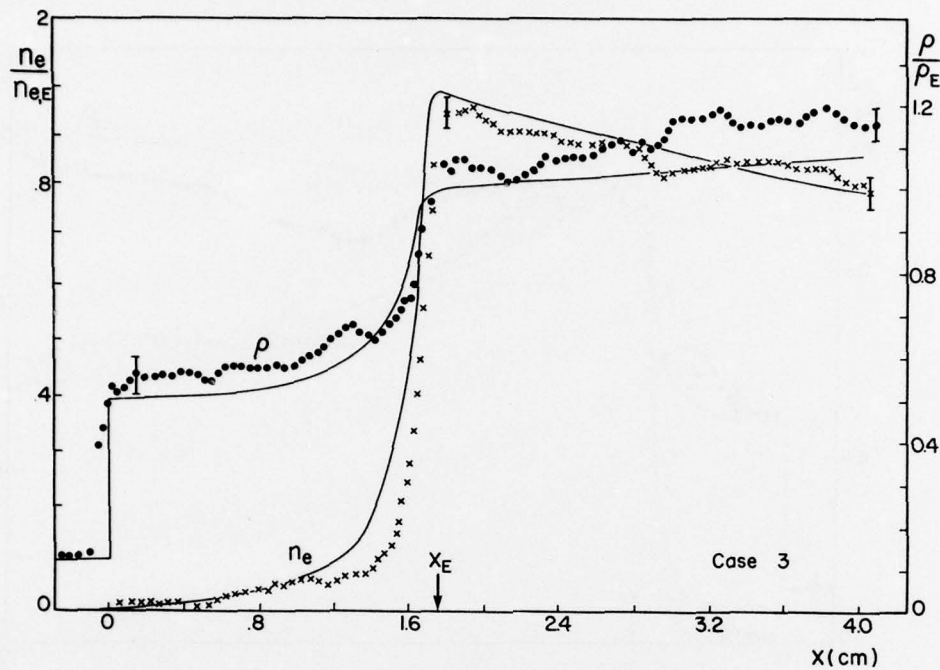


FIG. 20 VARIATION OF NONDIMENSIONALIZED DEGREE OF IONIZATION ( $\alpha/\alpha_E$ ) WITH DISTANCE  $x$  FOR CASE 3.

FIG. 21 VARIATIONS OF NONDIMENSIONALIZED ELECTRON NUMBER DENSITY ( $n_e/n_{e,E}$ ) AND DENSITY ( $\rho/\rho_E$ ) WITH DISTANCE  $x$  FOR CASE 4.

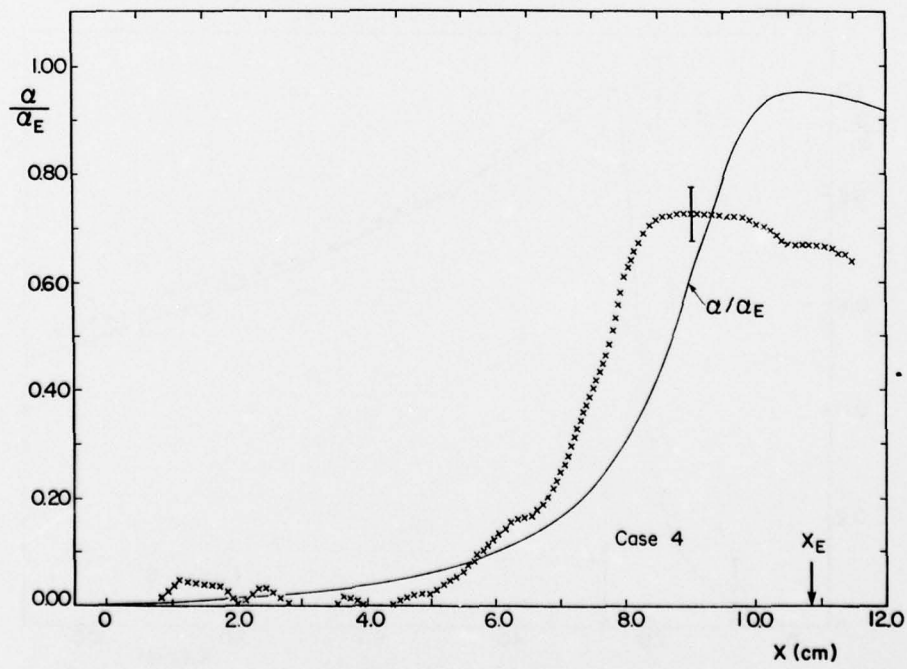
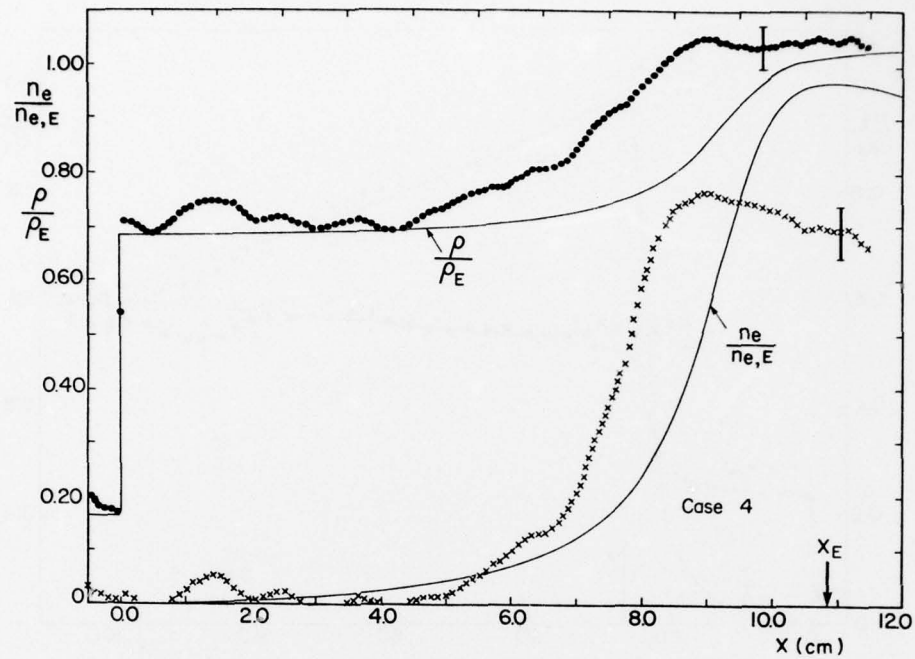


FIG. 22 VARIATION OF NONDIMENSIONALIZED DEGREE OF IONIZATION ( $\alpha/\alpha_E$ ) WITH DISTANCE  $x$  FOR CASE 4.

FIG. 23 VARIATIONS OF NONDIMENSIONALIZED ELECTRON NUMBER DENSITY ( $n_e/n_{e,E}$ ) AND DENSITY ( $\rho/\rho_E$ ) WITH DISTANCE  $x$  FOR CASE 5.

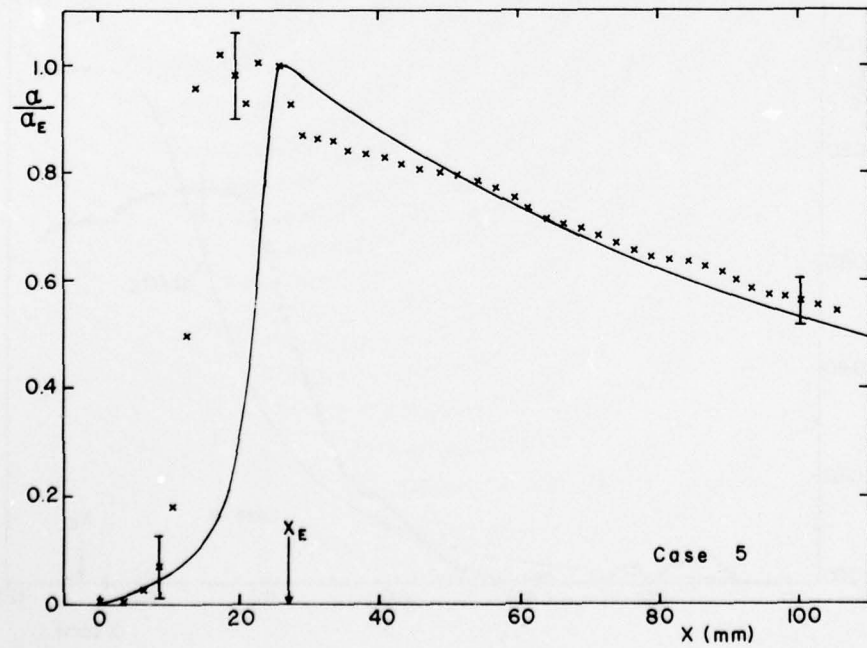
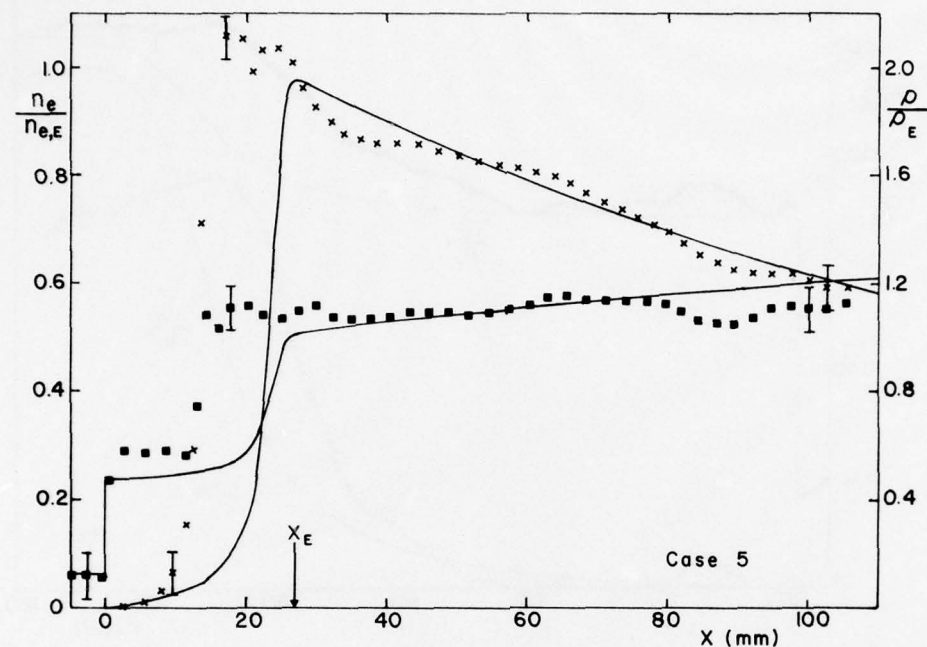


FIG. 24 VARIATION OF NONDIMENSIONALIZED DEGREE OF IONIZATION ( $\alpha/\alpha_E$ ) WITH DISTANCE  $x$  FOR CASE 5.

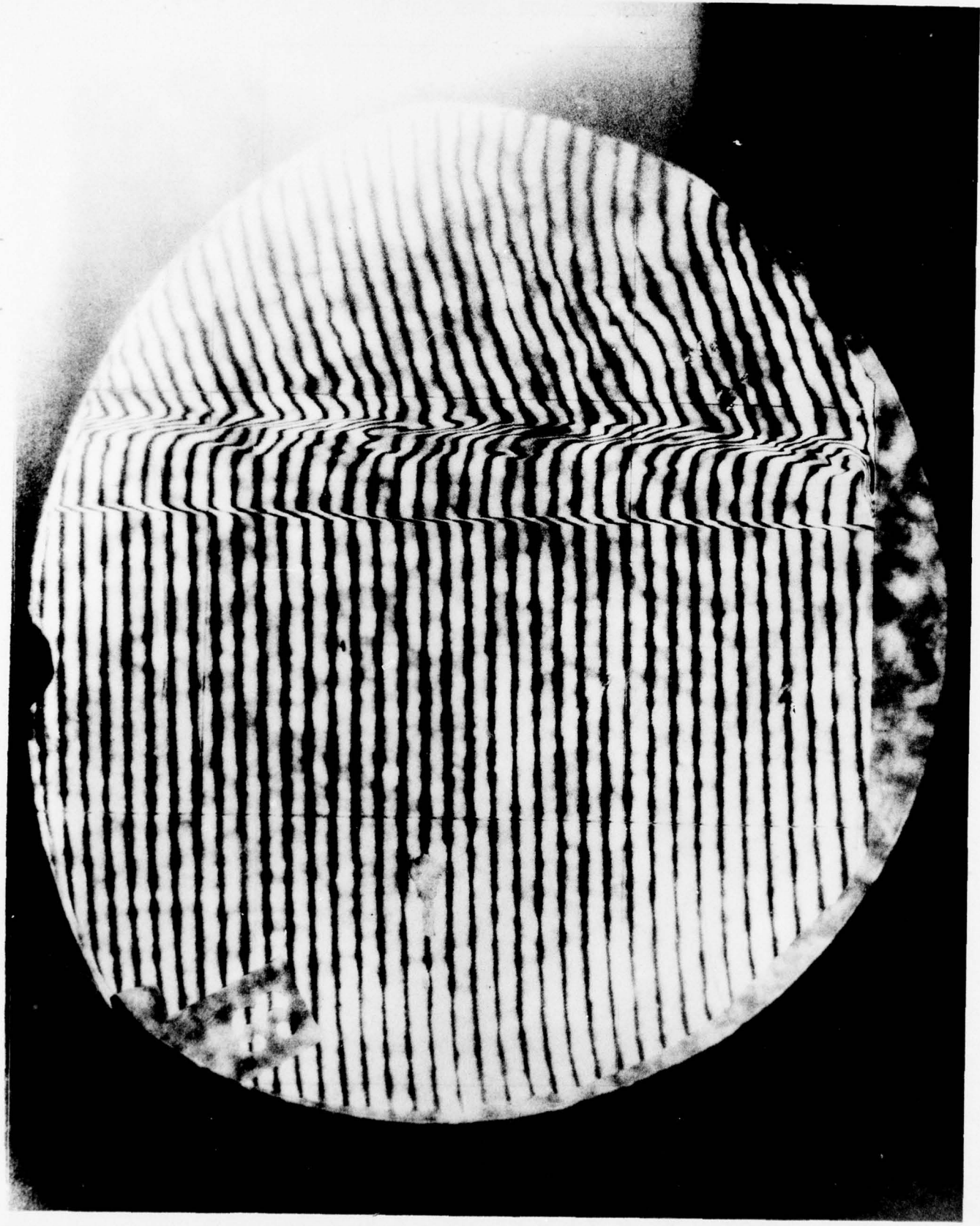


FIG. 25 INTERFEROGRAM OF A SHOCK WAVE  $M_S = 15.2$  TRAVELLING FROM RIGHT TO LEFT INTO KRYPTON,  $P_1 = 5.07$  TORR AND  $T_1 = 295.4$  K (CASE 6).

FIG. 26 VARIATIONS OF NONDIMENSIONALIZED ELECTRON NUMBER DENSITY ( $n_e/n_{e,E}$ ) AND DENSITY ( $\rho/\rho_E$ ) WITH DISTANCE  $x$  FOR CASE 6.

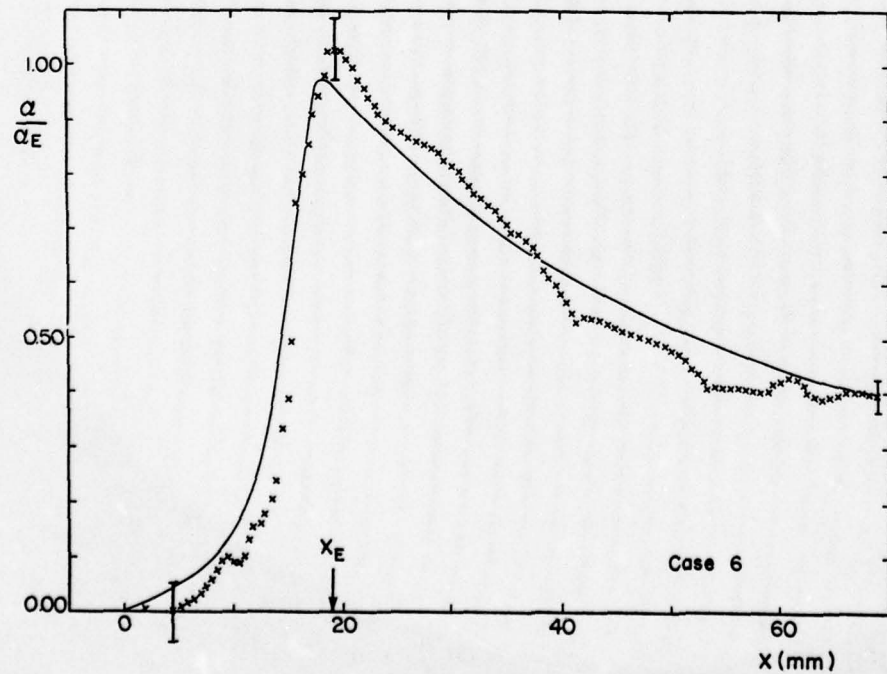
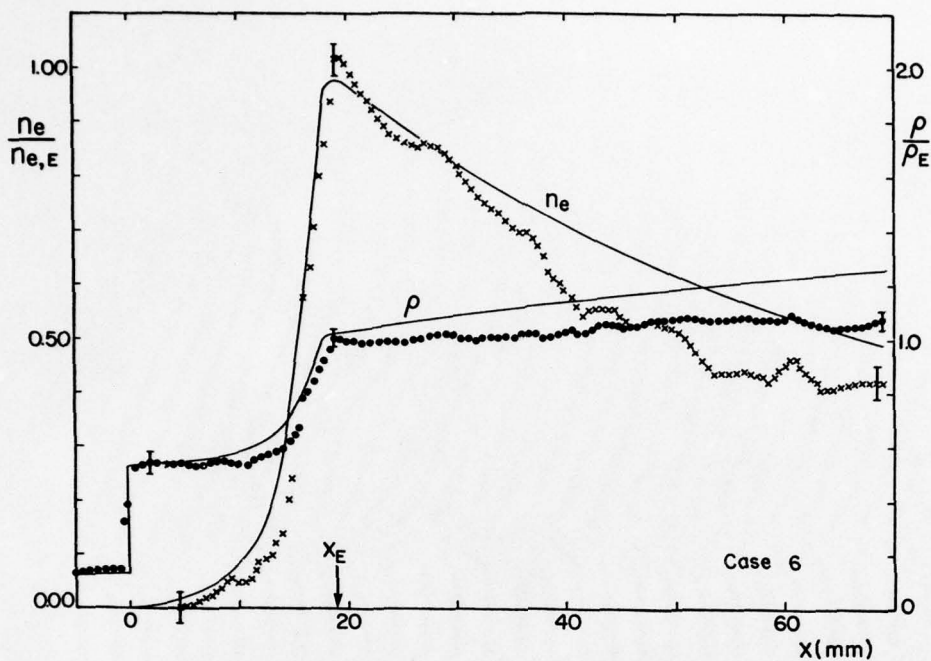


FIG. 27 VARIATION OF NONDIMENSIONALIZED DEGREE OF IONIZATION ( $\alpha/\alpha_E$ ) WITH DISTANCE  $x$  FOR CASE 6

FIG. 28 VARIATIONS OF NONDIMENSIONALIZED ELECTRON NUMBER DENSITY ( $n_e/n_{e,E}$ ) AND DENSITY ( $\rho/\rho_E$ ) WITH DISTANCE  $x$  FOR CASE 7.

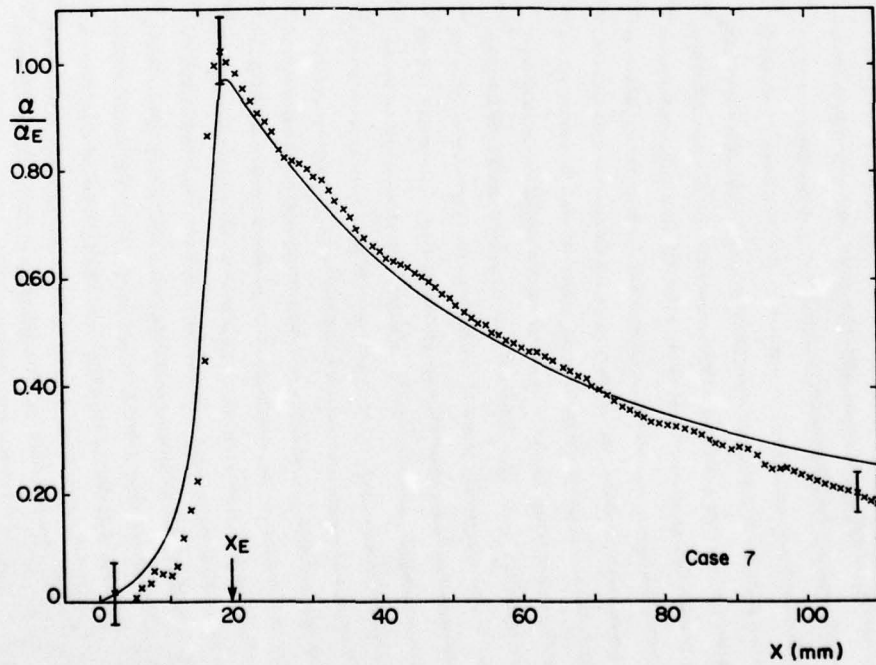
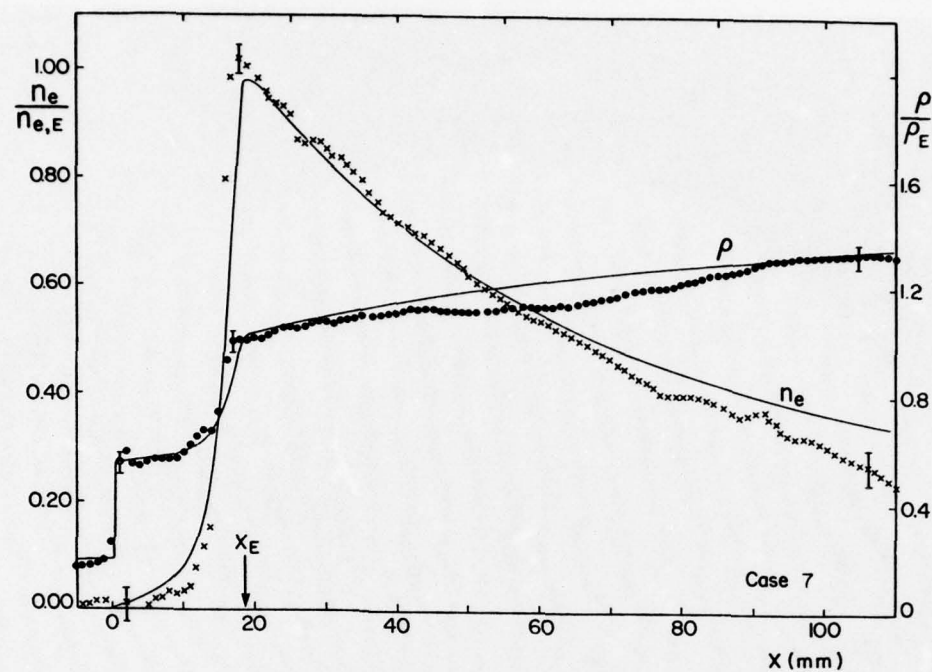


FIG. 29 VARIATION OF NONDIMENSIONALIZED DEGREE OF IONIZATION ( $\alpha/\alpha_E$ ) WITH DISTANCE  $x$  FOR CASE 7.

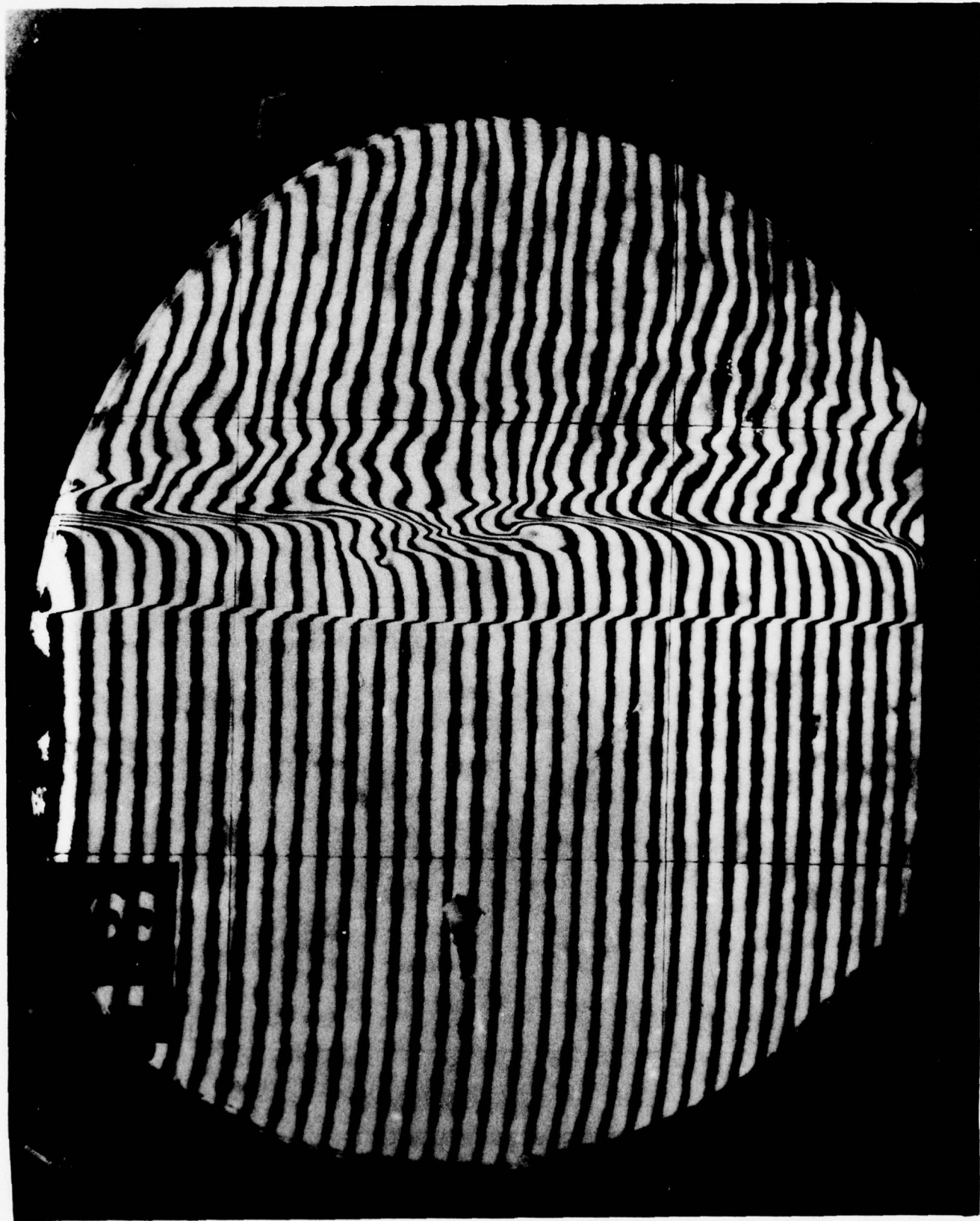


FIG. 30 INTERFEROGRAM OF A SHOCK WAVE  $M_s = 15.7$  TRAVELLING FROM RIGHT TO LEFT INTO NaCl CONTAMINATED ARGON,  $P_1 = 5.14$  TORR AND  $T_1 = 297.4$  K.

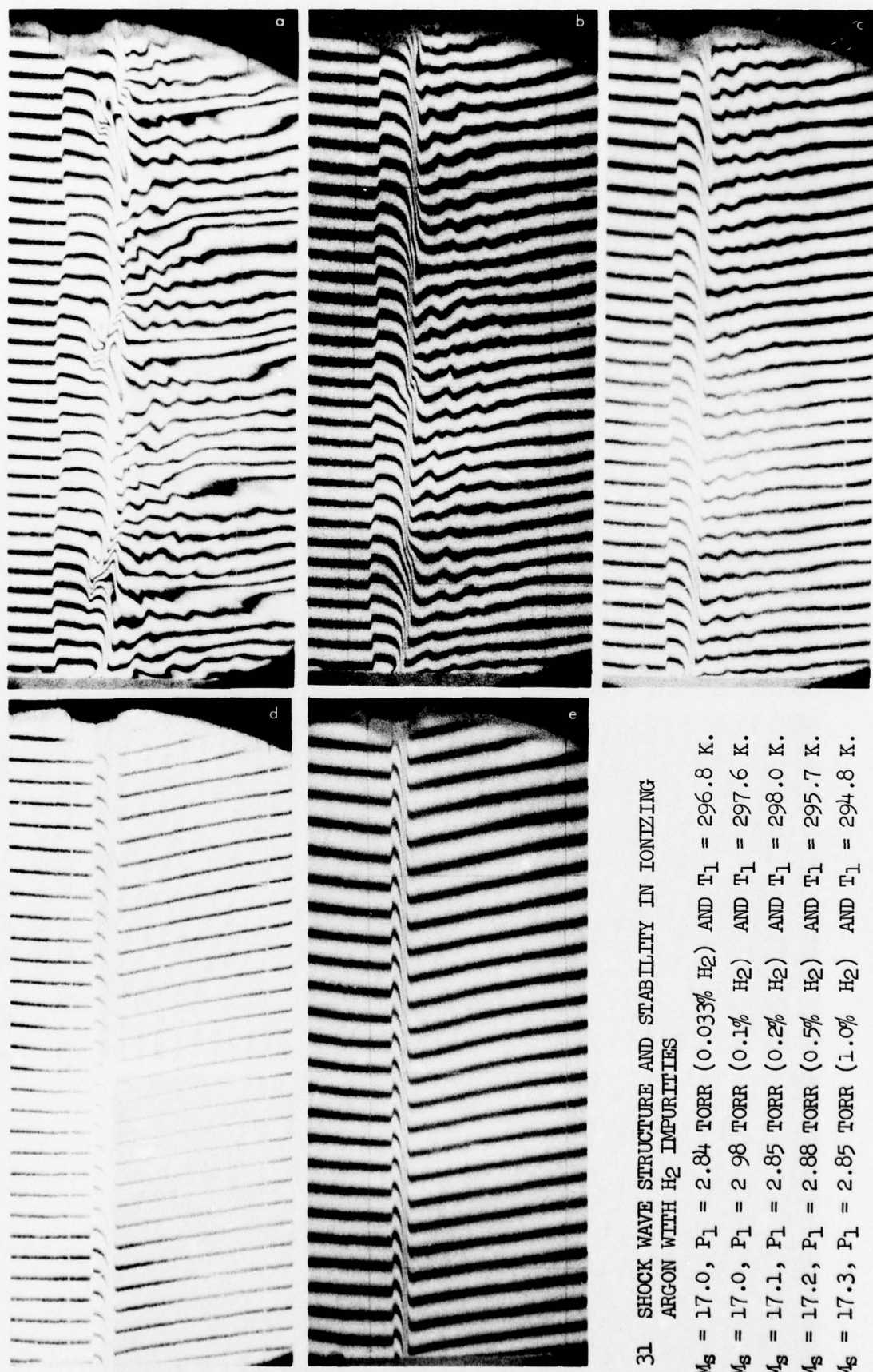


FIG. 31 SHOCK WAVE STRUCTURE AND STABILITY IN IONIZING ARGON WITH  $H_2$  IMPURITIES

- (a)  $M_S = 17.0$ ,  $P_1 = 2.84$  TORR (0.033%  $H_2$ ) AND  $T_1 = 296.8$  K.
- (b)  $M_S = 17.0$ ,  $P_1 = 2.98$  TORR (0.1%  $H_2$ ) AND  $T_1 = 297.6$  K.
- (c)  $M_S = 17.1$ ,  $P_1 = 2.85$  TORR (0.2%  $H_2$ ) AND  $T_1 = 298.0$  K.
- (d)  $M_S = 17.2$ ,  $P_1 = 2.88$  TORR (0.5%  $H_2$ ) AND  $T_1 = 295.7$  K.
- (e)  $M_S = 17.3$ ,  $P_1 = 2.85$  TORR (1.0%  $H_2$ ) AND  $T_1 = 294.8$  K.

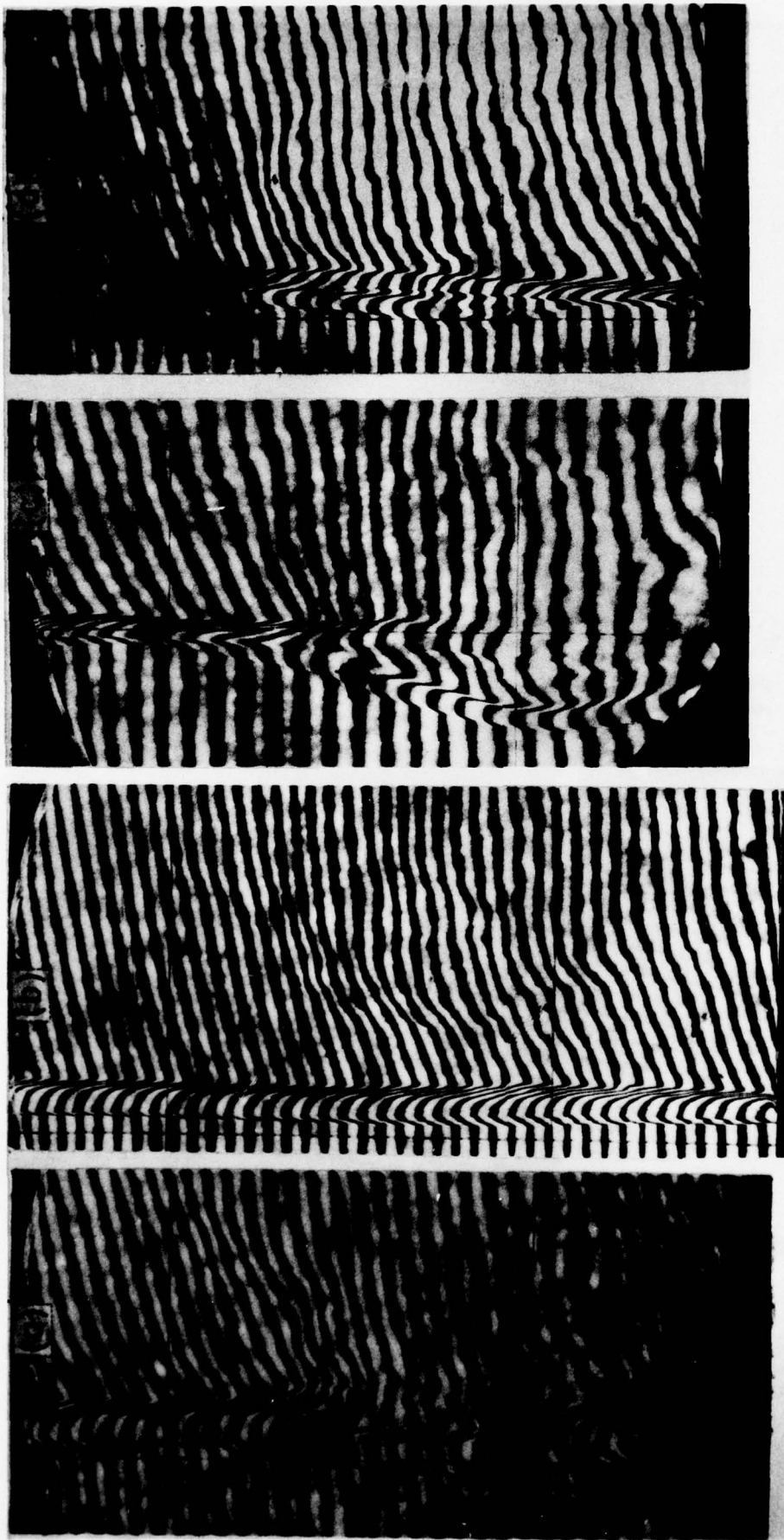


FIG. 32 SHOCK WAVE STRUCTURE AND STABILITY IN IONIZING KRYPTON WITH  $H_2$  IMPURITIES

- (a)  $M_s = 15.0$ ,  $P_1 = 5.15$  TORR (0.2%  $H_2$ ) AND  $T_1 = 298.3$  K.
- (b)  $M_s = 15.0$ ,  $P_1 = 5.21$  TORR (0.38%  $H_2$ ) AND  $T_1 = 295.4$  K.
- (c)  $M_s = 15.3$ ,  $P_1 = 5.19$  TORR (0.6%  $H_2$ ) AND  $T_1 = 296.6$  K.
- (d)  $M_s = 15.0$ ,  $P_1 = 5.13$  TORR (1.0%  $H_2$ ) AND  $T_1 = 297.7$  K.

FIG. 33 VARIATIONS OF NONDIMENSIONALIZED ELECTRON NUMBER DENSITY ( $n_e/n_{e,E}$ ) AND DENSITY ( $\rho/\rho_E$ ) WITH DISTANCE  $x$  FOR CASE 8.

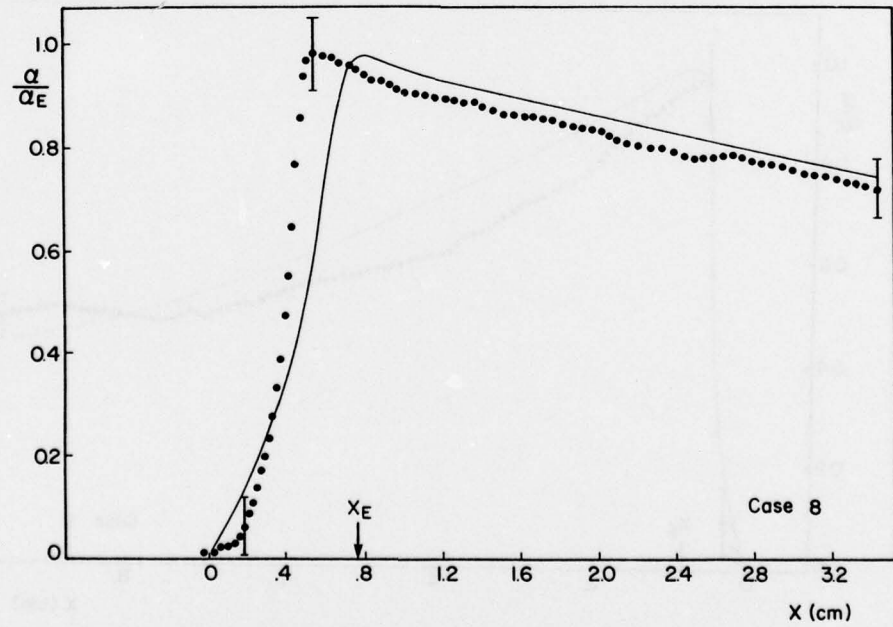
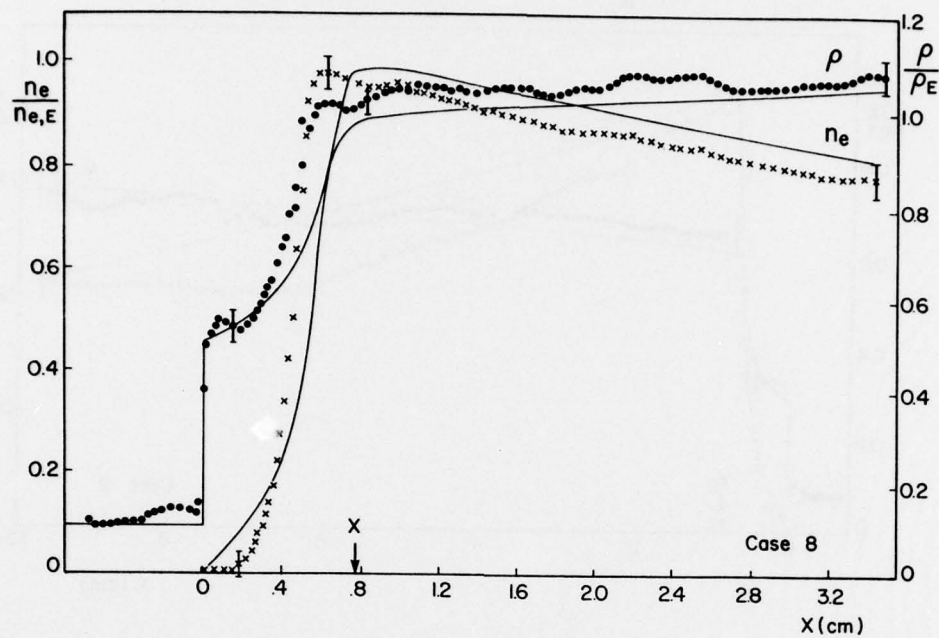


FIG. 34 VARIATION OF NONDIMENSIONALIZED DEGREE OF IONIZATION ( $\alpha/\alpha_E$ ) WITH DISTANCE  $x$  FOR CASE 8.

FIG. 35 VARIATIONS OF NONDIMENSIONALIZED ELECTRON NUMBER DENSITY ( $n_e/n_{e,E}$ ) AND DENSITY ( $\rho/\rho_E$ ) WITH DISTANCE  $x$  FOR CASE 9.

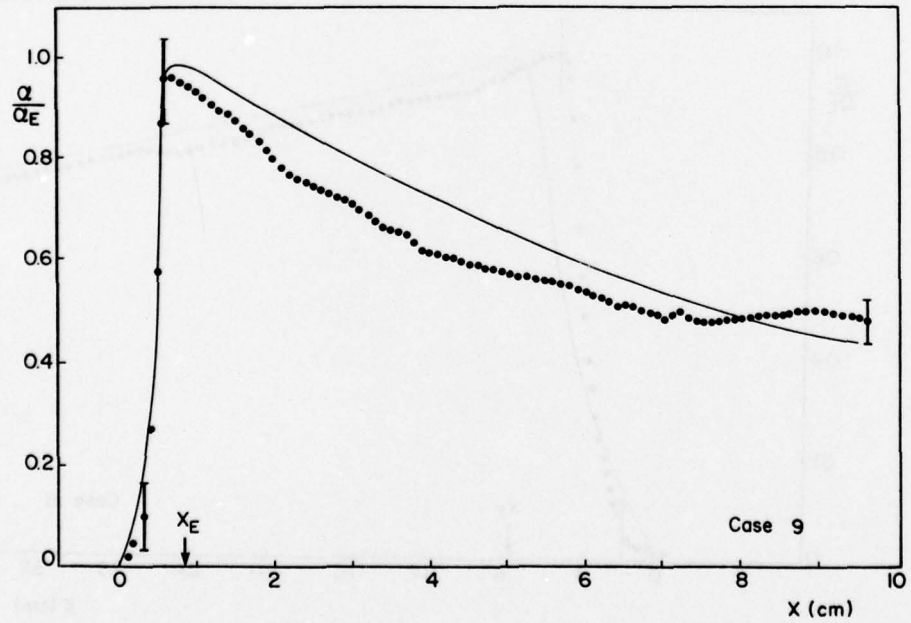
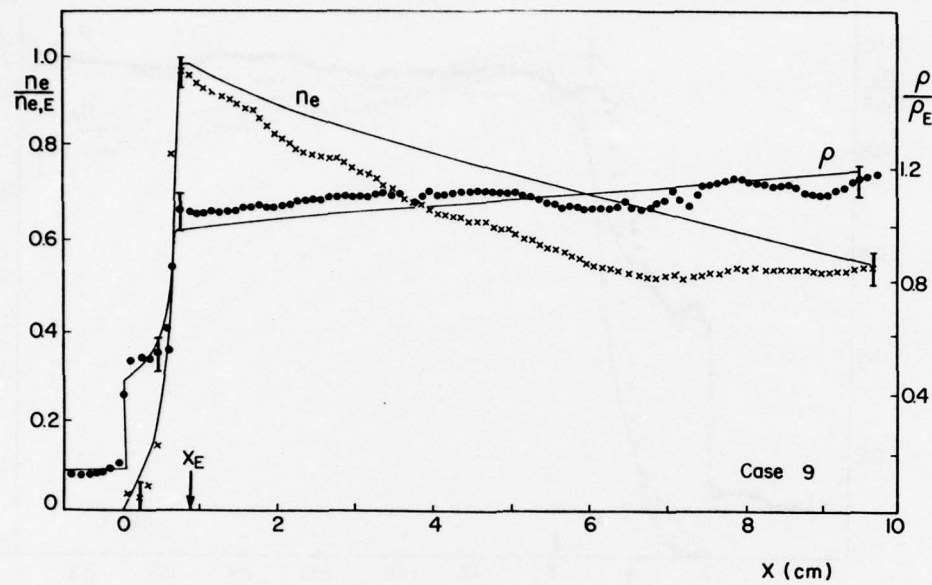


FIG. 36 VARIATION OF NONDIMENSIONALIZED DEGREE OF IONIZATION ( $\alpha/\alpha_E$ ) WITH DISTANCE  $x$  FOR CASE 9.

FIG. 37 VARIATIONS OF NONDIMENSIONALIZED ELECTRON NUMBER DENSITY ( $n_e/n_{e,E}$ ) AND DENSITY ( $\rho/\rho_E$ ) WITH DISTANCE  $x$  FOR CASE 10.

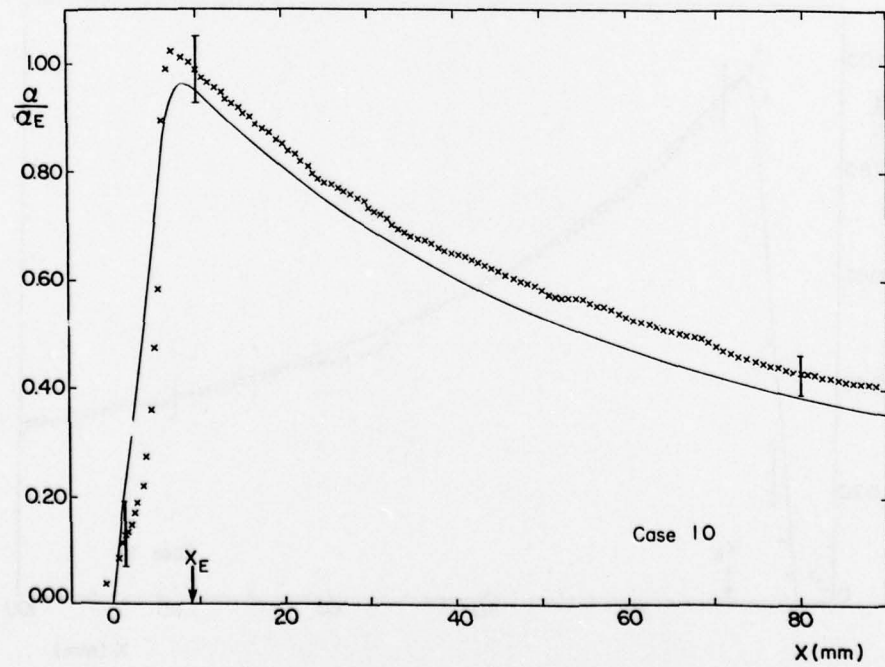
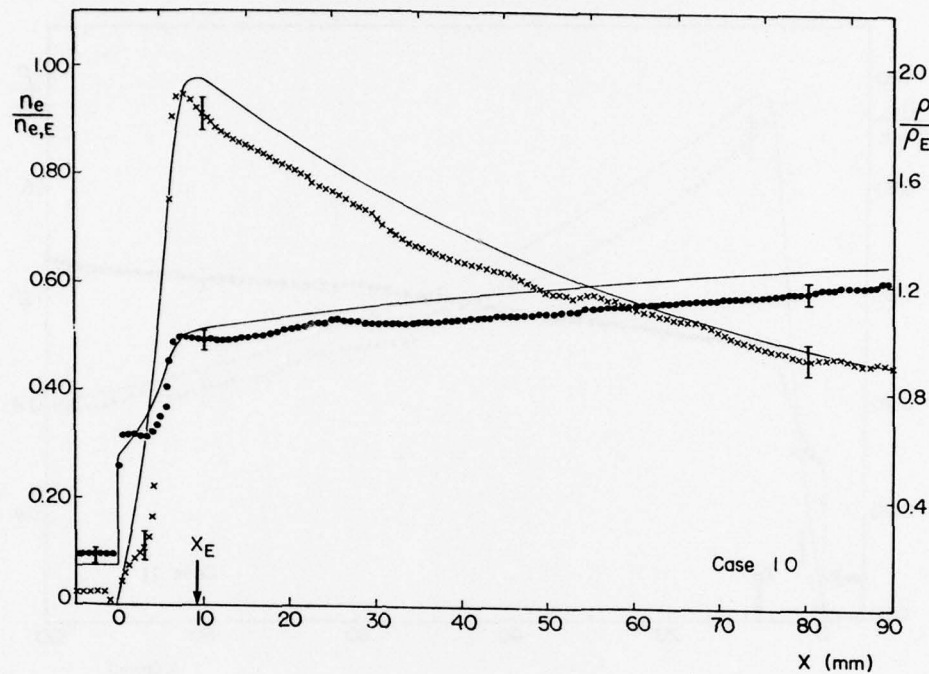


FIG. 38 VARIATION OF NONDIMENSIONALIZED DEGREE OF IONIZATION ( $\alpha/\alpha_E$ ) WITH DISTANCE  $x$  FOR CASE 10.

FIG. 39 VARIATIONS OF NONDIMENSIONALIZED ELECTRON NUMBER DENSITY ( $n_e/n_{e,E}$ ) AND DENSITY ( $\rho/\rho_E$ ) WITH DISTANCE  $x$  FOR CASE II.

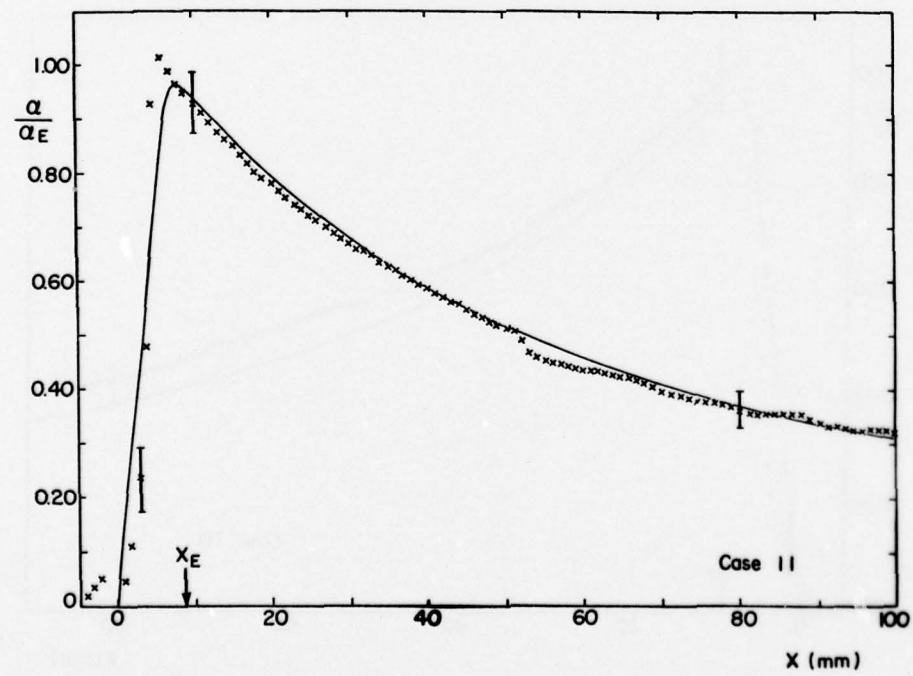
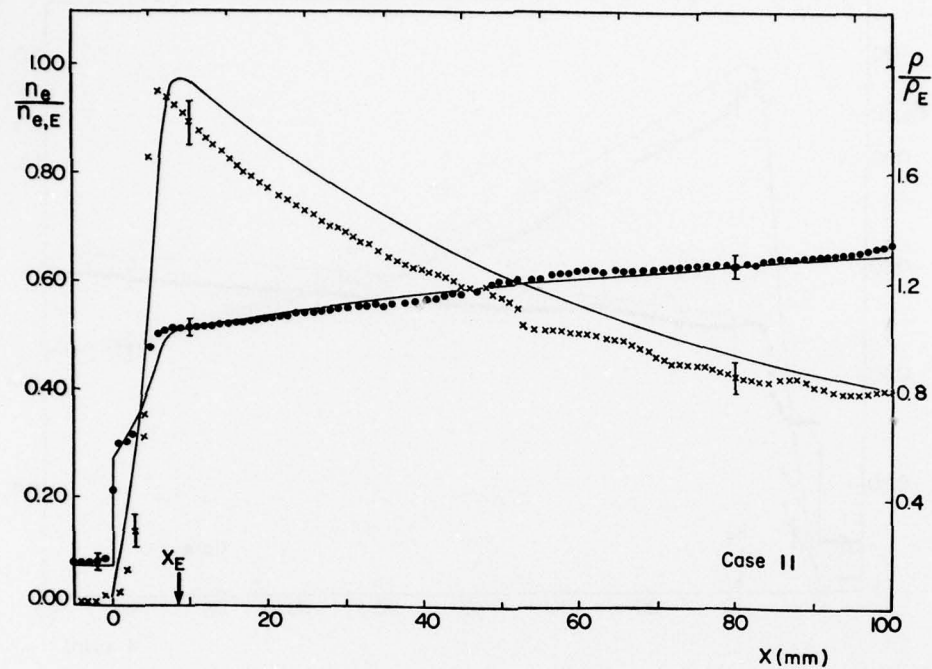


FIG. 40 VARIATION OF NONDIMENSIONALIZED DEGREE OF IONIZATION ( $\alpha/\alpha_E$ ) WITH DISTANCE  $x$  FOR CASE II.

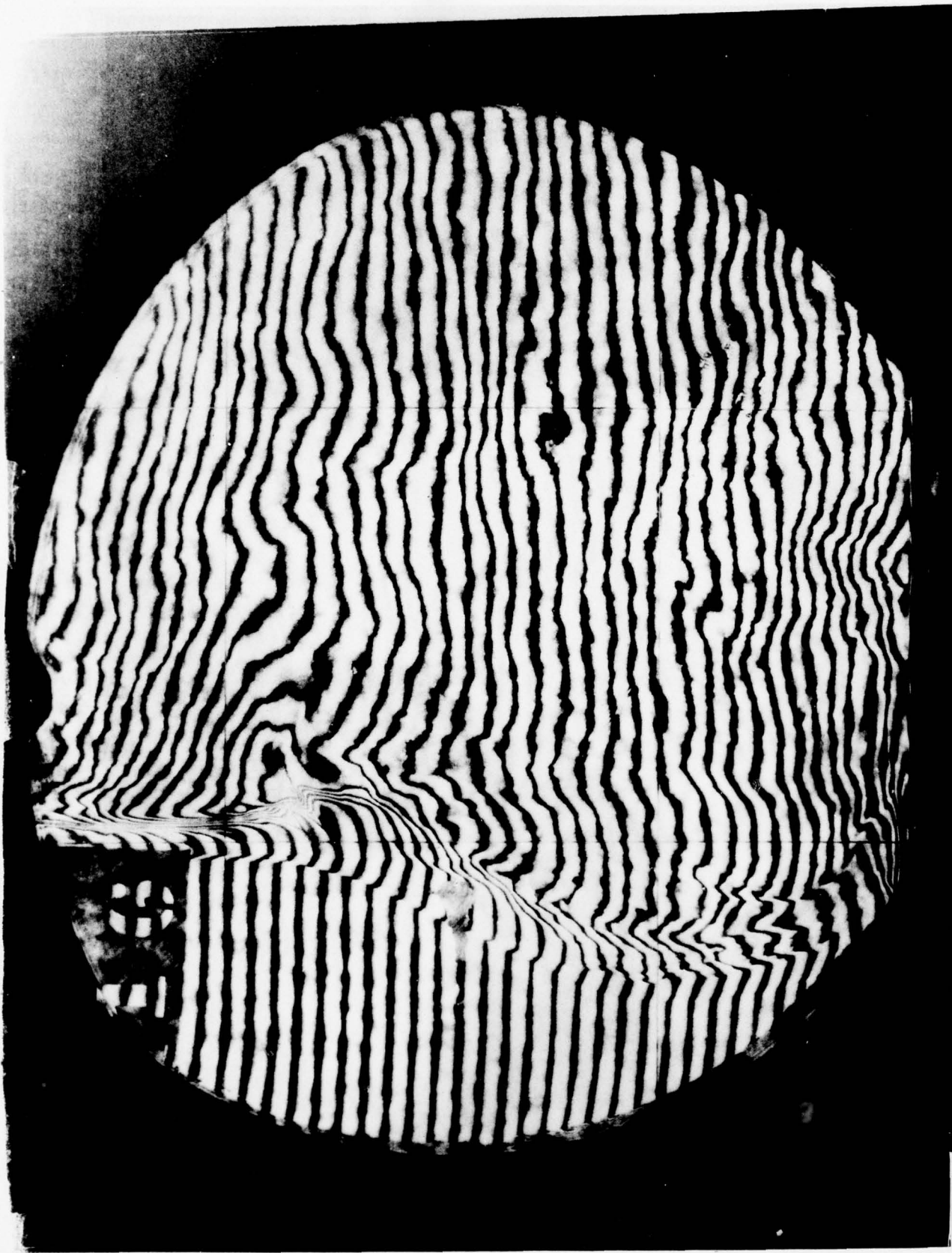


FIG. 41 INTERFEROGRAM OF A SHOCK WAVE TRAVELLING FROM RIGHT TO LEFT INTO ARGON ( $P_1 = 5.11$  TORR AND  $T_1 = 296.2$  K). TEST GAS WAS CONTAMINATED BY A "SMALL" BUT UNKNOWN AMOUNT OF WATER VAPOUR. MACH NUMBER  $M_s$  RECORDED WAS 18.5, BUT IS BELIEVED TO BE ERRONEOUS PERHAPS DUE TO OSCILLATING SHOCK FRONT.

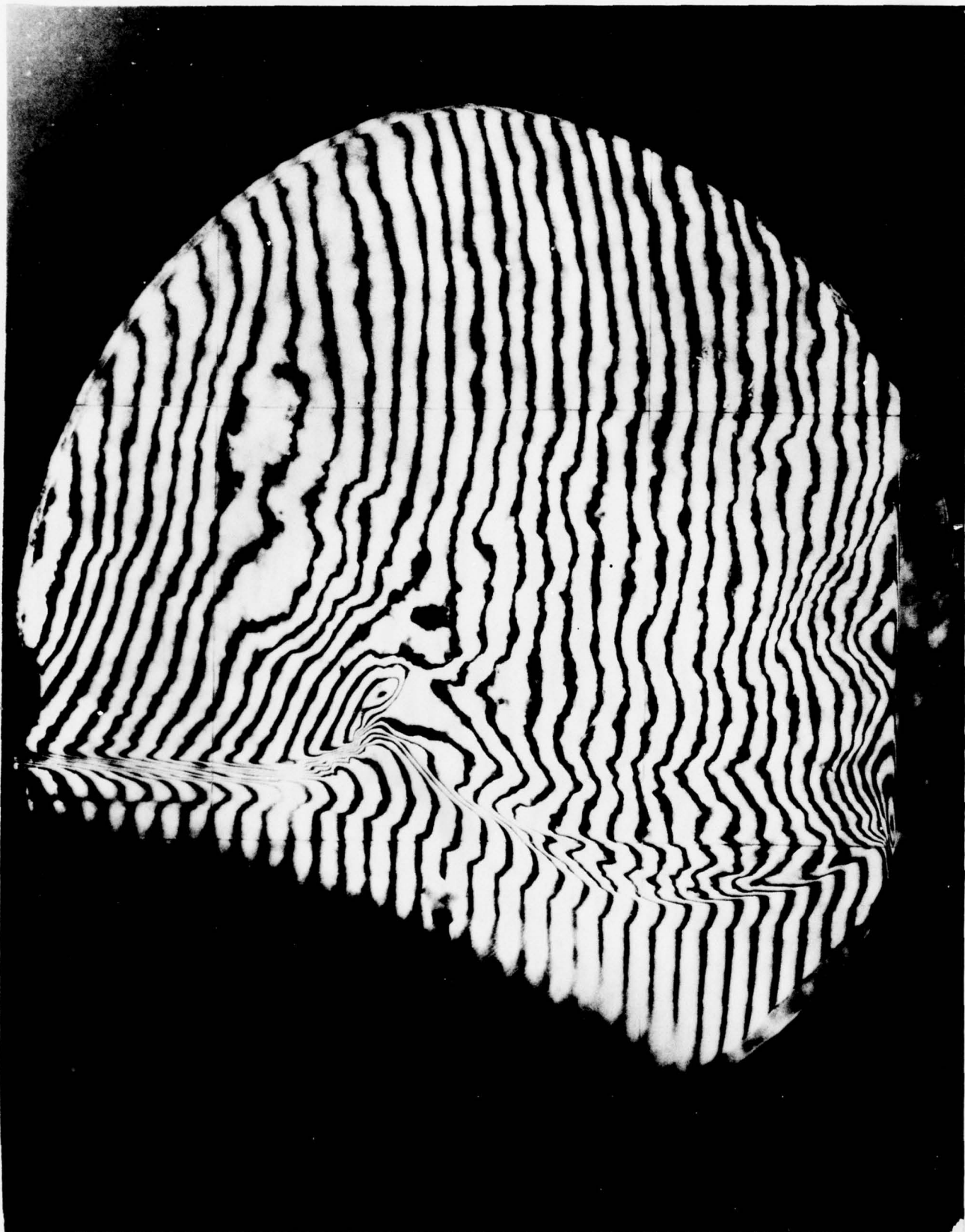


FIG. 42 INTERFERGRAM OF A SHOCK WAVE TRAVELLING FROM RIGHT TO LEFT INTO PURE ARGON ( $P_1 = 5.08$  TORR AND  $T_1 = 295.5$  K). TEST GAS WAS PROBABLY CONTAMINATED BY LEFT-OVER WATER VAPOUR TRAPPED INSIDE THE RESERVOIR DURING THE ADMISSION PROCESS. MACH NUMBER  $M_s$  RECORDED WAS 18.0, BUT IS BELIEVED TO BE ERRONEOUS PERHAPS DUE TO OSCILLATING SHOCK FRONT.

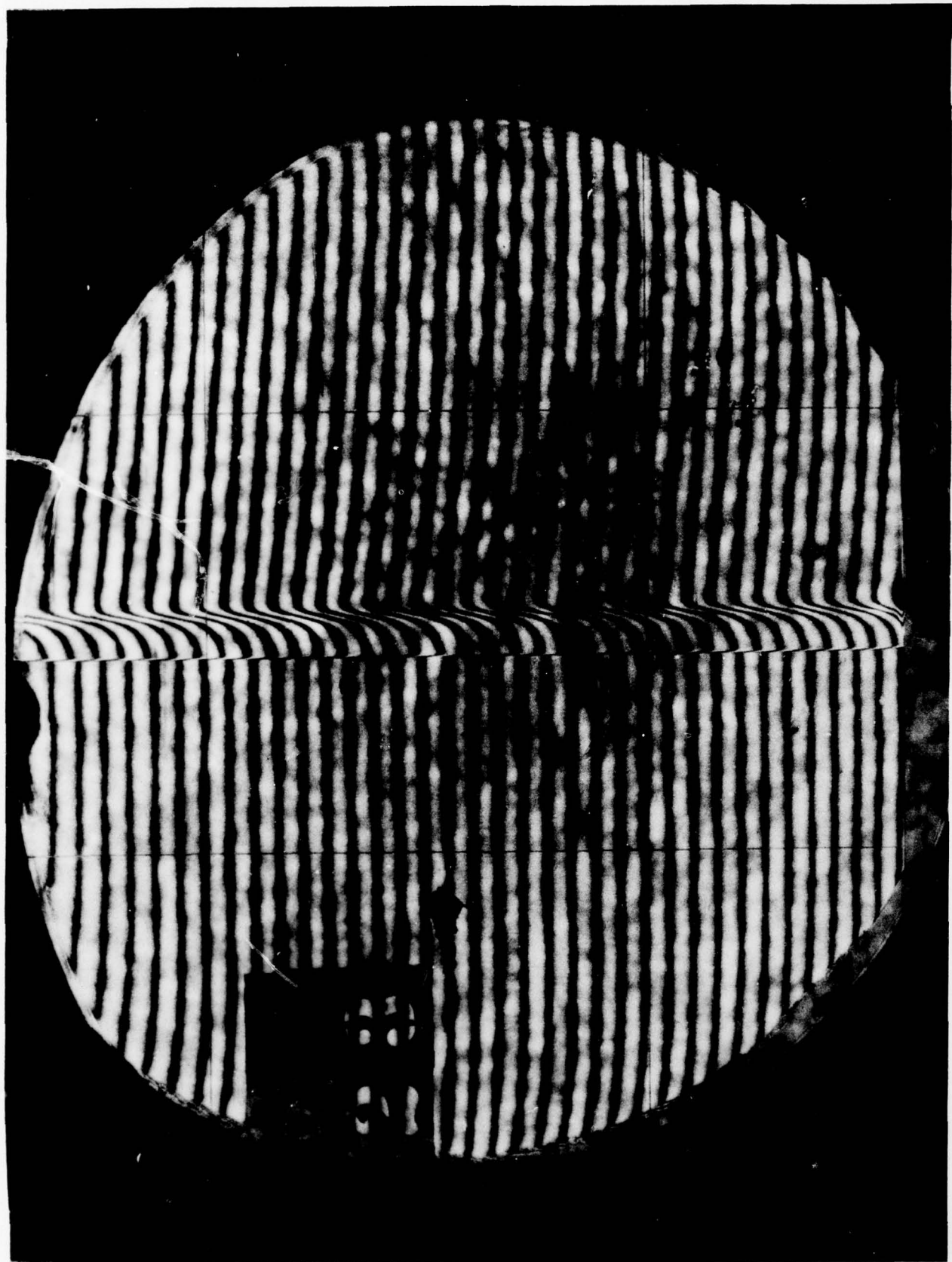


FIG. 43 INTERFEROGRAM OF A SHOCK WAVE  $M_s = 14.9$  TRAVELLING FROM RIGHT TO LEFT INTO ARGON WITH WATER VAPOUR IMPURITY,  $P_1 = 5.12$  TORR AND  $T_1 = 296.0$  K. HERE 0.25 ml OF DISTILLED WATER WAS INTRODUCED INTO THE TUBE, AND PRESSURE GAUGE REGISTERED 30 $\mu$  OR 0.78% WATER VAPOUR BY PRESSURE.

TABLE 1. GAS PRESSURE VARIATION WITH TIME

Amount of Water	Initial Pressure Reading (Ar) $t = 2$	Pressure Reading (Ar + H <sub>2</sub> O) at Later Time Intervals			
		$t = 2.5$	$t = 4$	$t = 5$	$t = 6$
1/2 ml	1500 $\mu$	1750 $\mu$	1600 $\mu$	1600 $\mu$	
1/2 ml	1500 $\mu$		1600 $\mu$		1550 $\mu$
1/4 ml	1300 $\mu$	1370 $\mu$	1340 $\mu$		
1/8 ml	2100 $\mu$		2150 $\mu$	2130 $\mu$	2115 $\mu$

$t$  denotes time in minutes after pumps are off

TABLE 2 CONSTANTS FOR INTERFEROMETRIC EQUATIONS

	$K_{A1}$ ( $\text{cm}^3/\text{gm}$ )	$K_{A2}$ ( $\text{cm}^3/\text{gm}$ )	$C_1$ ( $\text{cm}^3/\text{gm}$ )	$C_2$ ( $\text{cm}^3/\text{gm}$ )	$K$ ( $\text{cm}^6/\text{gm}^2$ )
Ar ( $K_1 = 0.67 K_A$ )	0.1573	0.1627	3.312	0.8686	0.4022
Kr ( $K_1 = 0.75 K_A$ )	0.1127	0.1188	1.581	0.4180	0.1407

TABLE 3 INITIAL CONDITIONS FOR CASES STUDIED

Interferograms from	Case	$M_s$	$P_1$ (Torr)	$T_1$ (K)	Gases
Present work	1	15.9	5.14	293.6	Ar
Present work	2	16.1	5.15	295.9	Ar
Brimelow, Ref. 30	3	16.5	5.12	296.6	Ar
Whitten, Ref. 29	4	13.0	5.01	296.6	Ar
Bristow, Ref. 11	5	17.2	2.60	293.3	Ar
Present work	6	15.2	5.07	295.4	Kr
Present work	7	15.1	5.15	296.2	Kr
Brimelow, Ref. 30	8	16.2	5.17	297.0	Ar + 0.4% $H_2$
Present work	9	17.7	3.12	298.2	Ar + 0.4% $H_2$
Present work	10	15.0	5.21	295.4	Kr + 0.38% $H_2$
Present work	11	15.1	5.16	297.1	Kr + 0.38% $H_2$

TABLE 4

THERMAL EQUILIBRIUM VALUES OF THE DENSITY  $\rho_E$ ,ELECTRON NUMBER DENSITY  $n_{e,E}$  AND DEGREE OF IONIZATION  $\alpha_E$  WITHOUT RADIATION LOSSES

Case	Gases	$\rho_E$ (gm/cm <sup>3</sup> )	$n_{e,E}$ (cm <sup>-3</sup> )	$\alpha_E$
1	Ar	$0.84 \times 10^{-4}$	$1.69 \times 10^{17}$	0.14
2	Ar	$0.87 \times 10^{-4}$	$1.83 \times 10^{17}$	0.15
3	Ar	$0.88 \times 10^{-4}$	$2.10 \times 10^{17}$	0.16
4	Ar	$0.62 \times 10^{-4}$	$5.62 \times 10^{16}$	0.06
5	Ar	$0.47 \times 10^{-4}$	$1.32 \times 10^{17}$	0.18
6	Kr	$0.17 \times 10^{-3}$	$1.71 \times 10^{17}$	0.14
7	Kr	$0.17 \times 10^{-3}$	$1.68 \times 10^{17}$	0.14
8	Ar + 0.4% $H_2$	$0.82 \times 10^{-4}$	$1.94 \times 10^{17}$	0.15
9	Ar + 0.4% $H_2$	$0.56 \times 10^{-4}$	$1.83 \times 10^{17}$	0.21
10	Kr + 0.38% $H_2$	$0.16 \times 10^{-3}$	$1.66 \times 10^{17}$	0.13
11	Kr + 0.38% $H_2$	$0.16 \times 10^{-3}$	$1.72 \times 10^{17}$	0.14

TABLE 5  
COMPARISON OF PREDICTED AND EXPERIMENTALLY MEASURED RELAXATION LENGTHS  $X_E$

Case	Gases	$M_S$	$P_1$ (Torr)	Theory (cm)	Experiment (cm)
1	Ar	15.9	5.14	2.1	2.0
2	Ar	16.1	5.15	2.0	1.9
3	Ar	16.5	5.12	1.7	1.8
4	Ar	13.0	5.01	10.9	8.9
5	Ar	17.2	2.60	2.7	1.6
6	Kr	15.2	5.07	1.9	1.8
7	Kr	15.1	5.15	1.9	1.8
8	Ar + 0.4% H <sub>2</sub>	16.2	5.17	0.77	0.65
9	Ar + 0.4% H <sub>2</sub>	17.7	3.12	0.80	0.75
10	Kr + 0.38% H <sub>2</sub>	15.0	5.21	0.90	0.80
11	Kr + 0.38% H <sub>2</sub>	15.1	5.16	0.85	0.63

APPENDIX A - ADDITIONAL RESULTS

The results presented in this Appendix were obtained from the same interferograms (but at different locations) used in Case 1 to Case 11. The initial conditions and thermal equilibrium values can be found in Tables 3 and 4. These results have been discussed in Section 5.

FIG. A1 VARIATIONS OF NONDIMENSIONALIZED ELECTRON NUMBER DENSITY ( $n_e/n_{e,E}$ ) AND DENSITY ( $\rho/\rho_E$ ) WITH DISTANCE  $x$  FOR CASE 1.

- $M_s = 16.2$  AND  $S_{Ar-Ar}^* = 0.9 \times 10^{-19} \text{ cm}^2/\text{eV}$
- $M_s = 15.9$  AND  $S_{Ar-Ar}^* = 1.0 \times 10^{-19} \text{ cm}^2/\text{eV}$
- ·-  $M_s = 15.6$  AND  $S_{Ar-Ar}^* = 1.1 \times 10^{-19} \text{ cm}^2/\text{eV}$

$P_1 = 5.14 \text{ TORR}$  AND  $T_1 = 293.6 \text{ K.}$

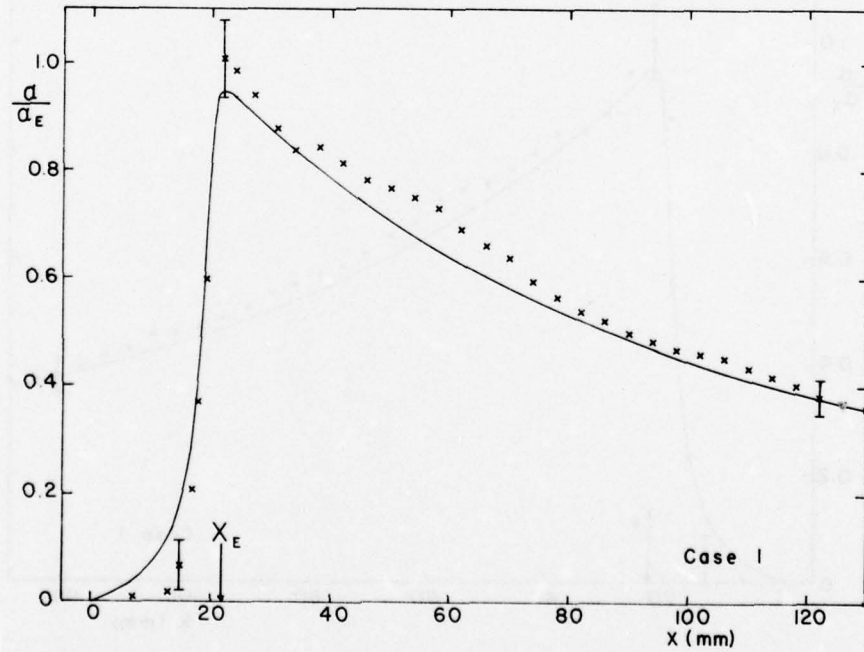
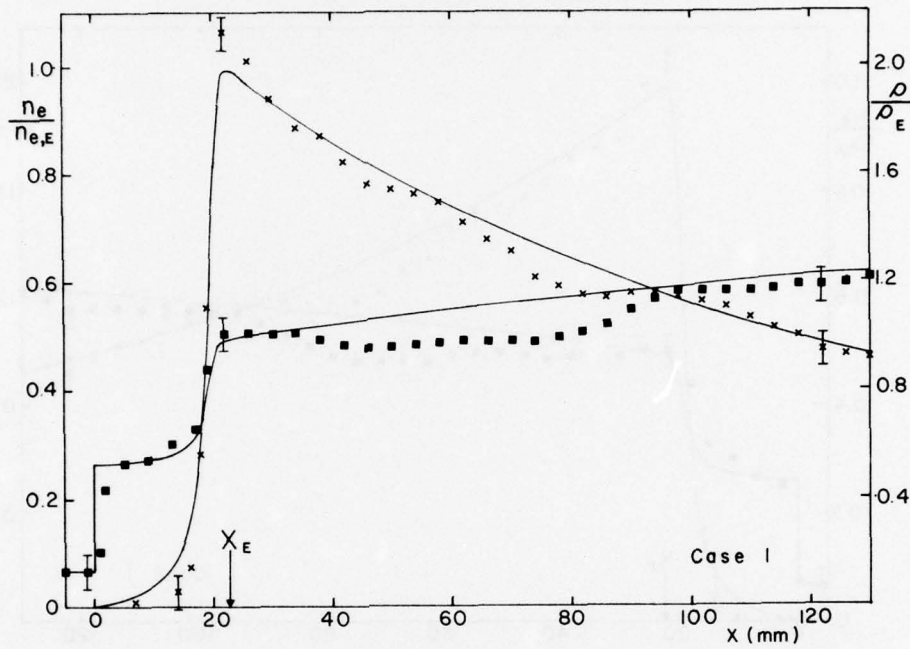


FIG. A2 VARIATION OF NONDIMENSIONALIZED DEGREE OF IONIZATION ( $\alpha/\alpha_E$ ) WITH DISTANCE  $x$  FOR CASE 1.

- $M_s = 16.2$  AND  $S_{Ar-Ar}^* = 0.9 \times 10^{-19} \text{ cm}^2/\text{eV}$
- $M_s = 15.9$  AND  $S_{Ar-Ar}^* = 1.0 \times 10^{-19} \text{ cm}^2/\text{eV}$
- ·-  $M_s = 15.6$  AND  $S_{Ar-Ar}^* = 1.1 \times 10^{-19} \text{ cm}^2/\text{eV}$

$P_1 = 5.14 \text{ TORR}$  AND  $T_1 = 293.6 \text{ K.}$

FIG. A3 VARIATIONS OF NONDIMENSIONALIZED ELECTRON NUMBER DENSITY ( $n_e/n_{e,E}$ ) AND DENSITY ( $\rho/\rho_E$ ) WITH DISTANCE  $x$  FOR CASE 1.

- $M_s = 16.2$  AND  $S_{Ar-Ar}^* = 0.9 \times 10^{-19} \text{ cm}^2/\text{eV}$
- $M_s = 15.9$  AND  $S_{Ar-Ar}^* = 1.0 \times 10^{-19} \text{ cm}^2/\text{eV}$
- · -  $M_s = 15.6$  AND  $S_{Ar-Ar}^* = 1.1 \times 10^{-19} \text{ cm}^2/\text{eV}$

$P_1 = 5.14 \text{ TORR AND } T_1 = 293.6 \text{ K.}$

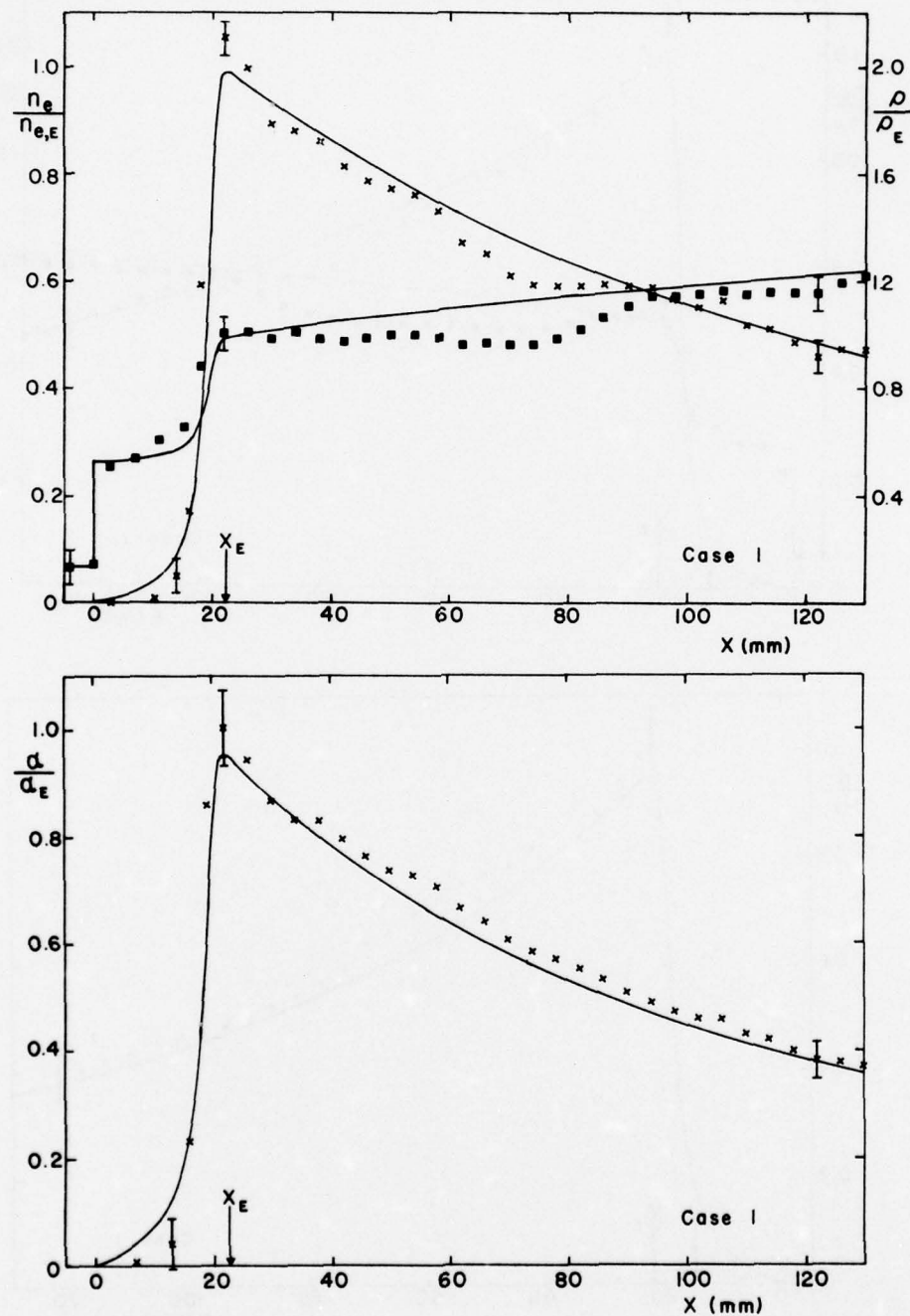


FIG. A4 VARIATION OF NONDIMENSIONALIZED DEGREE OF IONIZATION ( $\alpha/\alpha_E$ ) WITH DISTANCE  $x$  FOR CASE 1.

- $M_s = 16.2$  AND  $S_{Ar-Ar}^* = 0.9 \times 10^{-19} \text{ cm}^2/\text{eV}$
- $M_s = 15.9$  AND  $S_{Ar-Ar}^* = 1.0 \times 10^{-19} \text{ cm}^2/\text{eV}$
- · -  $M_s = 15.6$  AND  $S_{Ar-Ar}^* = 1.1 \times 10^{-19} \text{ cm}^2/\text{eV}$

$P_1 = 5.14 \text{ TORR AND } T_1 = 293.6 \text{ K.}$

FIG. A5 VARIATIONS OF NONDIMENSIONALIZED ELECTRON NUMBER DENSITY ( $n_e/n_{e,E}$ ) AND DENSITY ( $\rho/\rho_E$ ) WITH DISTANCE  $x$  FOR CASE 3.

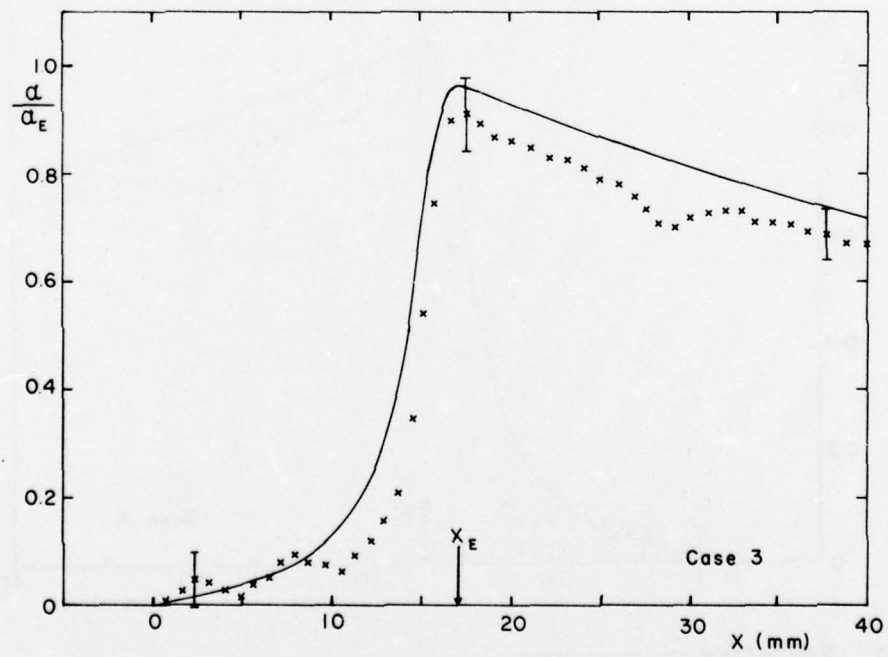
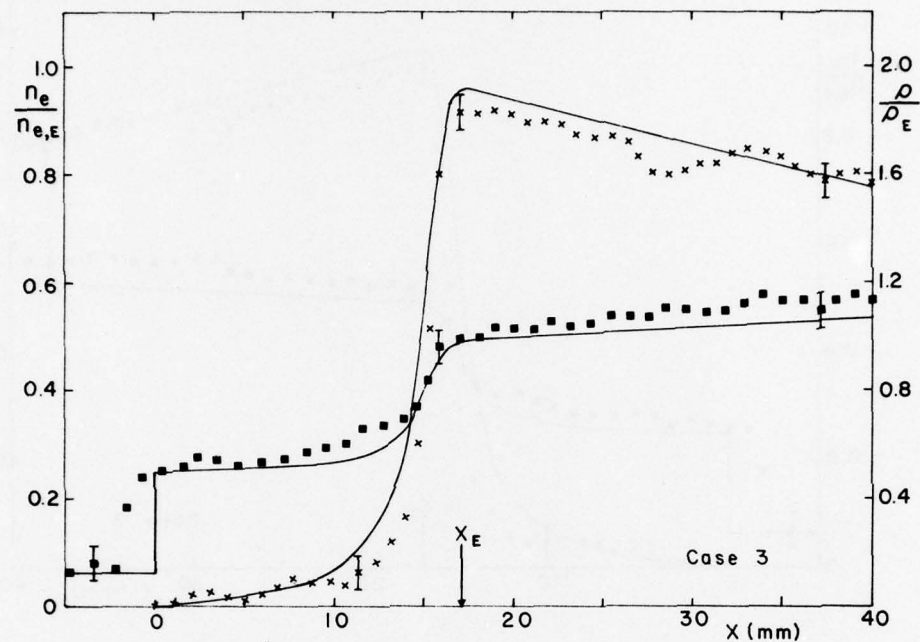


FIG. A6 VARIATION OF NONDIMENSIONALIZED DEGREE OF IONIZATION ( $\alpha/\alpha_E$ ) WITH DISTANCE  $x$  FOR CASE 3.

FIG. A7 VARIATIONS OF NONDIMENSIONALIZED ELECTRON NUMBER DENSITY ( $n_e/n_{e,E}$ ) AND DENSITY ( $\rho/\rho_E$ ) WITH DISTANCE  $x$  FOR CASE 3.

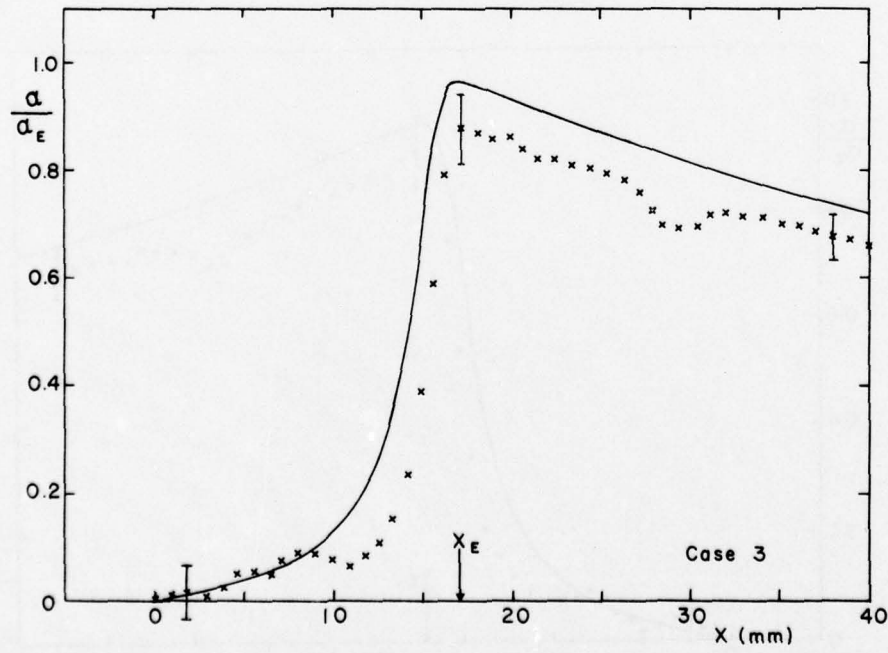
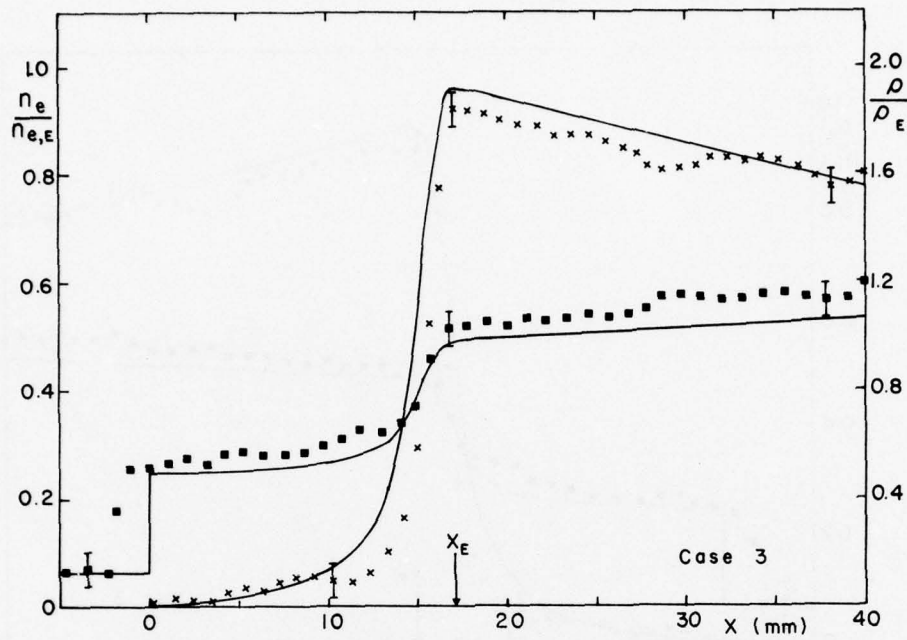
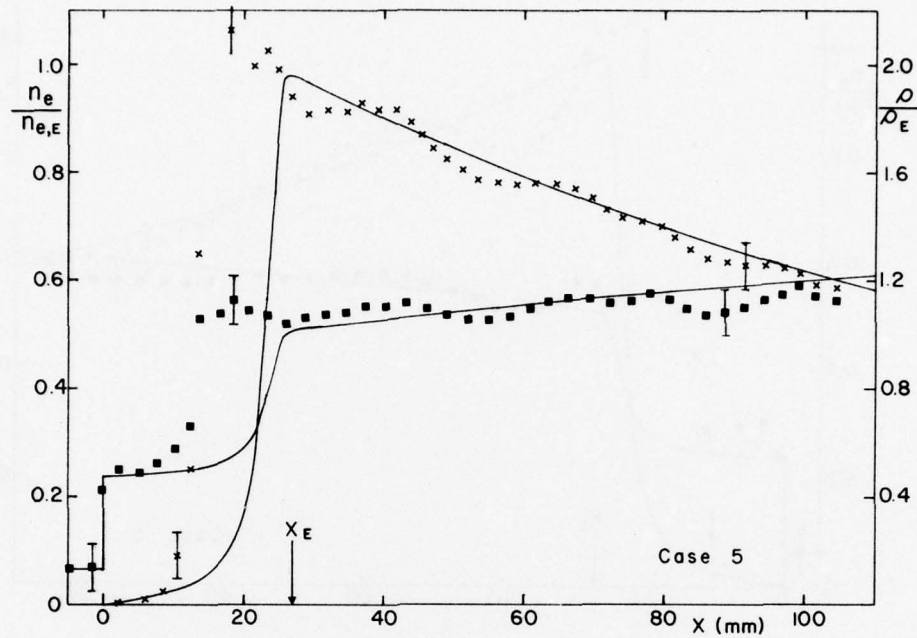


FIG. A8 VARIATION OF NONDIMENSIONALIZED DEGREE OF IONIZATION ( $\alpha/\alpha_E$ ) WITH DISTANCE  $x$  FOR CASE 3.

FIG. A9

VARIATIONS OF NONDIMENSIONALIZED ELECTRON NUMBER DENSITY ( $n_e/n_{e,E}$ ) AND DENSITY ( $\rho/\rho_E$ ) WITH DISTANCE  $x$  FOR CASE 5.



Case 5

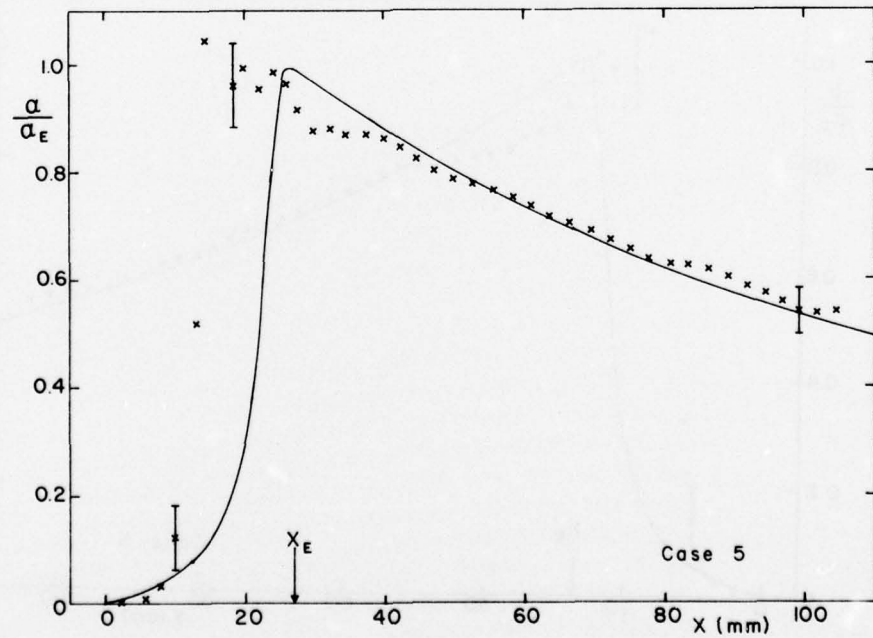


FIG. A10

VARIATION OF NONDIMENSIONALIZED DEGREE OF IONIZATION ( $\alpha/\alpha_E$ ) WITH DISTANCE  $x$  FOR CASE 5.

FIG. A11 VARIATIONS OF NONDIMENSIONALIZED ELECTRON NUMBER DENSITY ( $n_e/n_{e,E}$ ) AND DENSITY ( $\rho/\rho_E$ ) WITH DISTANCE  $x$  FOR CASE 5.

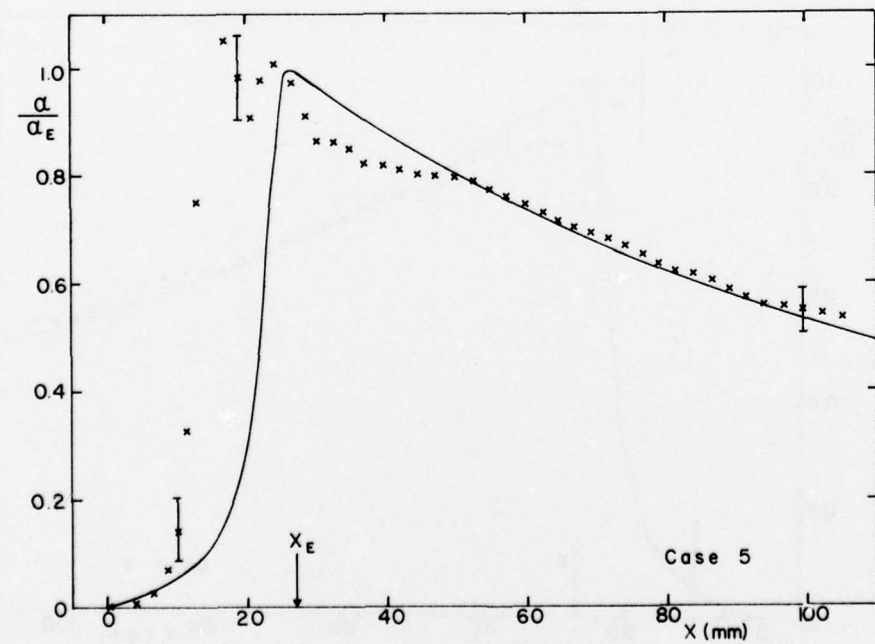
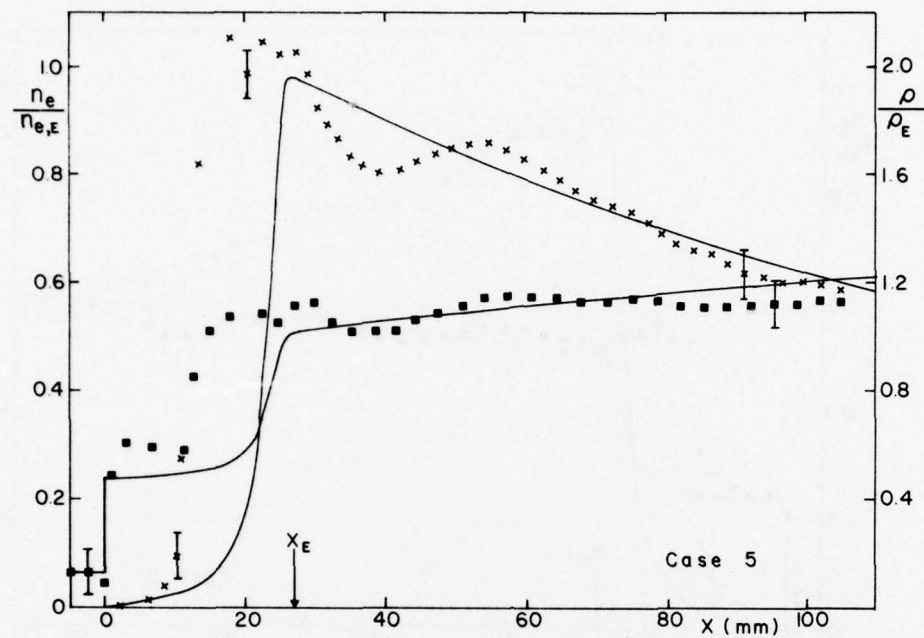


FIG. A12 VARIATION OF NONDIMENSIONALIZED DEGREE OF IONIZATION ( $\alpha/\alpha_E$ ) WITH DISTANCE  $x$  FOR CASE 5.

FIG. A13 VARIATIONS OF NONDIMENSIONALIZED ELECTRON NUMBER DENSITY ( $n_e/n_{e,E}$ ) AND DENSITY ( $\rho/\rho_E$ ) WITH DISTANCE  $x$  FOR CASE 6.

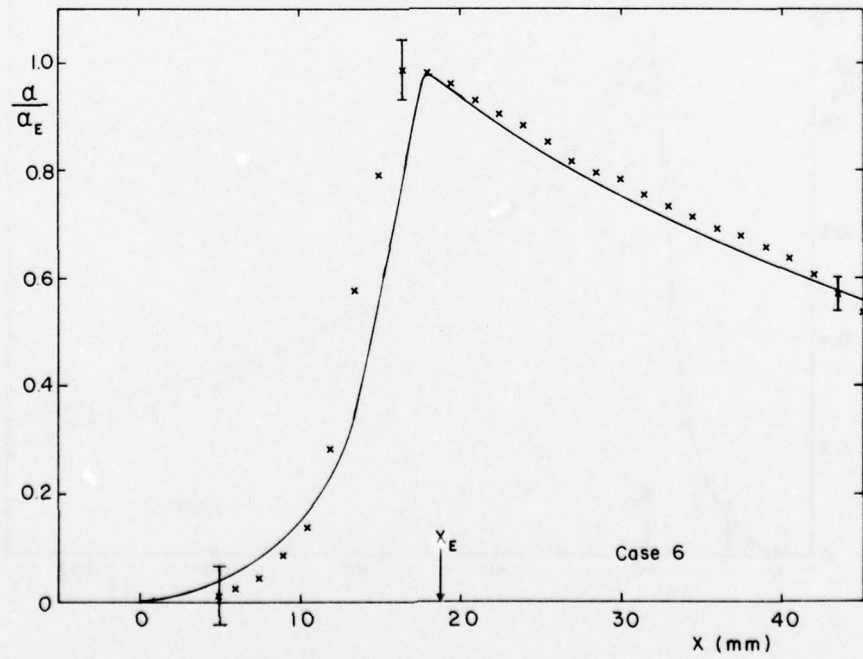
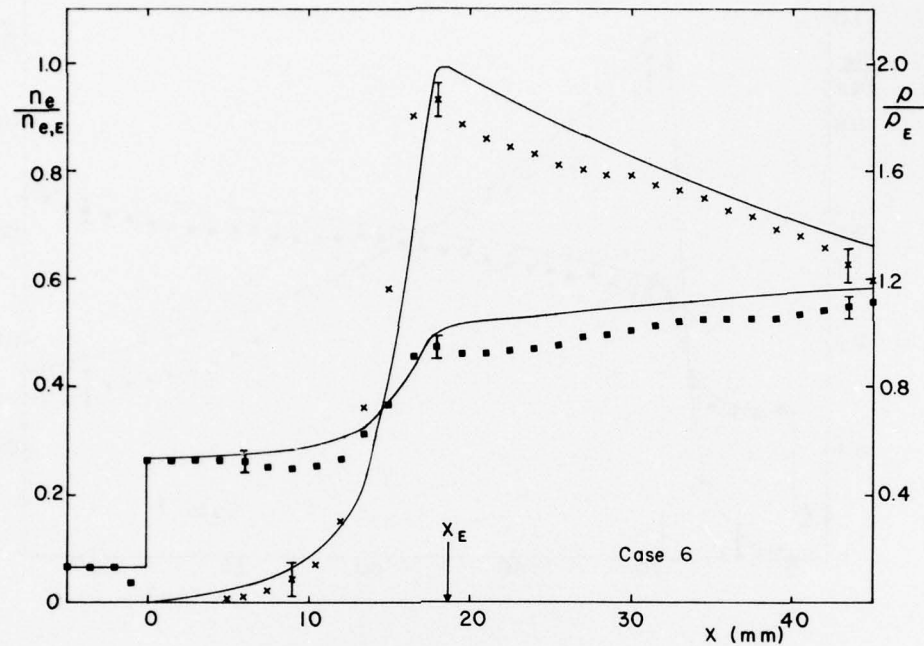


FIG. A14 VARIATION OF NONDIMENSIONALIZED DEGREE OF IONIZATION ( $\alpha/\alpha_E$ ) WITH DISTANCE  $x$  FOR CASE 6

FIG. A15 VARIATIONS OF NONDIMENSIONALIZED ELECTRON NUMBER DENSITY ( $n_e/n_{e,E}$ ) AND DENSITY ( $\rho/\rho_E$ ) WITH DISTANCE  $x$  FOR CASE 7.

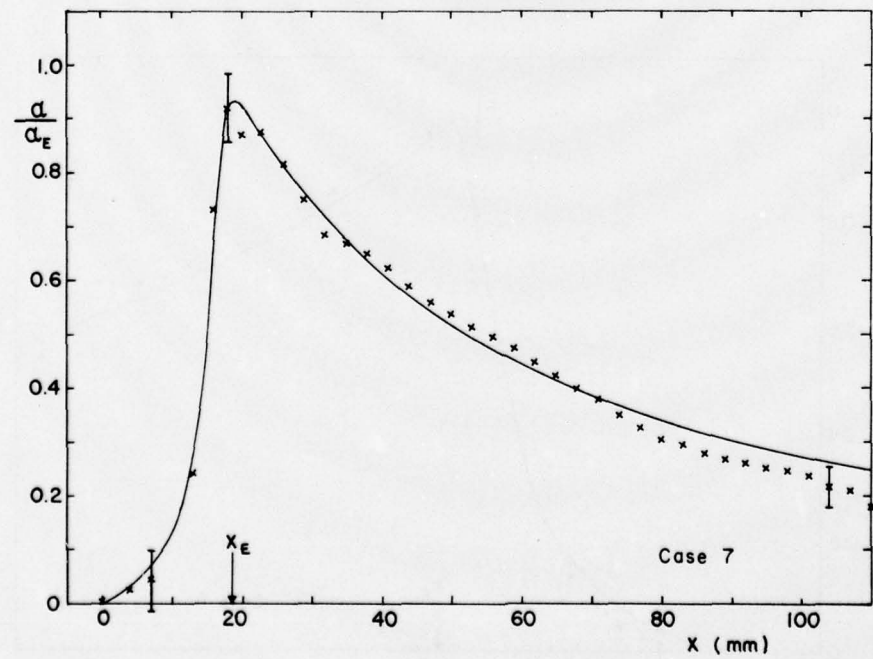
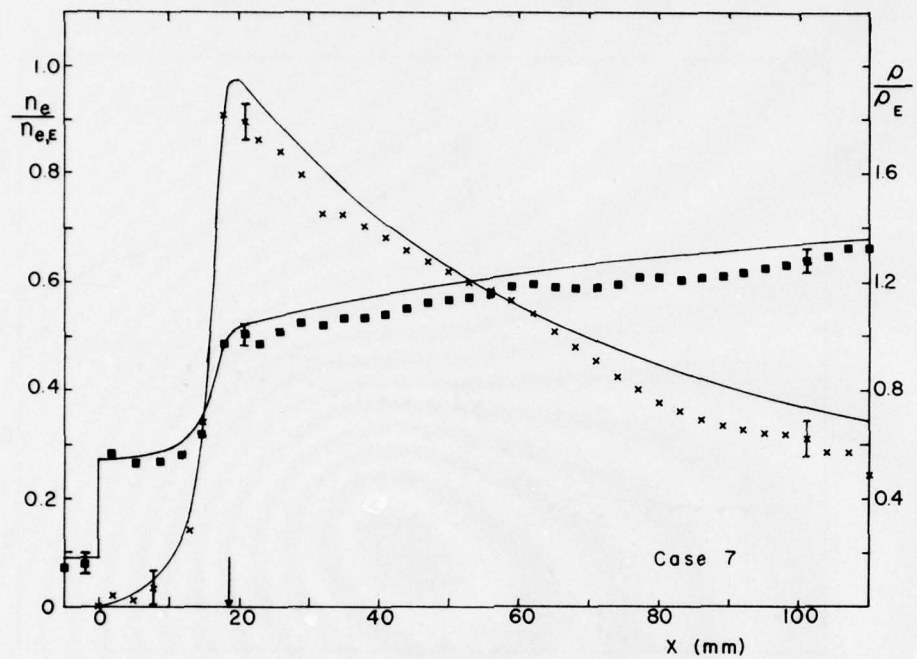


FIG. A16 VARIATION OF NONDIMENSIONALIZED DEGREE OF IONIZATION ( $\alpha/\alpha_E$ ) WITH DISTANCE  $x$  FOR CASE 7.

FIG. A17 VARIATIONS OF NONDIMENSIONALIZED ELECTRON NUMBER DENSITY ( $n_e/n_{e,E}$ ) AND DENSITY ( $\rho/\rho_E$ ) WITH DISTANCE  $x$  FOR CASE 7.

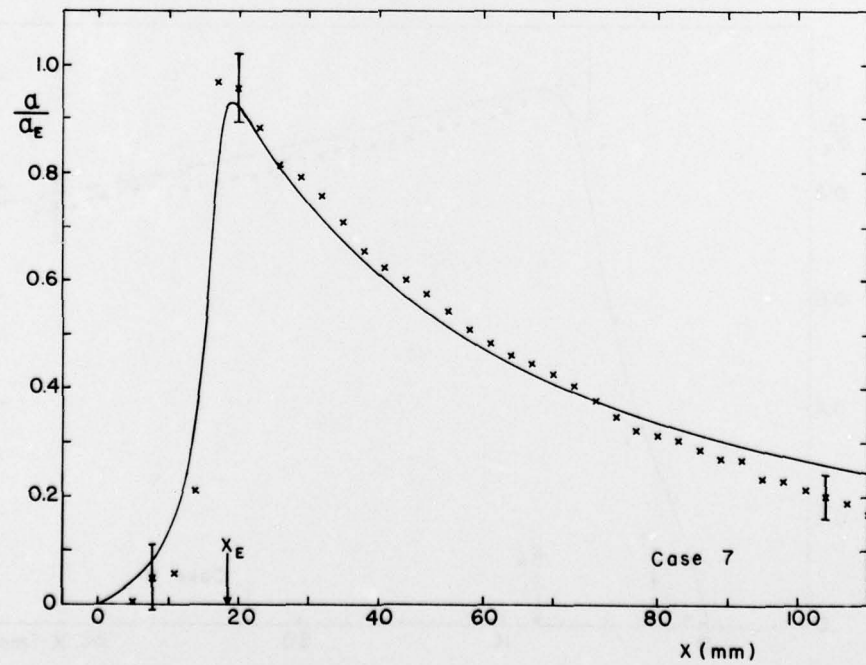
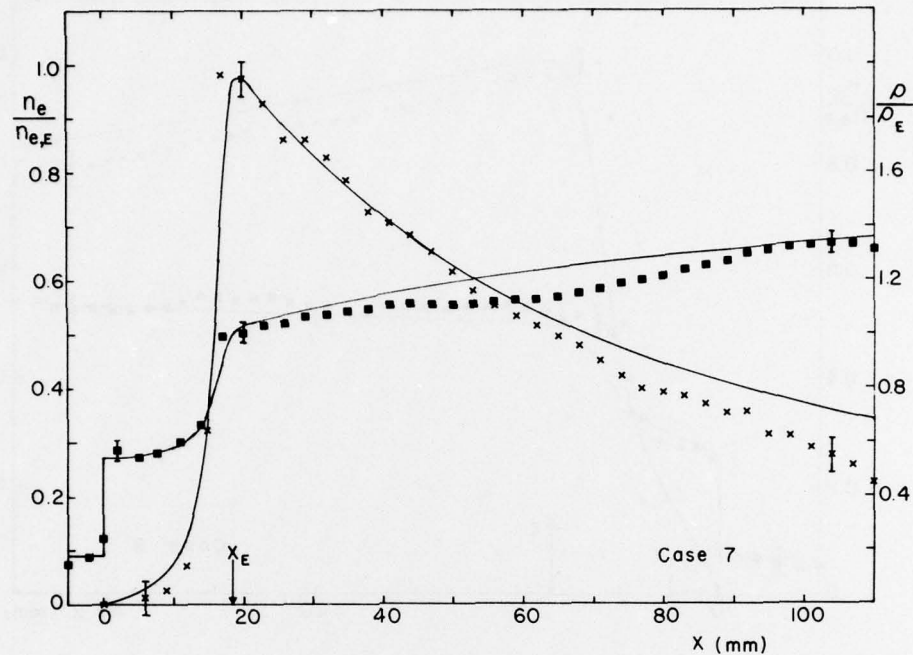


FIG. A18 VARIATION OF NONDIMENSIONALIZED DEGREE OF IONIZATION ( $\alpha/\alpha_E$ ) WITH DISTANCE  $x$  FOR CASE 7.

FIG. A19 VARIATIONS OF NONDIMENSIONALIZED ELECTRON NUMBER DENSITY ( $n_e/n_{e,E}$ ) AND DENSITY ( $\rho/\rho_E$ ) WITH DISTANCE  $x$  FOR CASE 8.

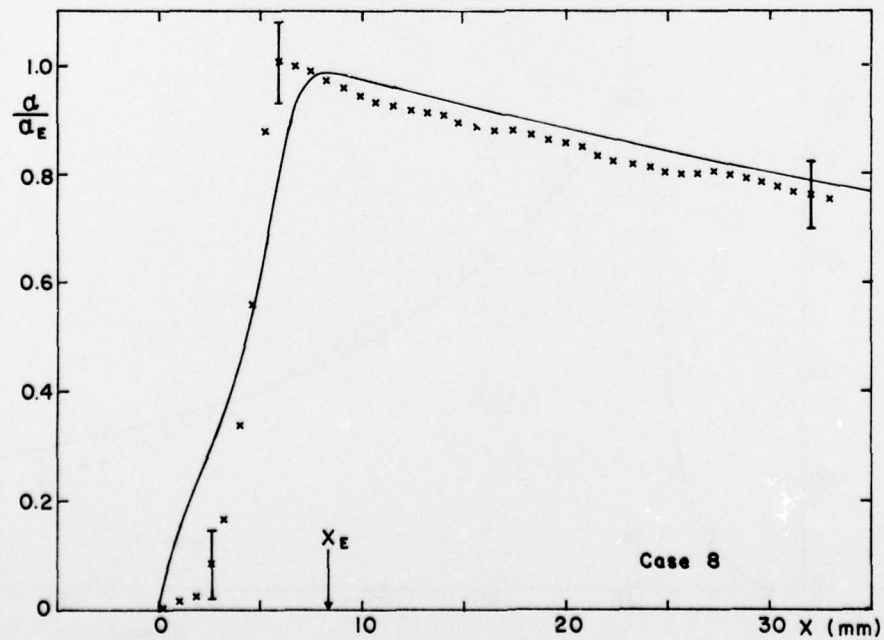
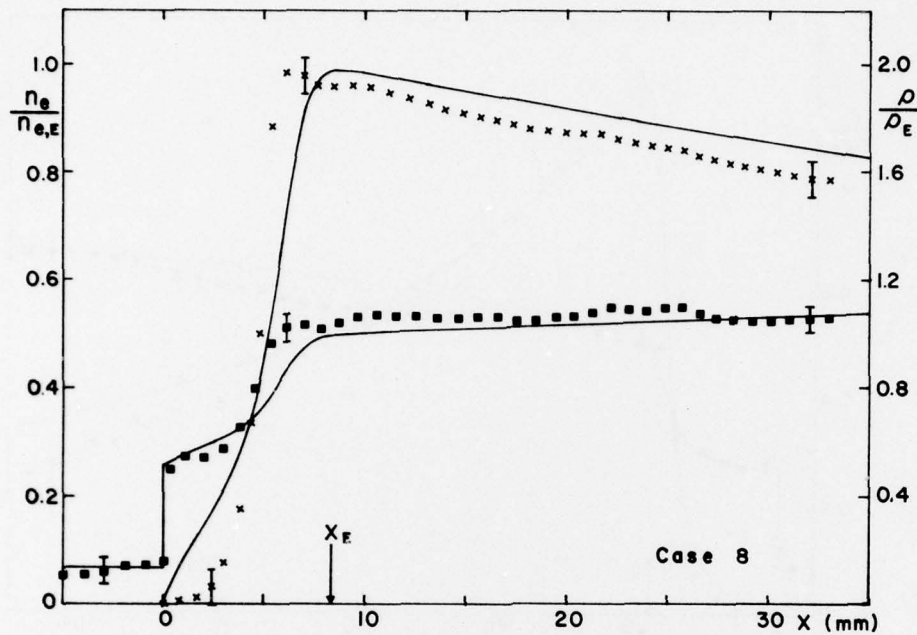


FIG. A20 VARIATION OF NONDIMENSIONALIZED DEGREE OF IONIZATION ( $\alpha/\alpha_E$ ) WITH DISTANCE  $x$  FOR CASE 8.

FIG. A21 VARIATIONS OF NONDIMENSIONALIZED ELECTRON NUMBER DENSITY ( $n_e/n_{e,E}$ ) AND DENSITY ( $\rho/\rho_{e,E}$ ) WITH DISTANCE  $x$  FOR CASE 8.

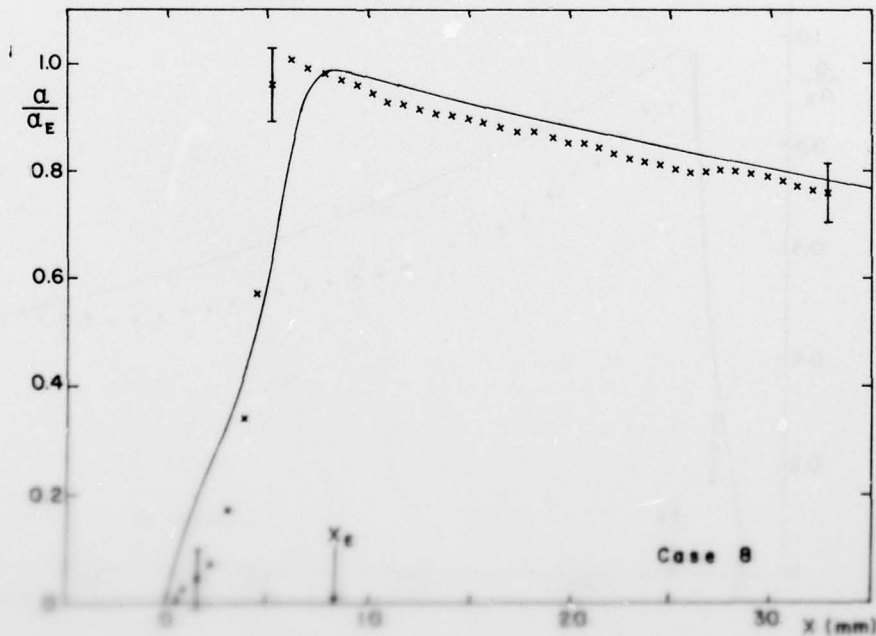
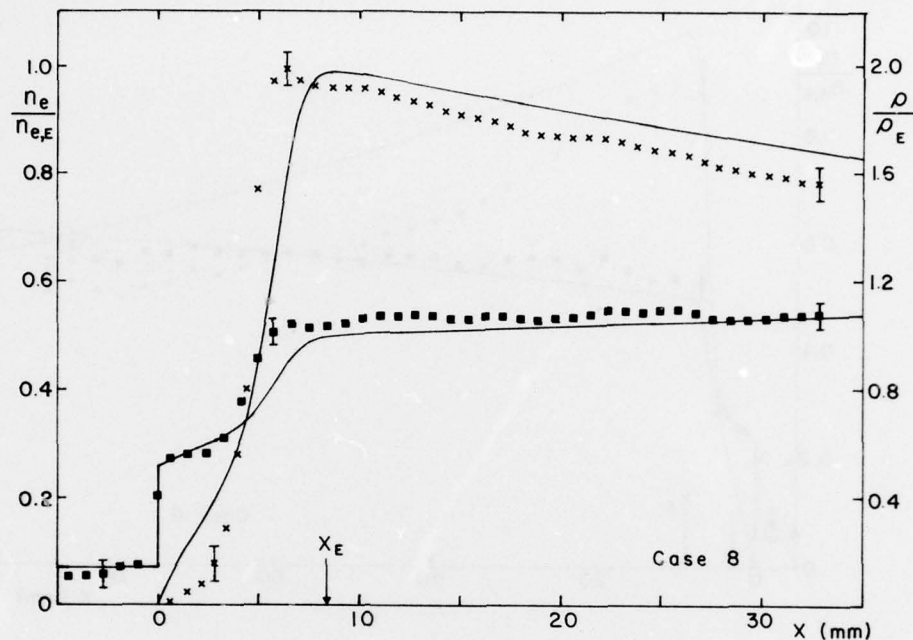


FIG. A22 VARIATION OF NONDIMENSIONALIZED DEGREE OF IONIZATION ( $\alpha/\alpha_E$ ) WITH DISTANCE  $x$  FOR CASE 8.

FIG. A23 VARIATIONS OF NONDIMENSIONALIZED ELECTRON NUMBER DENSITY ( $n_e/n_{e,E}$ ) AND DENSITY ( $\rho/\rho_E$ ) WITH DISTANCE  $x$  FOR CASE 9.

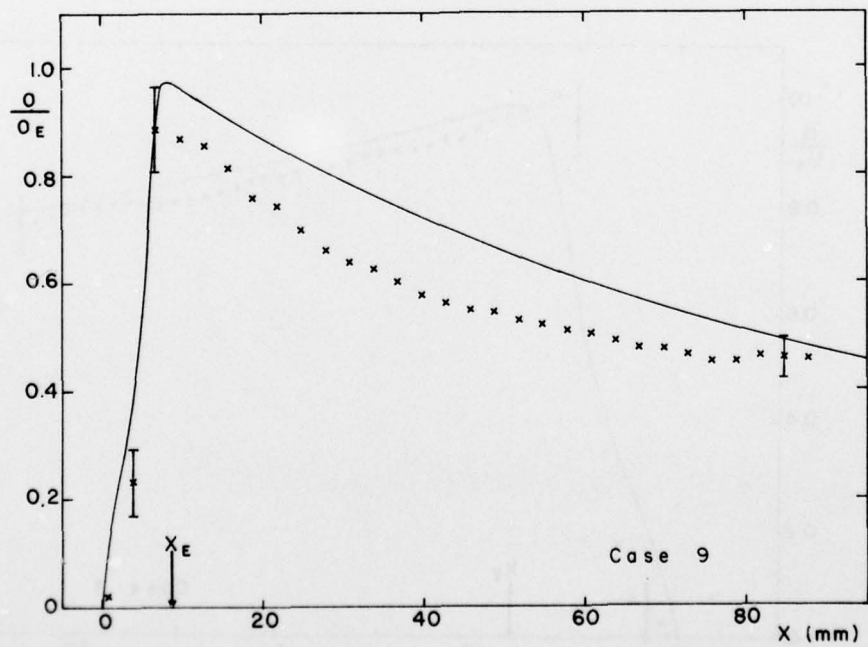
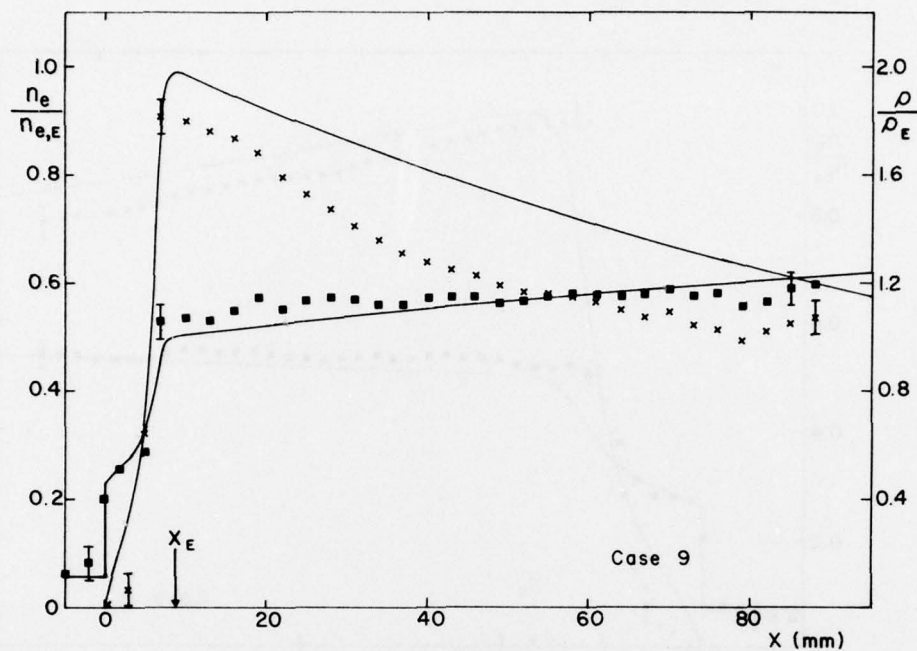


FIG. A24 VARIATION OF NONDIMENSIONALIZED DEGREE OF IONIZATION ( $\alpha/\alpha_E$ ) WITH DISTANCE  $x$  FOR CASE 9.

FIG. A25 VARIATIONS OF NONDIMENSIONALIZED ELECTRON NUMBER DENSITY ( $n_e/n_{e,E}$ ) AND DENSITY ( $\rho/\rho_E$ ) WITH DISTANCE  $x$  FOR CASE 9.

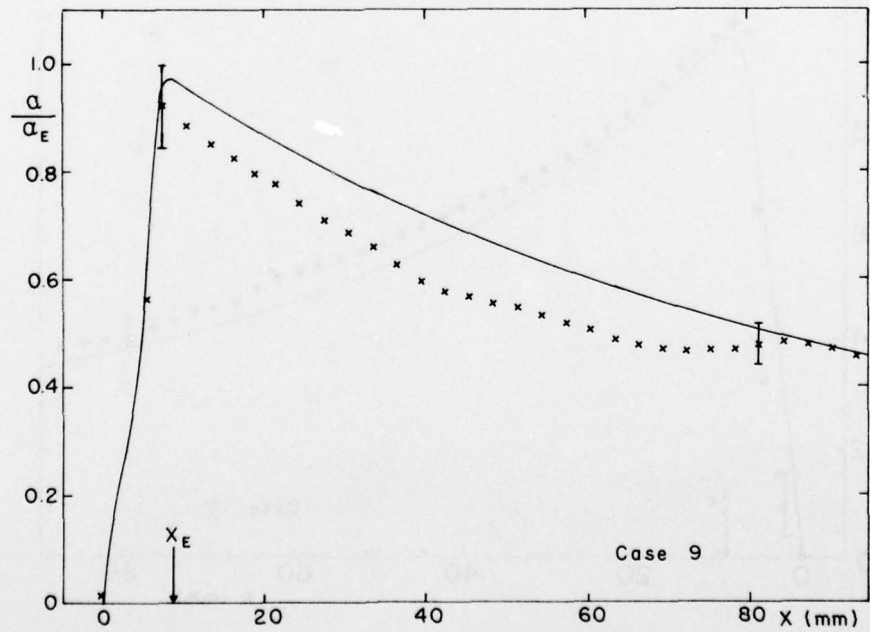
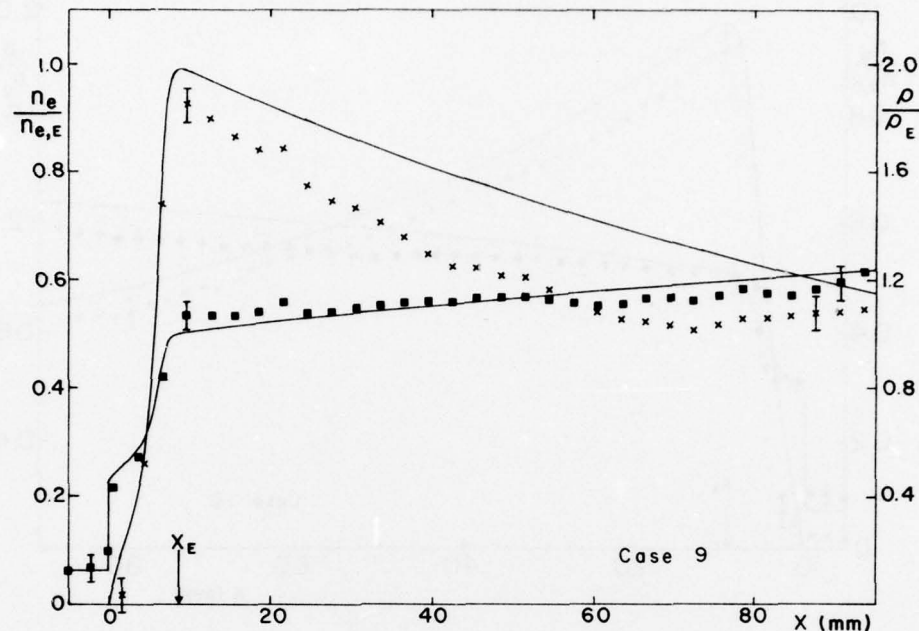


FIG. A26 VARIATION OF NONDIMENSIONALIZED DEGREE OF IONIZATION ( $\alpha/\alpha_E$ ) WITH DISTANCE  $x$  FOR CASE 9.

FIG. A27 VARIATIONS OF NONDIMENSIONALIZED ELECTRON NUMBER DENSITY ( $n_e/n_{e,E}$ ) AND DENSITY ( $\rho/\rho_E$ ) WITH DISTANCE  $x$  FOR CASE 10.

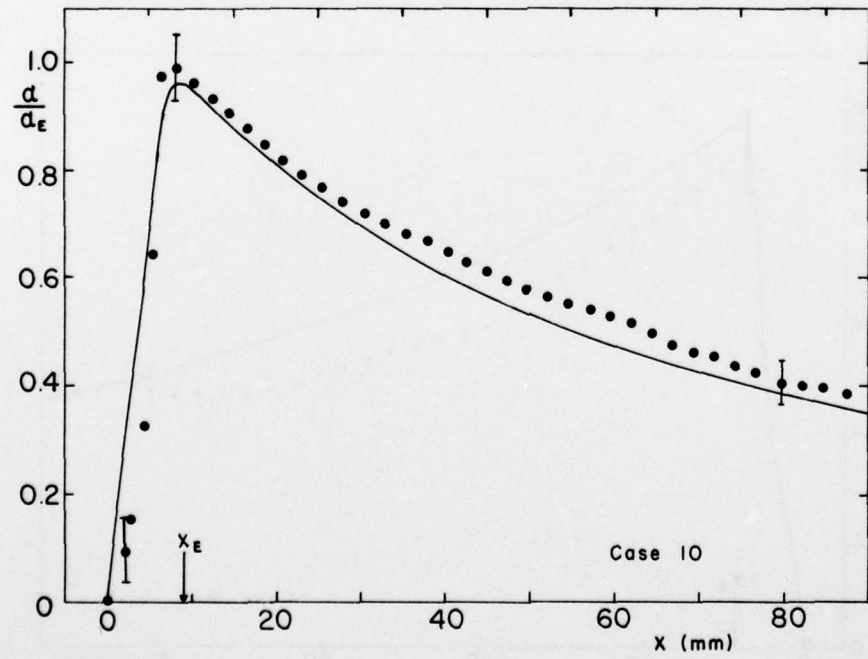
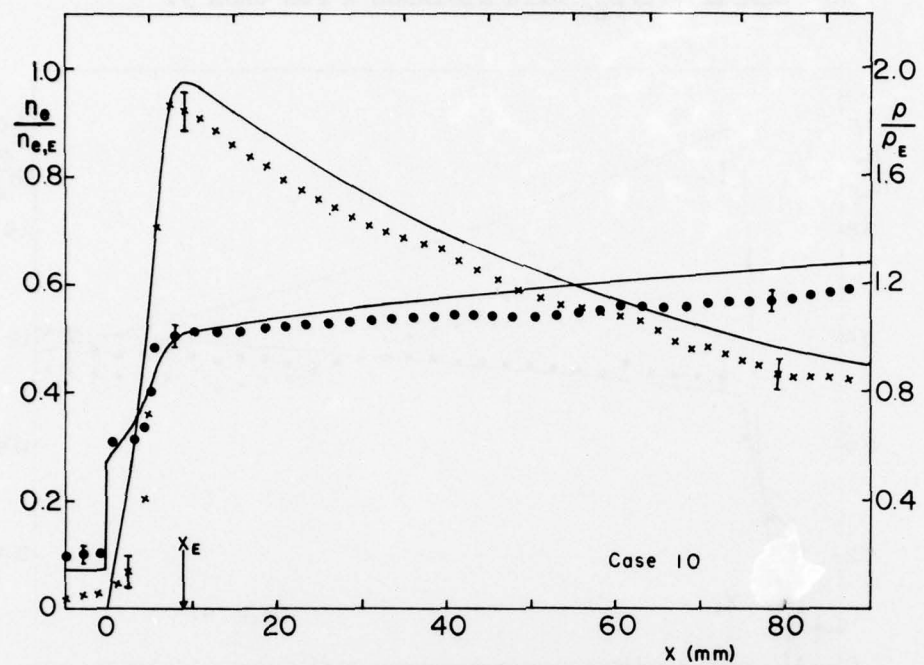


FIG. A28 VARIATION OF NONDIMENSIONALIZED DEGREE OF IONIZATION ( $\alpha/\alpha_E$ ) WITH DISTANCE  $x$  FOR CASE 10.

FIG. A29 VARIATIONS OF NONDIMENSIONALIZED ELECTRON NUMBER DENSITY ( $n_e/n_{e,E}$ ) AND DENSITY ( $\rho/\rho_E$ ) WITH DISTANCE  $x$  FOR CASE 10.

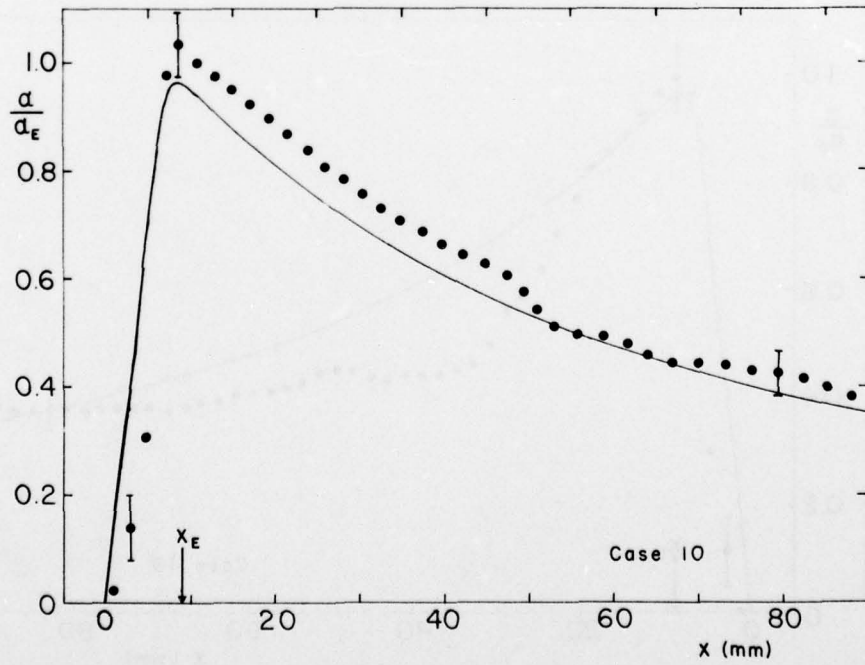
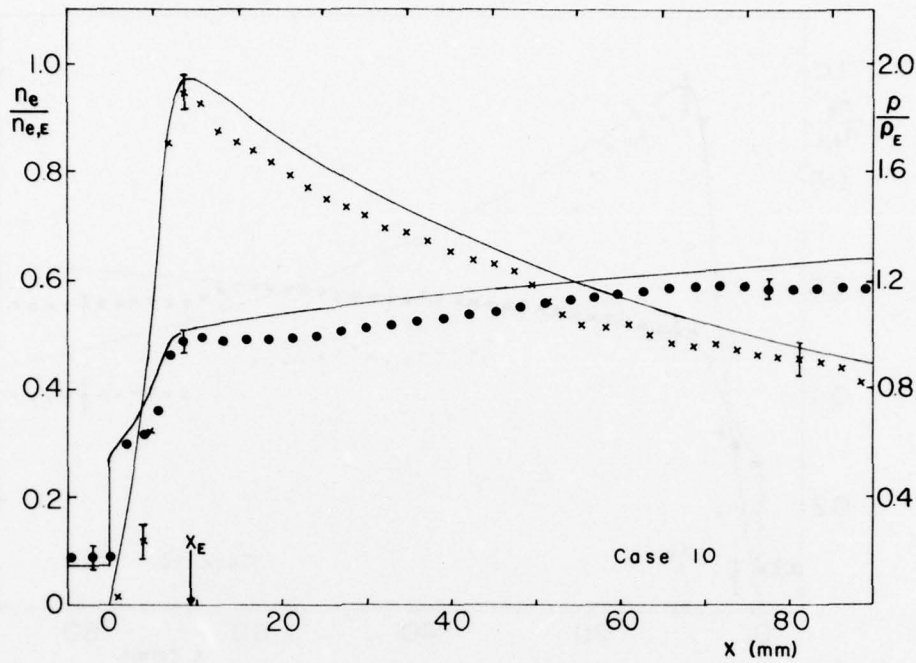


FIG. A30 VARIATION OF NONDIMENSIONALIZED DEGREE OF IONIZATION ( $\alpha/\alpha_E$ ) WITH DISTANCE  $x$  FOR CASE 10.

FIG. A31 VARIATIONS OF NONDIMENSIONALIZED ELECTRON NUMBER DENSITY ( $n_e/n_{e,E}$ ) AND DENSITY ( $\rho/\rho_E$ ) WITH DISTANCE  $x$  FOR CASE 10.

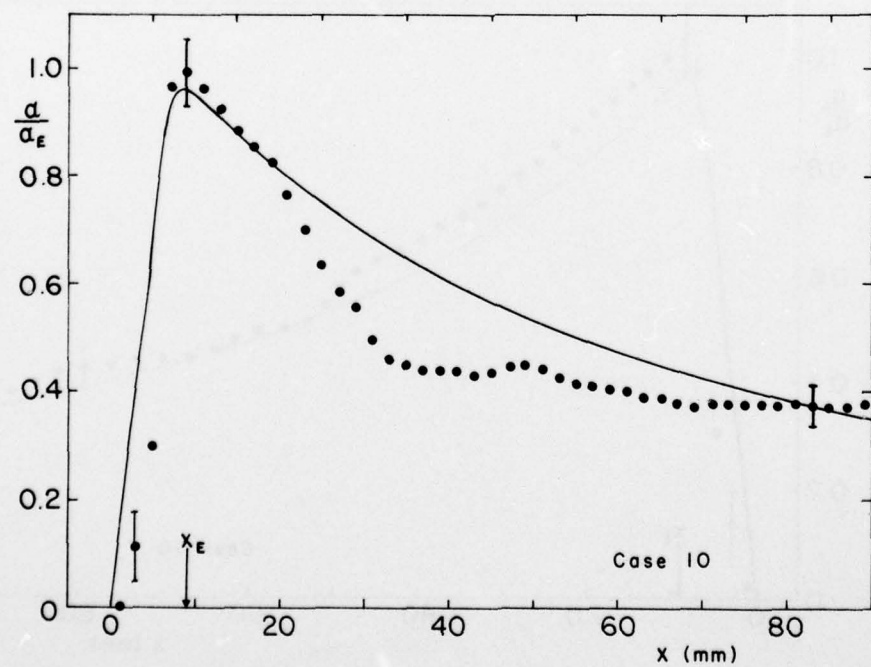
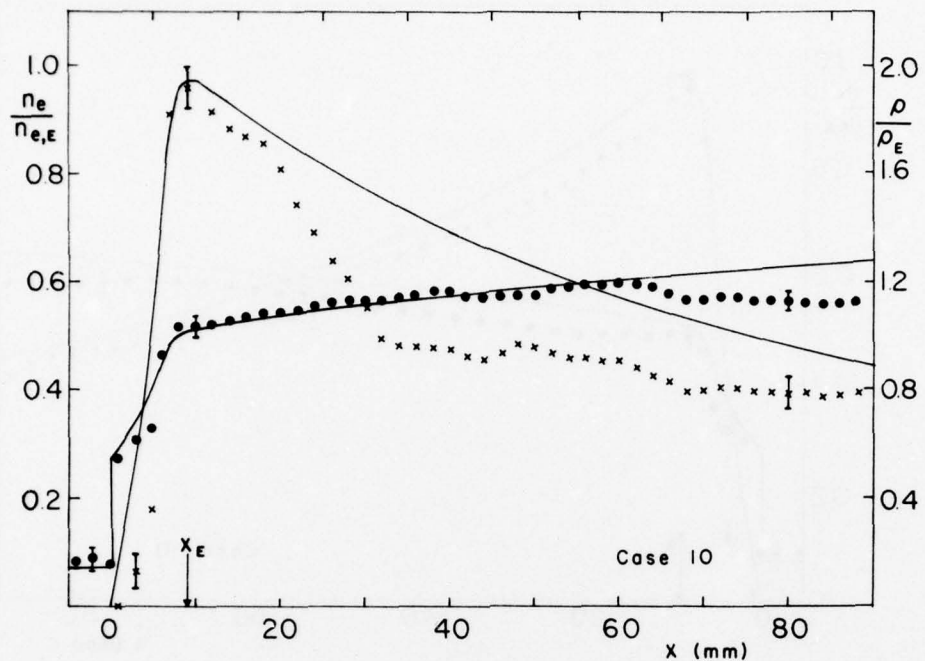


FIG. A32 VARIATION OF NONDIMENSIONALIZED DEGREE OF IONIZATION ( $\alpha/\alpha_E$ ) WITH DISTANCE  $x$  FOR CASE 10.

FIG. A33 VARIATIONS OF NONDIMENSIONALIZED ELECTRON NUMBER DENSITY ( $n_e/n_{e,E}$ ) AND DENSITY ( $\rho/\rho_E$ ) WITH DISTANCE  $x$  FOR CASE II.

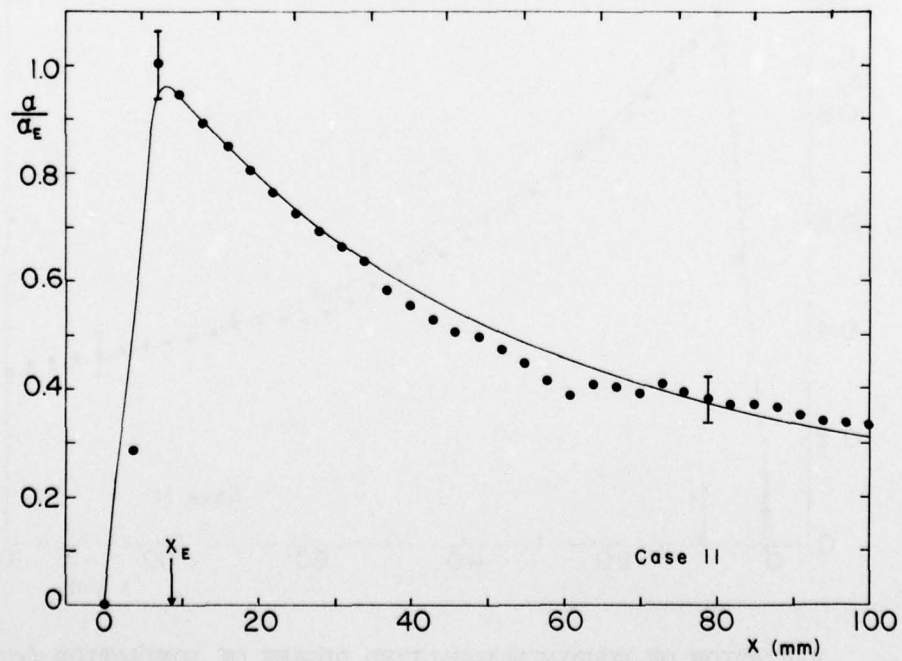
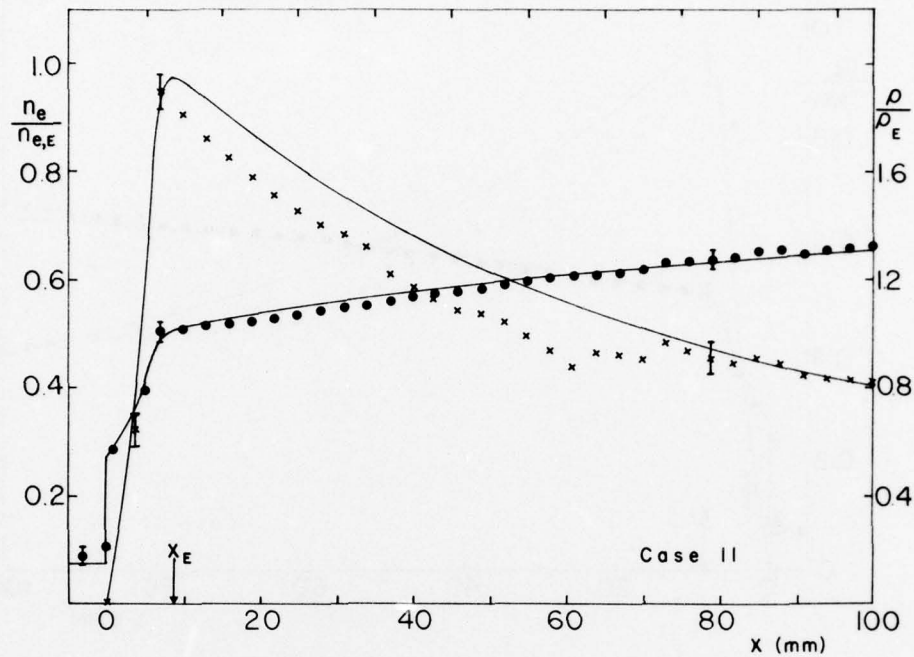


FIG. A34 VARIATION OF NONDIMENSIONALIZED DEGREE OF IONIZATION ( $\alpha/\alpha_E$ ) WITH DISTANCE  $x$  FOR CASE II.

FIG. A35 VARIATIONS OF NONDIMENSIONALIZED ELECTRON NUMBER DENSITY ( $n_e/n_{e,E}$ ) AND DENSITY ( $\rho/\rho_E$ ) WITH DISTANCE  $x$  FOR CASE II.

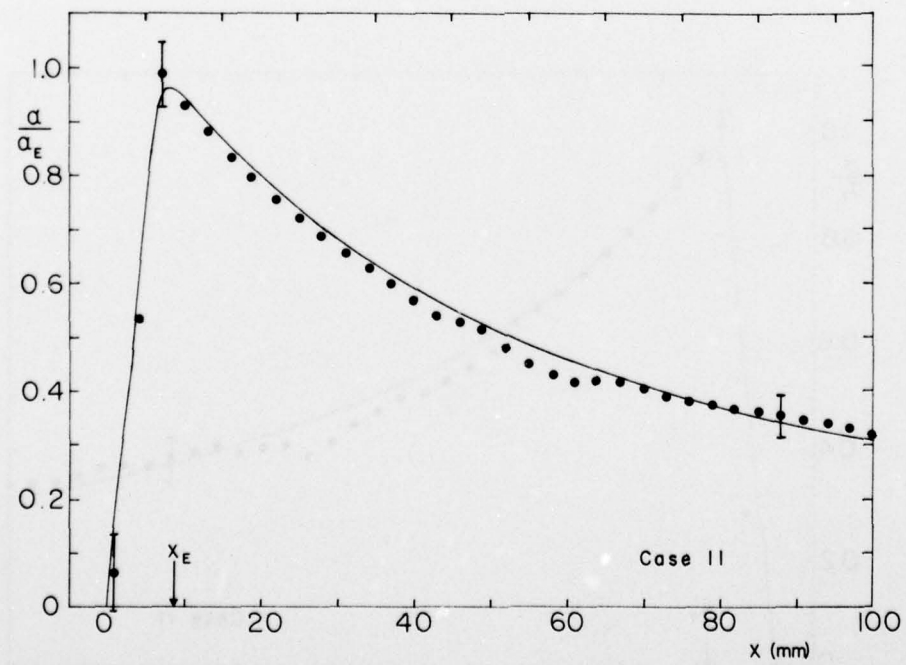
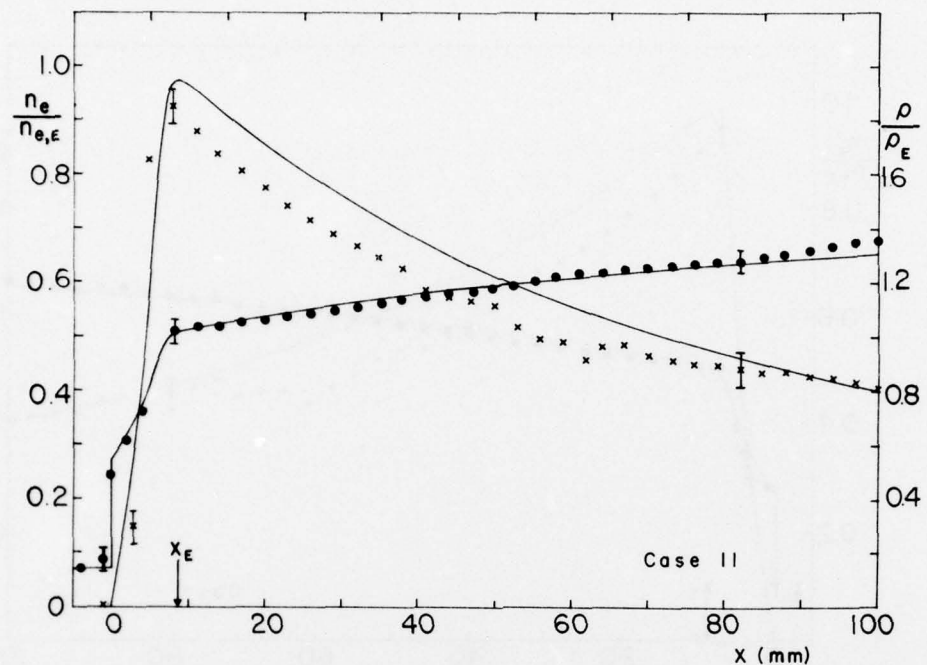


FIG. A36 VARIATION OF NONDIMENSIONALIZED DEGREE OF IONIZATION ( $\alpha/\alpha_E$ ) WITH DISTANCE  $x$  FOR CASE II.

FIG. A37 VARIATIONS OF NONDIMENSIONALIZED ELECTRON NUMBER DENSITY ( $n_e/n_{e,E}$ ) AND DENSITY ( $\rho/\rho_E$ ) WITH DISTANCE  $x$  FOR CASE II.

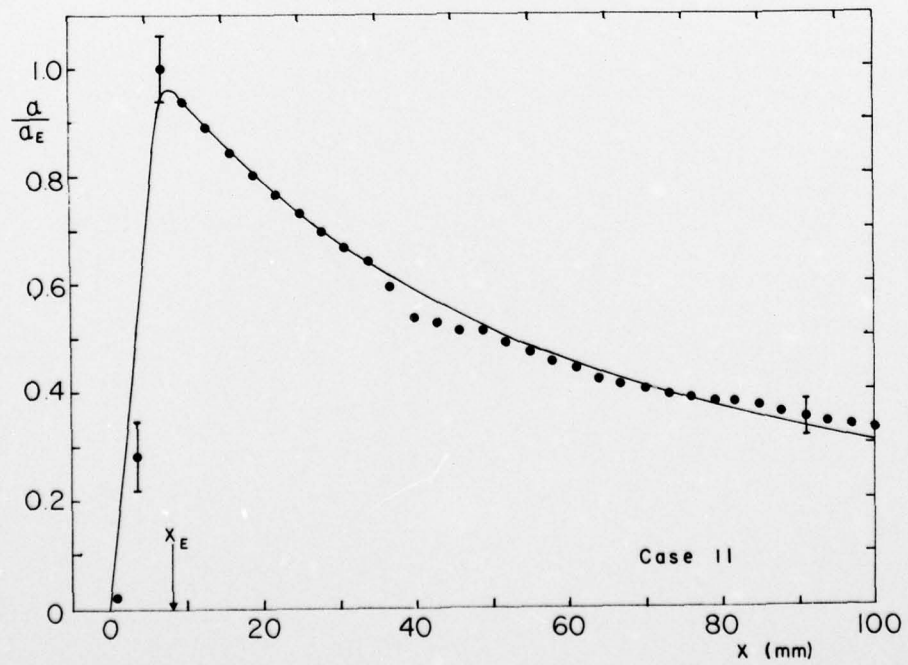
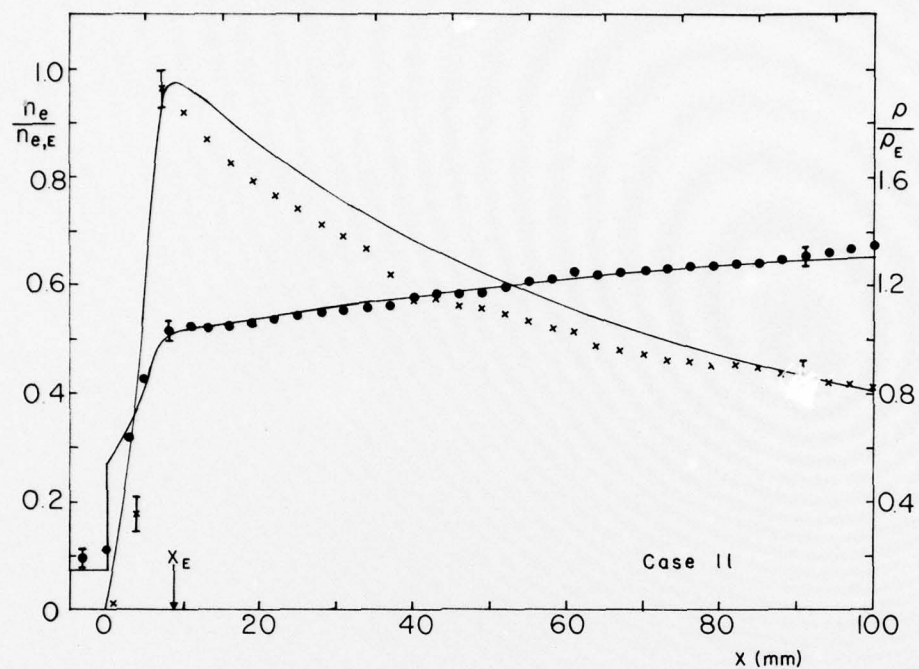


FIG. A38 VARIATION OF NONDIMENSIONALIZED DEGREE OF IONIZATION ( $\alpha/\alpha_E$ ) WITH DISTANCE  $x$  FOR CASE II.

UTIAS TECHNICAL NOTE NO. 212  
Institute for Aerospace Studies, University of Toronto (UTIAS)

4925 Dufferin Street, Don Mills, Ontario, Canada, N3H 2W6

EFFECTS OF IMPURITIES ON SHOCK WAVE STABILITY AND STRUCTURE IN IONIZING MONATOMIC GASES

TANG, P. C. Approx 50 pages

Approx 80 figures

1. Ionizing shock-wave structure 2. Shock-wave stability 3. Collision cross-sections

4. Radiation effects in shock waves 5. Impurity effects on ionizing monatomic shock waves

6. Interferometric measurements of shock-wave structure.

The effects of impurities - hydrogen, water vapour and sodium chloride - on shock wave stability and structure in ionizing-argon and krypton flows were investigated by using a dual-wavelength Mach-Zehnder interferometer in conjunction with the UTIAS 10 cm x 18 cm (4" x 7") hypervelocity Shock Tube. At shock Mach number of about 15, when pure argon or krypton is used as a test gas, the resulting translational shock front develops sinusoidal oscillations. The subsequent ionization relaxation region, the electron-cascade front and the quasi-equilibrium state also exhibit unstable characteristics. The addition of small amounts of hydrogen (0.5% by pressure) to the test gas stabilizes the entire flow and at the same time drastically shortens the relaxation length to about 1/3 of the original value in argon and 2/3 in krypton. The addition of about 1% of water vapour (by pressure) to the argon test gas also stabilizes the flow and shortens the relaxation region. A thin coating of dissolved sodium chloride in water on the shock tube wall, which on evacuation leaves a rough surface of crystals, however, does not seem to have any effect on the flow. Although the small impurities of hydrogen and water vapour have a significant effect in stabilizing the shock, the overall values of density and electron number density in the quasi-equilibrium region remain nearly the same. The present experimental results provided the data for a theoretical study which took into account atom-atom collisions, electron-atom collisions and radiation-energy losses to deduce a precise value for the atom-atom excitation cross-section constants for argon and krypton having values of  $g_{Ar-Ar} = 1.0 \times 10^{-19} \text{ cm}^2/\text{eV}$  and  $g_{Kr-Kr} = 1.2 \times 10^{-19} \text{ cm}^2/\text{eV}$ , respectively.

Available copies of this report are limited. Return this card to UTIAS, if you require a copy.

UTIAS TECHNICAL NOTE NO. 212  
Institute for Aerospace Studies, University of Toronto (UTIAS)

4925 Dufferin Street, Don Mills, Ontario, Canada, N3H 2W6

EFFECTS OF IMPURITIES ON SHOCK WAVE STABILITY AND STRUCTURE IN IONIZING MONATOMIC GASES

TANG, P. C. Approx 50 pages

Approx 80 figures

1. Ionizing shock-wave structure 2. Shock-wave stability 3. Collision cross-sections

4. Radiation effects in shock waves 5. Impurity effects on ionizing monatomic shock waves

6. Interferometric measurements of shock-wave structure.

The effects of impurities - hydrogen, water vapour and sodium chloride - on shock wave stability and structure in ionizing-argon and krypton flows were investigated by using a dual-wavelength Mach-Zehnder interferometer in conjunction with the UTIAS 10 cm x 18 cm (4" x 7") hypervelocity Shock Tube. At shock Mach number of about 15, when pure argon or krypton is used as a test gas, the resulting translational shock front develops sinusoidal oscillations. The subsequent ionization relaxation region, the electron-cascade front and the quasi-equilibrium state also exhibit unstable characteristics. The addition of small amounts of hydrogen (0.5% by pressure) to the test gas stabilizes the entire flow and at the same time drastically shortens the relaxation length to about 1/3 of the original value in argon and 2/3 in krypton. The addition of about 1% of water vapour (by pressure) to the argon test gas also stabilizes the flow and shortens the relaxation region. A thin coating of dissolved sodium chloride in water on the shock tube wall, which on evacuation leaves a rough surface of crystals, however, does not seem to have any effect on the flow. Although the small impurities of hydrogen and water vapour have a significant effect in stabilizing the shock, the overall values of density and electron number density in the quasi-equilibrium region remain nearly the same. The present experimental results provided the data for a theoretical study which took into account atom-atom collisions, electron-atom collisions and radiation-energy losses to deduce a precise value for the atom-atom excitation cross-section constants for argon and krypton having values of  $g_{Ar-Ar} = 1.0 \times 10^{-19} \text{ cm}^2/\text{eV}$  and  $g_{Kr-Kr} = 1.2 \times 10^{-19} \text{ cm}^2/\text{eV}$ , respectively.

Available copies of this report are limited. Return this card to UTIAS, if you require a copy.

UTIAS TECHNICAL NOTE NO. 212  
Institute for Aerospace Studies, University of Toronto (UTIAS)

4925 Dufferin Street, Don Mills, Ontario, Canada, N3H 2W6

EFFECTS OF IMPURITIES ON SHOCK WAVES STABILITY AND STRUCTURE IN IONIZING MONATOMIC GASES

TANG, P. C. Approx 50 pages

Approx 80 figures

1. Ionizing shock-wave structure 2. Shock-wave stability 3. Collision cross-sections

4. Radiation effects in shock waves 5. Impurity effects on ionizing monatomic shock waves

6. Interferometric measurements of shock-wave structure.

The effects of impurities - hydrogen, water vapour and sodium chloride - on shock wave stability and structure in ionizing-argon and krypton flows were investigated by using a dual-wavelength Mach-Zehnder interferometer in conjunction with the UTIAS 10 cm x 18 cm (4" x 7") hypervelocity Shock Tube. At shock Mach number of about 15, when pure argon or krypton is used as a test gas, the resulting translational shock front develops sinusoidal oscillations. The subsequent ionization relaxation region, the electron-cascade front and the quasi-equilibrium state also exhibit unstable characteristics. The addition of small amounts of hydrogen (0.5% by pressure) to the test gas stabilizes the entire flow and at the same time drastically shortens the relaxation length to about 1/3 of the original value in argon and 2/3 in krypton. The addition of about 1% of water vapour (by pressure) to the argon test gas also stabilizes the flow and shortens the relaxation region. A thin coating of dissolved sodium chloride in water on the shock tube wall, which on evacuation leaves a rough surface of crystals, however, does not seem to have any effect on the flow. Although the small impurities of hydrogen and water vapour have a significant effect in stabilizing the shock, the overall values of density and electron number density in the quasi-equilibrium region remain nearly the same. The present experimental results provided the data for a theoretical study which took into account atom-atom collisions, electron-atom collisions and radiation-energy losses to deduce a precise value for the atom-atom excitation cross-section constants for argon and krypton having values of  $g_{Ar-Ar} = 1.0 \times 10^{-19} \text{ cm}^2/\text{eV}$  and  $g_{Kr-Kr} = 1.2 \times 10^{-19} \text{ cm}^2/\text{eV}$ , respectively.

Available copies of this report are limited. Return this card to UTIAS, if you require a copy.

UTIAS TECHNICAL NOTE NO. 212  
Institute for Aerospace Studies, University of Toronto (UTIAS)

4925 Dufferin Street, Don Mills, Ontario, Canada, N3H 2W6

EFFECTS OF IMPURITIES ON SHOCK WAVES STABILITY AND STRUCTURE IN IONIZING MONATOMIC GASES

TANG, P. C. Approx 50 pages

Approx 80 figures

1. Ionizing shock-wave structure 2. Shock-wave stability 3. Collision cross-sections

4. Radiation effects in shock waves 5. Impurity effects on ionizing monatomic shock waves

6. Interferometric measurements of shock-wave structure.

The effects of impurities - hydrogen, water vapour and sodium chloride - on shock wave stability and structure in ionizing-argon and krypton flows were investigated by using a dual-wavelength Mach-Zehnder interferometer in conjunction with the UTIAS 10 cm x 18 cm (4" x 7") hypervelocity Shock Tube. At shock Mach number of about 15, when pure argon or krypton is used as a test gas, the resulting translational shock front develops sinusoidal oscillations. The subsequent ionization relaxation region, the electron-cascade front and the quasi-equilibrium state also exhibit unstable characteristics. The addition of small amounts of hydrogen (0.5% by pressure) to the test gas stabilizes the entire flow and at the same time drastically shortens the relaxation length to about 1/3 of the original value in argon and 2/3 in krypton. The addition of about 1% of water vapour (by pressure) to the argon test gas also stabilizes the flow and shortens the relaxation region. A thin coating of dissolved sodium chloride in water on the shock tube wall, which on evacuation leaves a rough surface of crystals, however, does not seem to have any effect on the flow. Although the small impurities of hydrogen and water vapour have a significant effect in stabilizing the shock, the overall values of density and electron number density in the quasi-equilibrium region remain nearly the same. The present experimental results provided the data for a theoretical study which took into account atom-atom collisions, electron-atom collisions and radiation-energy losses to deduce a precise value for the atom-atom excitation cross-section constants for argon and krypton having values of  $g_{Ar-Ar} = 1.0 \times 10^{-19} \text{ cm}^2/\text{eV}$  and  $g_{Kr-Kr} = 1.2 \times 10^{-19} \text{ cm}^2/\text{eV}$ , respectively.

Available copies of this report are limited. Return this card to UTIAS, if you require a copy.

REPORT DOCUMENTATION PAGE		READ INSTRUCTIONS BEFORE COMPLETING FORM
1. REPORT NUMBER <b>AFOSR-TR- 78-0841</b>	2. GOVT ACCESSION NO.	3. RECIPIENT'S CATALOG NUMBER
4. TITLE (and Subtitle) EFFECTS OF IMPURITIES ON SHOCK WAVE STABILITY AND STRUCTURE IN IONIZING MONATOMIC GASES		5. TYPE OF REPORT & PERIOD COVERED INTERIM
7. AUTHOR(s) F. C. TANG		6. PERFORMING ORG. REPORT NUMBER AFOSR 77-3303
9. PERFORMING ORGANIZATION NAME AND ADDRESS UNIVERSITY OF TORONTO INSTITUTE FOR AEROSPACE STUDIES M3H 5T6 4925 DUFFERIN ST, DOWNSVIEW, ONTARIO, CANADA		10. PROGRAM ELEMENT, PROJECT, TASK AREA & WORK UNIT NUMBERS 2307A3 61102F
11. CONTROLLING OFFICE NAME AND ADDRESS AIR FORCE OFFICE OF SCIENTIFIC RESEARCH/NA BLDG 410 BOLLING AIR FORCE BASE, D C 20332		12. REPORT DATE Nov 77
14. MONITORING AGENCY NAME & ADDRESS (if different from Controlling Office)		13. NUMBER OF PAGES 102
		15. SECURITY CLASS. (of this report) UNCLASSIFIED
		15a. DECLASSIFICATION/DOWNGRADING SCHEDULE
16. DISTRIBUTION STATEMENT (of this Report)  Approved for public release; distribution unlimited.		
17. DISTRIBUTION STATEMENT (of the abstract entered in Block 20, if different from Report)		
18. SUPPLEMENTARY NOTES		
19. KEY WORDS (Continue on reverse side if necessary and identify by block number) IONIZING SHOCK-WAVE STRUCTURE SHOCK-WAVE STABILITY COLLISION CROSS-SECTIONS RADIATION EFFECTS IN SHOCK WAVES IMPURITY EFFECTS ON IONIZING MONATOMIC SHOCK WAVES INTERFEROMETRIC MEASUREMENTS OF SHOCK-WAVE STRUCTURE		
20. ABSTRACT (Continue on reverse side if necessary and identify by block number) The effects of impurities-hydrogen, water vapour and sodium chloride-on shock wave stability and structure in ionizing-argon and krypton flows were investigated by using a dual-wavelength Mach-Zehnder interferometer in conjunction with the UTIAS 10 cm x 18 cm (4" x 7") Hypervelocity Shock Tube. At shock Mach number of about 15, when pure argon or krypton is used as a test gas, the resulting translational shock front develops sinusoidal oscillations. The subsequent ionization relaxation region, the electron-cascade front and the quasi-equilibrium state also exhibit unstable characteristics. The addition of small amounts of hydrogen (> 0.5% by pressure) to the test gas stabilizes the		

entire flow and at the same time drastically shortens the relaxation length to about 1/3 of the original value in argon and 2/3 in krypton. The addition of about 1% of water vapour (by pressure) to the argon test gas also stabilizes the flow and shortens the relaxation region. A thin coating of dissolved sodium chloride in water on the shock tube wall, which on evacuation leaves a rough surface of crystals, however, does not seem to have any effect on the flow. Although the small impurities of hydrogen and water vapour have a significant effect in stabilizing the shock, the overall values of density and electron number density in the quasi-equilibrium region remain nearly the same. The present experimental results provided the data for a theoretical study which took into account atom-atom collisions, electron-atom collisions and radiation-energy losses to deduce a precise value for the atom-atom collision excitation cross-section constants for argon and krypton having values of  $S^*_{Ar-Ar} = 1.0 \times 10^{-19} \text{ cm}^2/\text{eV}$  and  $S^*_{Kr-Kr} = 1.2 \times 10^{-19} \text{ cm}^2/\text{eV}$ , respectively.

UNCLASSIFIED

SECURITY CLASSIFICATION OF THIS PAGE(When Data Entered)